Pacific Northwest National Laboratory
Operated by Battelle for the
U.S. Department of Energy

Experimental and Numerical Investigations of Soil Desiccation for Vadose Zone Remediation: Report for Fiscal Year 2007

A.L. Ward
M. Oostrom
D.H. Bacon

January 2008

DISCLAIMER

This report was prepared as an account of work sponsored by an agency of the United States Government. Neither the United States Government nor any agency thereof, nor Battelle Memorial Institute, nor any of their employees, makes **any warranty, express or implied, or assumes any legal liability or responsibility for the accuracy, completeness, or usefulness of any information, apparatus, product, or process disclosed, or represents that its use would not infringe privately owned rights**. Reference herein to any specific commercial product, process, or service by trade name, trademark, manufacturer, or otherwise does not necessarily constitute or imply its endorsement, recommendation, or favoring by the United States Government or any agency thereof, or Battelle Memorial Institute. The views and opinions of authors expressed herein do not necessarily state or reflect those of the United States Government or any agency thereof.

PACIFIC NORTHWEST NATIONAL LABORATORY
operated by
BATTELLE
for the
UNITED STATES DEPARTMENT OF ENERGY
under Contract DE-ACO5-76RL01830

Printed in the United States of America

Available to DOE and DOE contractors from the
Office of Scientific and Technical Information,
P.O. Box 62, Oak Ridge, TN 37831-0062;
ph: (865) 576-8401
fax: (865) 576 5728
email: reports@adonis.osti.gov

Available to the public from the National Technical Information Service,
U.S. Department of Commerce, 5285 Port Royal Rd., Springfield, VA 22161
ph: (800) 553-6847
fax: (703) 605-6900
email: orders@nits.fedworld.gov
online ordering: http://www.ntis.gov/ordering.htm

This document was printed on recycled paper.
(8/00)

Experimental and Numerical Investigations of Soil Desiccation for Vadose Zone Remediation: Summary Report for Fiscal Year 2007

A. L. Ward
M. Oostrom
D.H. Bacon

January 2008

Pacific Northwest National Laboratory
Richland, Washington 99352

Summary

Apart from source excavation, the options available for the remediation of vadose zone metal and radionuclide contaminants beyond the practical excavation depth (0 to 15 m) are quite limited. Of the available technologies, very few are applicable to the deep vadose zone with the top-ranked candidate being soil desiccation. An expert panel review of the work on infiltration control and supplemental technologies identified a number of knowledge gaps that would need to be overcome before soil desiccation could be deployed. The report documents some of the research conducted in the last year to address some of these knowledge gaps. This work included 1) performing intermediate-scale laboratory flow cell experiments to demonstrate the desiccation process, 2) implementing a scalable version of Subsurface Transport Over Multiple Phases–Water-Air-Energy (STOMP-WAE), and 3) performing numerical experiments to identify the factors controlling the performance of a desiccation system.

Four laboratory experiments were conducted in an intermediate-scale flow cell to demonstrate the desiccation process and assess the impact of the energy balance on the desiccation process. One of the experiments was performed in homogeneous medium-grained sand, while the rest of the simulations were completed in a heterogeneous system with an inclusion of a fine-grained sand zone and varying levels of external insulation. Evaporative cooling was observed in the experiments and generally decreased with increased distance from the gas inlet chamber. Observations of temperature in fine-grained sands in the heterogeneous systems show two local minima associated with the cooling because of evaporation in the adjacent medium-grained sand whereas the second is attributed to evaporative cooling in the fine-grained sand itself. The occurrence of these temperature minima coincided with passage of the desiccation front. Results of the laboratory tests are consistent with the theory showing that the injection of air leads to significant temperature and moisture changes in the porous medium. In all the experiments, the injection of dry air proved to be an effective means for removing essentially all moisture from the test media. The results of this study provide a unique data set that will be used to calibrate the STOMP code for use in the designs of field-scale desiccation systems.

To aid in the design and evaluation of desiccation technologies, STOMP-WAE-B has been enhanced with the addition of gas injection/withdrawal wells. The upgraded version of STOMP-WAE-B is now available for scalable execution on multiple processor (i.e., parallel) computers. The parallel version of the simulator is written in pure FORTRAN 90 with embedded directives that are interpreted by a FORTRAN preprocessor. Without the preprocessor, the scalable version of the simulator can be executed sequentially on a single processor computer. The scalable version of the simulator is designated as STOMP-WAE-B-Sc and is expected to find applications in the design and optimization of desiccation systems on parallel computing architectures.

Numerical simulations performed with the upgraded STOMP-WAE were used to examine the factors influencing desiccation-system performance. The effectiveness of desiccation is dependent on achieving and maintaining sufficient fluid flow to support the dominant processes. The effectiveness of desiccation depends strongly on soil texture, air temperature, air pressure, humidity, and soil moisture content. Simulations show very good performance in coarse-textured sediments and even coarse sediments with fine-textured interbeds. The highest efficiency was achieved when air, heated to at least 25°C above the ambient soil temperature and dried to a relative humidity of 25% or less, was injected at a pressure at least equal to the air entry pressure of the soil, but ideally above 344 kPa (50 psi).

Acronyms

DOE-RL	U.S. Department of Energy-Richland Operations
DL	directive language
EMSL	Environmental and Molecular Sciences Laboratory
ERDF	Environmental Remediation Disposal Facility
FH	Fluor Hanford
FML	flexible membrane liner
FP	FORTRAN Preprocessor
HDPE	high-density polyethylene
HET1, 2, 3	Heterogeneous experiments
HOM1	Homogeneous-porous media experiment
MPI	Message Passing Interface
PNNL	Pacific Northwest National Laboratory
PVC	polyvinyl chloride
RH	relative humidity
STOMP	Subsurface Transport Over Multiple Phases
USDA	U.S. Department of Agriculture
WAE-B	Water-Air-Energy w/Barrier Module

Contents

Figures

Tables

1.0   Introduction

The options currently available for remediating vadose zone metal and radionuclide contaminants are quite limited. Perhaps one of the most widely used remedies, landfilling, is becoming increasingly difficult and may even be cost-prohibitive at waste sites like Hanford's BC Cribs and Trenches that cover large areas. The remedial options are even more limited when dealing with radionuclides, which, unlike organic contaminants, are not volatile, and are not easily degraded in the short term. Remediation technologies are then limited mostly to separation, volume reduction, and/or immobilization (van Deuren et al. 2002). Stabilization and solidification technologies are mostly directed to encapsulation or immobilizing the harmful constituents and involve processing of the waste *in situ* or *ex situ*. Briefly, in the solidification process, contaminants are mechanically locked within a solidified matrix, typically cement, to produce a high-strength monolithic block, but the contaminants may not interact chemically with the solidification reagents. Stabilization typically involves adding chemical binders that limit the solubility or mobility of waste constituents. This can be conducted either *in situ* or *ex situ,* but it always involves using additives to form a uniform matrix to encapsulate the contaminants. Vitrification processes are solidification methods that essentially melt and convert waste materials into glass or other crystalline products. Contaminants such as heavy metals and radionuclides are incorporated into the glass structure to form a relatively strong, durable material resistant to leaching.

At sites with complex hydrogeology and those where contaminants are located beyond the practical depth of excavation, the options are even more limited (Ward et al. 2004). Truex[a] reviewed six technology alternatives for minimizing downward contamination transport: these were *in situ* gaseous reduction, vadose zone bioreduction, vadose zone permeable reactive barrier remediation, redox manipulation, *in situ* grouting, and soil desiccation. The basic premise of the soil-desiccation technology is to inject dry air, accompanied by the withdrawal of an equal volume of wet air in an array of wells (FH 2006). In combination with surface flux control, the technique can be used to immobilize contamination by reducing the hydraulic conductivity. Truex[a] concluded that soil desiccation had the least uncertainty of the six technologies. Soil desiccation is recognized as a potentially robust remediation process for the deep vadose zone because it is based on a physical phenomena, i.e., evaporation, that can be induced by air injection and extraction.

In 2005, the U.S. Department of Energy-Richland Operations (DOE-RL) and Fluor Hanford (FH) convened 3-day workshop to allow an independent technical panel to review deep vadose zone remediation technologies for use at the Hanford Site in general and the BC Cribs and Trenches in particular. The panel was tasked with assessing the most viable and practical approach for deep vadose zone treatment technology to supplement engineered barriers and make recommendations for testing. The panel concluded that soil desiccation, in addition to surface infiltration control, could have applications for deep vadose zone application (FH 2006). However, they identified a number of knowledge gaps that would need to be overcome before this technology could be deployed. These included 1) energy limitations on the volume of water that can be removed, 2) osmotic effects during soil drying, and 3) potential remobilization of contaminants after cessation of desiccation.

---

[a] MJ Truex. 2004. *Feasibility Study Evaluation of In Situ Technologies for Immobilization of Technetium Beneath the BC Cribs*. Letter Report, Pacific Northwest National Laboratory, Richland, Washington.

The first concern is related to the relatively large amount of energy that is needed to evaporate water (2500 joules/gram). This energy has to be provided by the injected air and/or the subsurface conducting the air. Without considering energy transfer, the amount of water that can potentially be removed per unit volume of air is the difference between the saturated water-vapor density and the water-vapor density of the injected dry air at a certain temperature. However, since energy has to be provided for water evaporation, it is more likely that water-vapor saturation will take place at the lower wet-bulb temperature, yielding a lower saturated water-vapor density. For example, the saturated water-vapor density of $15^{o}C$ air is 13 g/m^3. However, the density at the wet-bulb temperature of $5.5^{o}C$ is only 7 g/m^3. The considerable difference between these two numbers results in a potential slower water removal when energy effects are considered. The panel recommended that the effects should be quantified in laboratory experiments, including experiments with elevated air temperatures to minimize energy-balance issues.

The second concern raised by the panel relates to potential osmotic effects since lower vapor pressures will occur in zones of increased salt concentrations. Reductions in vapor pressure will reduce the efficiency and rate of desiccation (FH 2006). Previous studies of the fate and transport of hypersaline fluids in Hanford sediments suggest several important roles. Work by Ward et al. (2001) suggests that the fine-textured, low-permeability interbeds in the Hanford formation may exhibit semi-permeable membrane behavior and act to restrict solute transport relative to the flow of water. The mechanisms for this phenomenon include chemical osmosis (fluid flow in direction of higher salinity); electro-osmosis (flow of water, dragged along by ions moving due to an electric potential gradient); and ultra-filtration (solute sieving driven by a hydraulic gradient). The resulting flow of water in response to the concentration gradient could essentially pull water from the surrounding untreated regions, affecting the efficacy of the desiccation system, and could compound the energy-balance issues related to the first concern. The panel's third concern relates to the remobilization of high-concentration solutes after rewetting. Rewetting and remobilization may result in (temporary) increased concentrations and contaminant mass fluxes.

Soil desiccation has, to our knowledge, not been applied in the laboratory and the field as a method to immobilize contaminants in the unsaturated zone. The most closely related applications include the dry barrier concept in which evaporation of water from specific layers in multilayered engineered barriers has been shown to enhance barrier performance (Ankeny and Burhard 1995). Raimondi et al. (1997) described a system and method of preventing groundwater contamination from vadose zone sources by establishing a dry barrier between a contaminant plume and the water table. They proposed forming a barrier by injecting dry gas into the barrier region and subsequently removing the gas and moisture it had absorbed via extraction wells. They suggested that by maintaining the barrier, the contaminants would form an immobile crust above the barrier, which would assist in preventing the transport of contaminants into the groundwater from leaking tanks in the vadose zone. There is no evidence that this concept was ever tested, and Raimondi et al. (1997) provided neither performance data nor information on optimal operating parameters. Nonetheless, the potential value of soil desiccation is multifaceted and site dependent. Not only does desiccation have the potential to immobilize contaminants, but it could potentially improve access for other treatments (e.g., gas-phase manipulations) by reducing water content and increasing gas-phase permeability.

There has been one reported account of the use of soil desiccation in response to subsurface air injection as a means of leak mitigation with application to tank farms. Cameron et al. (2002) conducted a field demonstration of soil desiccation at the Hanford Mock Tank Site to dry a zone below a tank. More than

1000 gallons of water were removed during a 2-week test, although the removed volume included both water from the vadose zone and injected air because no dehumidification was applied to the injected air. Several soil-vapor-extraction experiments have been reported in which soil desiccation was observed as a byproduct of subsurface remediation efforts. For example, the intermediate-scale experiment described by Oostrom et al. (2005) showed that injecting dry air would not only accelerate carbon tetrachloride removal but would also remove water vapor at almost equilibrium concentrations when moderate injection rates were applied.

The limited data available suggest that successfully designing, deploying, and operating a field-scale soil desiccation system requires a detailed understanding of mass and energy transport in heterogeneous sediments under transient conditions. The expert panel recommended that the three major concerns would best be addressed by 1) developing, testing, and verifying a multiphase numerical simulator for field-scale modeling of desiccation and associated processes and 2) demonstrating the technique with focused laboratory experiments and addressing technical concerns related to the energy balance, osmotic effects, and the potential for remobilization after the desiccation period. To improve the understanding of the impact of these issues on soil desiccation and the potential for remobilization, Pacific Northwest National Laboratory (PNNL) conducted a series of detailed intermediate-scale laboratory experiments and parametric numerical simulations. The results of these laboratory and numerical experiments are intended to assist FH in resolving the outstanding issues in relation to field application of soil-desiccation technology.

1.1   Scope and Objectives

The scope of this project covered the intermediate-scale laboratory experimentation, model development, and numerical simulations. In response to the need for improved modeling capabilities, modifications were made to the water-air-energy mode of the STOMP simulator to 1) permit simulation of the subsurface injection and withdrawal of air and 2) extend constitutive theory to allow for accurate representation of air-phase permeability-saturation relationships. To support the design, implementation, and testing of a field-scale desiccation system, the barrier extension of the water-air-operational mode of STOMP was upgraded to permit scalable execution on multiple processor (i.e., parallel) computers. A series of laboratory experiments were conducted to demonstrate the desiccation process at the intermediate scale using a wedge-shaped flow cell. These experiments were also intended to develop a detailed temperature and relative-humidity data set and to test and verify the water-air-energy mode of the Subsurface Transport Over Multiple Phases (STOMP) simulator (White and Oostrom 2006). The FORTRAN77 version of the STOMP simulator was used to predict the intermediate-scale experiments whereas the upgraded, scalable version was used to investigate the factors controlling the performance of a desiccation system.

This report presents the activities performed in FY 2007. Section 1 is the introductory section. Section 2 describes the scalable implementation and testing of the water-air-energy operational mode of STOMP. Section 3 describes the intermediate-scale flow-cell experiments. Section 4 provides a summary of the modeling used to identify factors affecting the performance of a desiccation system and discusses the results in relation to their application to optimization of the design of a field test. Section 5 provides the overall summary and conclusions and discusses the implications of these findings on the design of a field-scale desiccation test.

2.0   Scalable Implementation of STOMP-WAE

Soil desiccation is a multiphase, nonisothermal problem, and if used to supplement engineered-surface-barrier technology, as is being proposed, it will be necessary to consider a component of the soil-vegetation-atmosphere continuum. Plants play an important role in the water and energy balance of engineered covers and are therefore critical to the water balance of the waste site to be treated by desiccation. The surface and subsurface energy balance are both influenced by meteorological forces. Although there are no published studies of the factors affecting the performance of soil-desiccation technologies, some insight can be gained from studies of soil venting in which desiccation is typically reported as an undesirable side effect.

Numerous experimental and numerical studies of soil venting have been performed to examine the factors influencing system performance and to serve as a basis for designing remediation systems. At a particular site, the effectiveness of venting technologies is dependent on achieving and maintaining sufficient air flow to support the dominant processes. Air flow is governed by the air-phase permeability of the soil and the relationship between applied pressure or vacuum and gas flow rate. The effectiveness of these techniques therefore depends on soil texture, air temperature, air pressure, and soil moisture content through its effect on phase partitioning and diffusion, but, more importantly, on air permeability. Air-distribution patterns are also controlled by microscopic and macroscopic processes. At the pore-scale, variations in air entry pressures control the migration of the injected air whereas at the macroscale, low-permeability interbeds and similar features will govern the air migration patterns (Thomson and Johnson 2000). The efficacy of the desiccation system will ultimately be controlled by the interplay of processes across these two scales, and predicting the system response will depend on our ability to represent these two scales in a numerical model.

Mathematical models are an important component of improving our understanding of such complicated and coupled systems and our ability to predict air migration and desiccation patterns in response to air injections. The impact of subsurface heterogeneities and plume size on the efficiency of field-scale desiccation can only be investigated with large-scale simulations executed on parallel computing architectures. This section covers the conceptual model for soil desiccation, demonstrates the need for a nonisothermal flow and transport model, and describes the implementation of a scalable version of the water-air-energy model of the STOMP Simulator.

2.1   Materials and Methods

2.1.1   Conceptual Model

The conceptual model for the migration of air injected into the vadose zone is similar to those developed for *in situ* air sparging and soil venting (e.g., Johnson et al. 1993). Dry air is injected into a relatively short-screened interval in a partially penetrating well within the vadose zone whereas air humidified with moisture evaporated from the soil is withdrawn at a downgradient well (Figure 2.1). For the aqueous and gaseous phases, zero flux (no-flow) conditions are imposed on the left and right boundaries and the lower boundary of the domain. Air is injected at a constant pressure, temperature, and relative humidity. Air is extracted at a fixed pressure. Air is injected at pressures in excess of the air-entry pressure of the porous medium, ψ_b, and is extracted at a pressure less than or equal to atmospheric, P_0 (Figure 2.1). For the
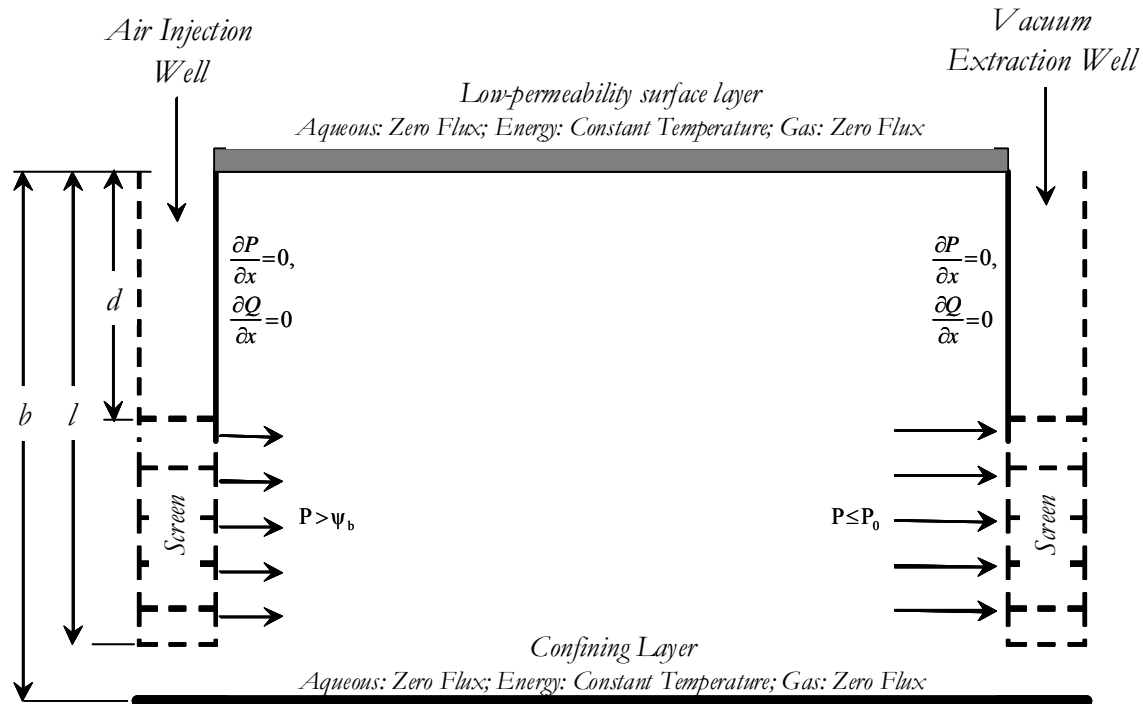
Figure 2.1. Schematic of a Two-Dimensional Cartesian Coordinate System Employed for Numerical Simulations of Vadose Zone Desiccation Where *b* is the Depth to Water Table or Low Permeability Boundary, *d* is the Depth to the Top of the Well Screen, and *l* is the Depth to the Bottom of the Well Screen

energy equations, Dirichlet (constant temperature) conditions are imposed on all boundaries. The ground surface and annulus around each well is assumed to be perfectly sealed to minimize short circuiting to the surface. As air moves through the sediment, the rate of flow is small enough that the injection system is able to maintain the injection pressure as the drying front expands outward. In homogeneous formations, both the air and temperature initially expand in a spherical fashion, away from the injection point, and grow upward and outward. Air flow continues until a boundary is encountered. The effectiveness of the method will therefore depend on how well the injected air is distributed within the geologic formation. In natural geologic media, heterogeneities can channel air flow through high-permeability zones, potentially bypassing low-permeability zones. In heterogeneous formations, preferential pathways for air flow typically occur in the coarse-textured, low-moisture zones whereas the bypassed zones are typically fine-textured, high-moisture zones with higher contaminant concentrations. These features may also lead to enhanced lateral migration away from the injection point. In low-permeability materials like silt and clay, the air-entry pressures are typically larger than the differences between the hydrostatic and air-injection pressures, and, as a result, air penetration can be quite limited. As a result, air moves laterally under the influence of the injection air pressure until the injection system can no longer maintain that pressure or until a vertical pathway is intersected.

In heterogeneous formations, the extent of lateral air migration will depend on the horizontal correlation lengths or connectivity of the layers (Ward et al. 2004) as well as the air-injection rate and the range of permeabilities. The modeling effort therefore considered both homogenous and heterogeneous

formations. The heterogeneous formation was assumed to be composed of alternating layers of coarse (high air permeability) and fine-textured (low air permeability) sediments.

As air is pumped or drawn into the soil from the atmosphere, it will be heated or cooled to the ambient soil temperature. Evaporation of the antecedent moisture requires energy, and this energy is provided mostly by the latent heat from injected air and can lead to significant changes in soil temperature. Thus, the system performance requires consideration of the energy balance. As in applications of soil-vapor extraction technologies, one potential method for enhancing desiccation in heterogeneous systems is to increase the soil temperature. The rate of diffusion is known to increase with increasing temperature through an increase in the vapor pressure. Thus, at higher temperatures, water could move out of stagnant low-permeability zones faster. This observation has led to the development of a number of different approaches to increasing soil temperature, including heating of the air-input stream. In soil applications of soil-vapor extraction, surface seals are often employed to increase efficiencies through their capability to prevent surface-water infiltration that can reduce air-flow rates, reduce the emission of contaminant vapors, and minimize vertical short-circuiting of air flow. At the Hanford site, soil desiccation is expected to be used to supplement engineered-barrier technology, which could have effects similar to a surface seal.

For this part of the study, a series of numerical experiments were conducted to investigate the effects of 1) low-permeability surface seals, 2) soil temperature, 3) injected air temperature, 4) injected air humidity, 5) air-injection pressure/vacuum, and 6) soil texture. In addition, the effects of heterogeneity were investigated using a simple layered system consisting of alternating layers of sand and silt loam.

2.1.2   Water-Air-Energy Operation Mode of STOMP

The STOMP simulator is a collection of operational modes, implementations, and modules for solving multi-fluid subsurface flow and reactive transport problems. Operational modes are distinguished by the solved coupled flow-and-transport equations. The Water-Air-Energy Operational Mode (STOMP-WAE) solves the coupled conservation equations for water mass, air mass, and thermal energy transported over three phases: aqueous, gas, and soil matrix. Modules are additional capabilities above the standard flow–and-transport schemes such as reactive transport (White and McGrail 2005), multifluid well models, and sparse vegetation surface models (Ward et al. 2005). The sparse vegetation module is implemented as a boundary condition on the upper surface of the computational domain and has capabilities for modeling evaporation from bare surfaces as well as evapotranspiration from sparsely vegetated surfaces populated with multiple plant species (Ward et al. 2005). This mode is the barrier extension of the WAE mode and is designated as STOMP-WAE-B. Input for STOMP-WAE-B is specified via three input cards and includes the following: atmospheric conditions through the *Atmospheric Conditions Card*, time-invariant plant species data through the *Plant Properties Card*, and time-varying plant species data through the *Boundary Conditions* Card. Two optional cards, the *Observed Data* and *UCODE Control* cards, allow the use of STOMP-W-I and STOMP-WAE-I, inverse operational modes of STOMP-W and STOMP-WAE, to estimate model parameters.

2.1.3   Scalable Implementation

Implementations of the operational modes of STOMP have been either sequential or scalable. Sequential implementations of the simulator were written in FORTRAN 77, with an option for dynamic memory allocation if compiled with a FORTRAN 90 compiler. Although some FORTRAN compilers offer auto-

parallelization, the scalable implementation is generally executed on a single processor computer. Scalable implementations were written in FORTRAN 90, but currently do not take advantage of the dynamic memory capabilities of the language.

The scalable implementation of STOMP-WAE followed the same path used for previous versions, e.g., STOMP-W and STOMP-WOA. The sequential implementations of the STOMP simulator were written first and represent the standard form of the simulator. The guiding objectives for developing the parallel implementation of the simulator were to 1) keep the source coding readable and modifiable by subsurface scientists, 2) allow both sequential and parallel execution, 3) leave the bulk of the parallelization to computer scientists, and 4) consign the parallel linear system solvers to applied mathematicians. The resulting coding scheme was to embed directives into the FORTRAN 90 version that defined the parallelism.

In developing the scalable implementations of the STOMP simulator, the choice was made to rewrite the simulator to take advantage of the parallel-programming structures built into the FORTRAN 90 language. These directives appear as FORTRAN 90 comments, which mean that the code can be compiled and executed as a conventional (i.e., sequential) implementation. This compilation option also allows for conventional debugging during the development stage. To realize the scalable implementation of the simulator, the embedded directives in the code are interpreted by a FORTRAN Preprocessor (FP) (Rosing and Yabusaki 1999). The FP comprises three components: 1) the preprocessor program, 2) the directive language (DL), and 3) the library. The FP is actually a generic preprocessor that has been programmed with a library of directives, written in a C25-like language, called DL (Rosing 2000) to operate on and manipulate FORTRAN 90 code fragments. Output from executing the FP program on the STOMP source code is new source coding with re-dimensioned arrays whose memory is distributed over the processors (i.e., compute nodes), calls to the Message Passing Interface (MPI library) (Gropp et al. 1999), and calls to the FP library.

2.1.4 Computational Domain Discretization

The STOMP simulator uses integral volume finite differencing for spatial discretization and backward Euler differencing for temporal discretization of the governing partial differential flow and transport equations. For spatial discretization, it is further assumed that the grid system is orthogonal and structured where a structured grid implies that a non-boundary grid cell has two, four, and six neighbors in one-, two-, and three-dimensional domains, respectively. Field variables (e.g., temperature, phase pressure, phase saturation, phase relative permeability, mole fraction) are defined at the grid centroids. Flux variables (e.g., component mass flux, energy flux) are defined at the centroid of the interfacial surface between two grid cells or the centroid of a boundary surface. Both field and flux variables are multi-dimensional arrays with the first three indices being used to define the grid-cell coordinates. The FP has been programmed with the assumption that the computational domain is discretized into a regular grid of processors (i.e., a contiguous subdomain of the structured grid is assigned to a processor). Grid cells that are within the assigned section of a processor's subdomain are defined to be local to the processor. A three-dimensional computational domain, representing a three-dimensional physical domain, can be discretized into a three-, two-, or one-dimensional grid of processors. In general, the processor domain dimensionality must be less than or equal to the computational domain dimensionality.

Field and flux variables are distributed over the processor domain according to user specifications, which include 1) dimensions to distribute, 2) number of ghost cells, and 3) number of boundary cells. For a three-dimensional computational domain, the user may specify that all three dimensions are distributed, that any two dimensions are distributed, or that any one dimension is distributed over the processors. Ghost cells refer to the number of computational grid cells that are duplicated in each of the distributed directions. Without ghost cells, fluxes on grid-cell surfaces that coincide with process boundaries would require field variables from two different processors. Ghost cells, therefore, allow flux calculations to remain local to the processors. Updating of the ghost cells is handled automatically by the FP. As flux variables are defined on computational domain grid surfaces, there is the potential for having misaligned distributions of flux and field variables over the processor distributions. The FP allows the user to define upper and lower boundary cells, which allows the flux variables to be aligned with field variables, thereby keeping all flux calculations local to the processor.

The default boundary condition in the STOMP simulator is a zero-flux boundary. Boundary conditions occur on the computational-domain boundary surfaces and on the boundary surfaces between active and inactive nodes. User-assigned boundary conditions specify conditions on a boundary surface associated with a single grid cell and are generally local calculations (i.e., involving a single processor). The FP allows for this type of calculation by delineating sections of code as being serial. To delineate a section of code as being serial, bounding directives are embedded in the FORTRAN code. Within serial sections of code, the FP provides additional support through "shared variable" directives for non-distributed variables or arrays that need to be consistent on all processors. Writes to a shared variable, within a serial section of code, are broadcast to all processors. For example, a shared variable could be used in conjunction with linked boundary surfaces where one boundary condition is dependent on an adjacent boundary condition (e.g., hydraulic-gradient-type boundary conditions).

In addition to handling distributed arrays, the parallelization of loops over grid cells and serial code sections, the FP automatically translates input and output statements. The general approach used by the FP is to execute all input and output on processor zero (i.e., the base processor of a processor cluster). Translation of the FORTRAN read and write statements depends on whether the variable being input or output is distributed. For non-distributed variables, FORTRAN read and write statements are executed from processor zero, and the data are then broadcast to all processors, therefore replicating the data on all processors. For distributed variables, the semantics depend on whether the data are formatted or unformatted. For formatted data, FORTRAN read and write statements are executed from processor zero, followed by a global broadcast. For unformatted data, special FP and MPI library calls are executed for the data-distribution operations. One limitation of the FP is that it is not possible to mix distributed and non-distributed variables in an unformatted FORTRAN read or write statement.

2.1.5 Gas Injection/Withdrawal Well Model

The multi-fluid well model for the STOMP-WAE-B simulator assumes a vertical, circular cross-section well transecting a vertical column of formation grids (i.e., well nodes within formation nodes). Well nodes are assumed to have the same vertical extent as the formation nodes and assume frictionless flow of fluids between the well and formation nodes. Multi-fluid wells, therefore, comprise a vertical array of well nodes imbedded within a vertical array of formation nodes. The bottom and top of the well nodes are assumed to exist at formation grid surfaces. The well bottom is defined through user input as a gas Dirichlet surface where the gas pressure and relative humidity are specified and remains unchanged over

time. Vertical flow within the well is assumed to be frictionless. Equilibrium conditions (e.g., aqueous-phase dissolved-gas is in equilibrium with gas) are assumed for the solution of the governing flow equations for the well nodes.

The governing flow equations for each well node are two mass balance equations for water and gas that take the form shown in Equation (2.1).

$$\frac{\partial m^i}{\partial t} - m^i_{in} + m^i_{out} = 0, \; for \; i = w, g \tag{2.1}$$

where
m^i = mass of component i in the well node, kg

m^i_{in} = mass rate of component i into the well node, kg/s

m^i_{out} = mass rate of component i out of the well node, kg/s

superscript w = water

superscript g = gas.

The mass of component i in the well node is defined according to Equation (2.2).

$$m^i = dz \, \pi \, r_w^2 \sum_{j=\ell, g} \left(\omega^i_j \, s_j \, \rho_j \right) \tag{2.2}$$

where
dz = cell height, m

r_w = well-bore radius, m

ω^i_j = mass fraction of component i in phase j

s_j = volume fraction (saturation) of phase j

ρ_j = density of phase j, m³/kg.

subscript ℓ = aqueous phase

subscript g = gas phase.

The mass flux is defined as being positive into a well node via flux through the screen and flux across the bottom surface.

The total mass flux into the well node equals the sum of the advective and diffusive components, as shown in Equation (2.3).

$$m^i_{in} = m^i_{in_{adv,screen}} + m^i_{in_{diff,screen}} + m^i_{in_{adv,bottom}} + m^i_{in_{diff,bottom}} + m^i_{in_{pump}} \tag{2.3}$$

2.6

where

$m_{in\,adv,screen}^{i}$ = advective mass flux in through the screen, kg/s

$m_{in\,diff,screen}^{i}$ = diffusive mass flux in through the screen, kg/s

$m_{in\,adv,bottom}^{i}$ = advective mass flux in across the bottom, kg/s

$m_{in\,diff,bottom}^{i}$ = diffusive mass flux in across the bottom, kg/s

$m_{in\,pump}^{i}$ = mass rate of component i pumped into the well, kg/s.

The advective mass flux through the screen is defined according to Equation (2.4).

$$m_{in_{adv,screen}}^{i} = \sum_{j=\ell,g} \frac{2\pi\, dz\, \mathbf{k}_{horz}\, (r_e^2 - r_w^2)\left(P_j - P_{j_w}\right)\omega_j^i\, \rho_j}{\mu_j\left[r_e^2 \ln\left(\dfrac{r_e}{r_w}\right) - \dfrac{(r_e^2 - r_w^2)}{2}\right]} \tag{2.4}$$

where

r_e = radius of influence, m

$\mathbf{k}_{horz}$ = average horizontal intrinsic permeability, m^2

P_j = pressure of phase j in the formation, Pa

P_{j_w} = pressure of phase j in the well, Pa

μ_j = viscosity of phase j, Pa s.

The average horizontal intrinsic permeability is computed according to Equation (2.5).

$$\mathbf{k}_{horz} = \sqrt{\mathbf{k}_x\, \mathbf{k}_y} \tag{2.5}$$

where $\mathbf{k}_x$ is the x-direction intrinsic permeability, m^2, $\mathbf{k}_y$ is the y-direction intrinsic permeability, m^2, and the radius of influence is computed according to Equation (2.6).

$$r_e = \sqrt{\frac{A_{horz}}{\pi}} \tag{2.6}$$

where A_{horz} is the aerial grid-cell area, m^2.

The diffusive flux through the screen is defined according to Equation (2.7).

2.7

$$m^i_{in_{diff,screen}} = \sum_{j=\ell,g} \frac{2\pi\,dz\,(r_e^2 - r_w^2)\left(\tau_j\,n_D\,\rho_j\,s_j\,M^i\,D^i_j\right)\left(\chi^i_j - \chi^i_{j_w}\right)}{M_j\left[r_e^2\ln\left(\dfrac{r_e}{r_w}\right) - \dfrac{(r_e^2 - r_w^2)}{2}\right]} \tag{2.7}$$

where

τ_j = phase tortuosity

n_D = porosity

M^i = molecular weight of component i, kg/kmol

M_j = molecular weight of phase j, kg/kmol

D^i_j = molecular diffusion coefficient of component i, m²/s

χ^i_j = mole fraction of component i in phase j in the formation

$\chi^i_{j_w}$ = mole fraction of component i in phase j in the well.

The advective mass flux across the bottom surface is defined according to Equation (2.8).

$$m^i_{in_{adv,bottom}} = \sum_{j=\ell,g} \frac{\pi\,r_w^2\,\omega^i_j\,\rho_j\,k_{j_w}}{\mu_j}\left(\frac{(P_{j_{wb}} - P_{j_w})}{dz_b} + \rho_j\,g\,z\right) \tag{2.8}$$

where

k_{j_w} = equivalent well intrinsic permeability, 10^{-6} m²

$P_{j_{wb}}$ = pressure of phase j at the bottom well node, Pa

P_{j_w} = pressure of phase j at the well node, Pa

dz_b = bottom inter-grid vertical distance, m

g = acceleration of gravity, m/s²

z = bottom surface elevation, m.

The diffusive mass flux across the bottom surface is defined according to Equation (2.9).

$$m^i_{in_{diff,bottom}} = \sum_{j=\ell,g} \frac{\pi\,r_w^2\,\rho_j\,M^i\,D^i_j}{M_j}\left(\frac{(\chi^i_{j_{wb}} - \chi^i_{j_w})}{dz_b}\right) \tag{2.9}$$

where $\chi^i_{j_{wb}}$ is the mole fraction of component i, phase j, at the bottom well node, and $\chi^i_{j_w}$ is the mole fraction of component i, phase j, at the well node.

The component mass pumped into the well is defined according to Equation (2.10).

$$m^i_{in_{pump}} = m_{in_{pump_\ell}} \, \omega^i_\ell \, \rho_\ell + m_{in_{pump_g}} \, \omega^i_g \, \rho_g \tag{2.10}$$

where $m_{in_{pump_\ell}}$ is the mass rate of aqueous phase pumped into the well, kg/s, and $m_{in_{pump_g}}$ is the mass rate of gas pumped into the well, kg/s.

The mass flux is defined as being positive out of a well node via flux through the top surface. The total mass flux out of the well node equals the sum of the advective and diffusive components, as shown in Equation (2.11).

$$m^i_{out} = m^i_{out_{adv,top}} + m^i_{out_{diff,top}} + m^i_{out_{pump}} \tag{2.11}$$

where $m^i_{out_{adv,top}}$ is the advective mass flux in across the top, kg/s, $m^i_{out_{diff,top}}$ is the diffusive mass flux in across the top, kg/s, and $m^i_{out_{pump}}$ is the mass flux of component i pumped from the well, kg/s.

The advective mass flux across the top surface is defined according to Equation (2.12).

$$m^i_{out_{adv,top}} = \sum_{j=\ell,g} \frac{\pi \, r_w^2 \, \omega^i_j \, \rho_j \, k_{j_w}}{\mu_j} \left(\frac{\left(P_{j_w} - P_{j_{wt}} \right)}{dz_t} + \rho_j \, g \, z \right) \tag{2.12}$$

where $P_{j_{wt}}$ is the pressure of phase j at the top well node, Pa, dz_b is the top inter-grid vertical distance, m, and z is the top surface elevation, m.

The diffusive mass flux across the bottom surface is defined according to Equation (2.13).

$$m^i_{out_{diff,top}} = \sum_{j=\ell,g} \frac{\pi \, r_w^2 \, \rho_j \, M^i \, D^i_j}{M_j} \left(\frac{\left(\chi^i_{j_w} - \chi^i_{j_{wt}} \right)}{dz_t} \right) \tag{2.13}$$

where $\chi^i_{j_{wt}}$ is the mole fraction of component i, phase j, at the top well node.

The component mass pumped from the well is defined according to Equation (2.14).

$$m^i_{out_{pump}} = m_{out_{pump_\ell}} \, \omega^i_\ell \, \rho_\ell + m_{out_{pump_g}} \, \omega^i_g \, \rho_g \qquad (2.14)$$

where $m_{out_{pump\ \ell}}$ is the mass rate of aqueous phase pumped from the well, kg/s, and $m_{out_{pump_g}}$ is the mass rate of gas pumped from the well, kg/s.

The amount of aqueous phase or gas pumped from a well node is limited according to Equations (2.15a) and (2.15b).

$$m_{out_{pump_\ell}} = \min\left[m^{def}_{out_{pump_\ell}} , \frac{m^{prev}_\ell}{dt} + m_{in_\ell} \right] \qquad (2.15a)$$

$$m_{out_{pump_g}} = \min\left[m^{def}_{out_{pump_g}} , \frac{m^{prev}_g}{dt} + m_{in_g} \right] \qquad (2.15b)$$

A critical component of the well model is the interfacial averaging schemes used to define fluid properties and surface areas at the screen, bottom surface, and top surface. For advective mass flux into the well through the screen, upwind interfacial averaging is applied to the calculation of the grid cell height and the component density of a component. The product of the grid cell height and component density for advective transfer across the well screen is computed according to the algorithm shown by Equations (2.16a to 2.16d)

$$\omega^i_\ell \, \rho_\ell \, dz = \omega^i_\ell \, \rho_\ell \, dz^* \, k_{r\ell} \quad for \ \left(P_\ell - P_{\ell_w} \right) \geq 0 \qquad (2.16a)$$

$$\omega^i_\ell \, \rho_\ell \, dz = \omega^i_{\ell_w} \, \rho_{\ell_w} \, dz^* \, s_{\ell_w} \quad for \ \left(P_\ell - P_{\ell_w} \right) < 0 \qquad (2.16b)$$

$$\omega^i_g \, \rho_g \, dz = \omega^i_g \, \rho_g \, dz^* \, k_{rg} \quad for \ \left(P_g - P_{g_w} \right) \geq 0 \qquad (2.16c)$$

$$\omega^i_g \, \rho_g \, dz = \omega^i_{g_w} \, \rho_{g_w} \, dz^* \, s_{g_w} \quad for \ \left(P_g - P_{g_w} \right) < 0 \qquad (2.16d)$$

where dz^* = geometric height of the well node

$k_{r\ell}$ = aqueous-phase relative permeability in the formation

s_{ℓ_w} = aqueous-phase volume fraction in the well node

k_{rg} = gas relative permeability in the formation

s_{g_w} = gas volume fraction in the well node.

Harmonic averaging is used to compute the phase viscosity at the well screen. For diffusive mass flux into the well through the screen, harmonic averaging is used to compute the effective molar diffusion coefficient as shown in Equations (2.17a and 2.17b)

$$\frac{\tau_\ell n_D \rho_\ell s_\ell D_\ell^a}{M_\ell} = \frac{\left(\dfrac{\rho_{\ell_w} s_{\ell_w} D_\ell^a}{M_{\ell_w}}\right)\left(\dfrac{\tau_{\ell_f} n_{D_f} \rho_{\ell_f} s_{\ell f} D_\ell^a}{M_{\ell f}}\right)(r_w + r_e)}{\left(\dfrac{\rho_{\ell_w} s_{\ell_w} D_\ell^a}{M_{\ell_w}}\right)r_w + \left(\dfrac{\tau_{\ell_f} n_{D_f} \rho_{\ell_f} s_{\ell f} D_\ell^a}{M_{\ell f}}\right)r_e}$$

(2.17a)

$$\frac{\tau_g n_D \rho_g s_g D_g^w}{M_g} = \frac{\left(\dfrac{\rho_{g_w} s_{g_w} D_g^w}{M_{g_w}}\right)\left(\dfrac{\tau_{g_f} n_{D_f} \rho_{g_f} s_{g_f} D_g^w}{M_{g f}}\right)(r_w + r_e)}{\left(\dfrac{\rho_{n_w} s_{n_w} D_n^w}{M_{g_w}}\right)r_w + \left(\dfrac{\tau_{g_f} n_{D_f} \rho_{g_f} s_{g_f} D_g^w}{M_{g f}}\right)r_e}$$

(2.17b)

For vertical flow within the well, a combination of harmonic, upwind, and downwind averaging is used. The phase permeability within the well for vertical advective flow is determined by upwind averaging of the phase saturation. For example, if the aqueous-head gradient is upward, then the permeability of the surface between two well nodes equals the saturation of the lower node. This scheme prevents fluid flux from a node void of a particular fluid and adds resistance to the flow of fluids from nodes with low saturation. Interfacial averaging for the component concentration follows the scheme specified for the field nodes, which is typically upwind averaging. The diffusive permeability of the surface between two nodes within the well is defined by downwind averaging of the phase saturation. For example, if the gradient in dissolved-gas concentration is upward, then the diffusive permeability of the surface between the two well nodes equals the aqueous saturation of the upper node. This scheme prevents diffusion of dissolved gas into a well node without aqueous phase. For intermediate saturations, the diffusive permeability acts as a phase tortuosity. The effective diffusion coefficient for a surface between two well nodes is computed using the harmonic average.

2.1.6 Input File Structure

As with previous versions of STOMP, the simulator is controlled through a text file, which must be entitled *"input"* for proper execution. This input file has a structured format composed of cards that contain associated groups of input data. Depending on the operational mode, input cards may be required, optional, or unused. Required cards must be present in an input file. Optional cards are not strictly required to execute the simulator, but may be required to execute a particular problem. Unused cards are treated as additional text that is unrecognized by the simulator but will not hinder a proper execution. Cards may appear in any order within the input file. However, the data structure within a card is critical and must follow the formatting directives described in the Users Guide (White and Oostrom 2006).

A STOMP input file is composed of cards, some of which are required and others that are optional or unused. The number of required cards depends on the operational mode. If an attempt is made to execute

the simulator on an *"input"* file with an incomplete set of required cards, an error message will be generated, and the code execution will stop. Optional cards are used to specify STOMP capabilities that may be required to execute a particular problem or generate desired output data. These cards are considered optional because the capabilities accessed through these cards are not necessarily required to execute the code. Execution of the simulator on input files with an incomplete set of optional cards yields messages that will note the missing optional cards but allow the execution to continue. The required and optional cards that comprise the input requirements for STOMP-WAE-B are summarized by Ward et al. (2005) and by White and Oostrom (2006). Input specific to this mode are five input cards that include 1) *Atmospheric Conditions Card* used to input local atmospheric conditions, 2) the *Plant Properties Card*, used to input time-invariant plant species data, 3) the *Boundary Conditions Card*, used to input time-varying plant species data and the traditional boundary condition data, 4) the *Thermal Properties Card*, used to enter traditional thermal properties data as well as parameters used to describe the bare surface albedo of rock/soil types used in the simulation, and 5) a gas injection/withdrawal well in the *Source Card*. Specific to the scalable implementation is the input needed for a parallel simulation with STOMP-WAE-B-Sc.

2.1.6.1 Source Card

Gas injection/withdrawal wells have been added to the *Source Card* in STOMP-WAE-B. The required inputs are the orientation of the well (X, Y, Z), gas pressure at the bottom of the well, well diameter, symmetry factor, minimum formation permeability, relative humidity, and temperature. The orientation of the well is determined by specifying either a "Z-Direction Injection Well," "X-Direction Injection Well," or a "Y-Direction Injection Well" and specifying a range of nodes in the appropriate direction. If the well gas pressure is greater than the formation pressure, gas will be injected into the formation. If the well gas pressure is less than the formation pressure, gas will be withdrawn from the formation. For gas withdrawal, the specified temperature will be ignored, and withdrawn gas will be at the formation temperature. The well diameter may be specified in any length unit allowed in other STOMP input. The symmetry factor is 1.0 if the well is in an interior node, 0.5 if the well is on a boundary that is a plane of symmetry, and 0.25 if the well is assumed to be along the corner of a domain. A very small minimum permeability may be specified if numerical difficulties are encountered with the nonlinear well model; otherwise, this parameter may be set to zero. For an injection well, the humidity and temperature of the injected gas may be specified.

2.1.6.2 Parallel Simulation Input

The input files for STOMP-WAE-B and STOMP-WAE-B-Sc are identical with two exceptions. In the *Solution Control Card*, the type of run, whether *Normal* or *Restart*, must be qualified with the phrase "w/PETSc" to specify the parallel solver. Also, in the *Grid Card*, the number of grids in the X-, Y-, and Z-directions must be followed by the number of processors required in each of those dimensions.

2.1.7 Parallel Simulation Output

The STOMP-WAE-B simulator can generate, depending on the requested output and saturation function type, data files for restarting a simulation and three types of simulation result files. Every execution produces an output file named *output*. If the simulation concludes without a fatal error, then a *restart.n* and a *plot.n* file are also generated. Restart and plot file names include extensions (i.e., *n*) that correspond

to the time step for which the file was written. For example, a restart file named *restart.39* would have been written at the conclusion of the 39th time step. A surface file named *surface* is generated whenever a surface flux card is included in the *input* file. All output files generated by the simulator (*output, restart.n, plot.n,* and *surface* files) are ASCII text files.

The STOMP-WAE-B-Sc simulator generates similar output files to STOMP-WAE-B. The output and surface files are identical in format. The restart and plot files differ in that, for the scalable version, there are two parts to each file, an ASCII file with header information named *restart90a.n* and *plot90a.n*, respectively. The field variables at each of the nodes are contained within binary files named *restart90.n* and *plot90.n* for each time step *n*. The *plot90a.n* and *plot90.n* files can be converted to Tecplot format ASCII text files for plotting, using the FORTRAN utility program named Plot90_to.

2.1.8   Solution Strategy

The general flow path for all operational modes of the STOMP simulator comprises three components, initialization, iteration, and closure. A flow chart for the initialization, iteration, and closure components of the main program is shown in Figure 2.2, where the enclosing boxes indicate either a single or group of routines. The initialization component of the program is executed once during a simulation. The routines in the initialization component are executed in the sequence shown in Figure 2.2, from the program start to the start of the first time step. The iteration component of the program contains a pair of nested loops, an outer loop for time stepping and an inner loop for Newton-Raphson linearization. The Newton-Raphson loop is terminated with a successful convergence or after an iteration limit violation. The time-stepping loop has been terminated after a simulation limit or a time-step reduction limit. Regardless of the cause for termination during the time-stepping loop, the closure routines are executed at the simulation completion.

Other than parallelization of individual DO-loops by the FP preprocessor, the main difference in code execution between STOMP-WAE-B and STOMP-WAE-B-Sc is the linear solver used. STOMP-WAE-B uses a serial solver named SPLIB (Bramley and Wang 1995), whereas STOMP-WAE-B-Sc uses a parallel solver named PETSc (Balay et al. 2007). Both solvers offer a selection of solution schemes, with the most efficient often being a variation of the iterative conjugate gradient method.

2.2   Application Examples

The value of a simulation model depends strongly on its capability to realistically generate an observation of response variables of interest. It is not unusual for initially parameterized simulation models to fail in their capability to accurately fit observed data. Thus, the situation is often corrected by adjusting the input parameters within reasonable limits and again comparing the output with observations. The process of comparing model output with observations is known as model verification. Validation, in contrast, compares output from a verified model with independent data and includes statistical analyses to quantify the goodness of fit. Verification is therefore an important step in a statistically rigorous validation and is required before a model can be certified as being capable of capturing responses for the major input variables and meteorological input.
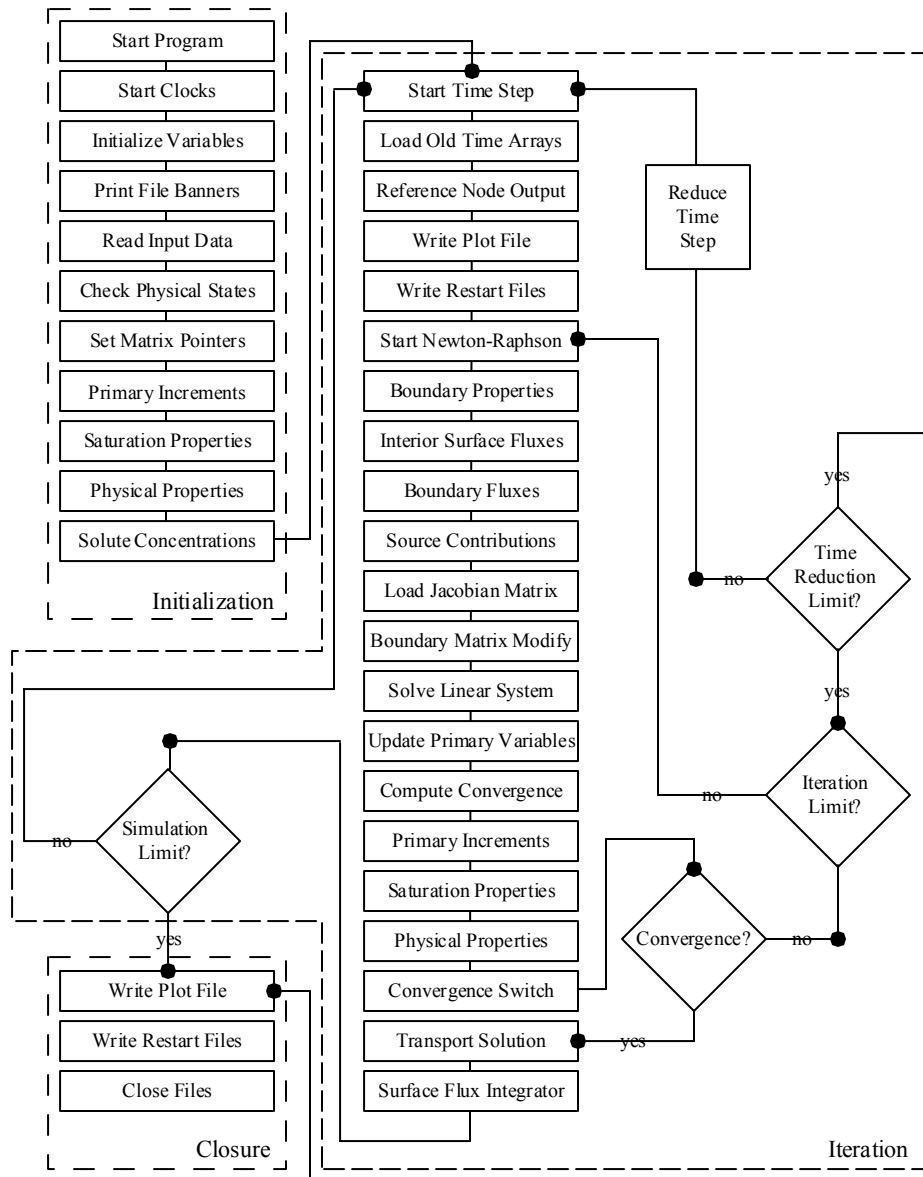
Figure 2.2. STOMP Solution Flow Chart

At present, there are no data available to allow verification of the desiccation process. Thus, model verification consisted of using the modified code to simulate a series of test problems, including those initially used to verify the sparse vegetation evapotranspiration model of STOMP-WAE-B (Ward et al. 2005). The test problems are identical to those used to verify the UNSAT-H code and included tests of infiltration, drainage, and heat flow (Fayer 2000). In addition to these test problems, two candidate engineered-barrier designs being considered for use at 216-UW-1 were simulated. The barrier simulations focused on the water-balance components, including transpiration, in 2-D cross sections. The selected problems are important in demonstrating the capability of the model to simulate the various processes that are impacted by meteorological forcings. To evaluate the model performance for 3-D field-scale problems, a simulation of the 299-E24-111 test (Sisson and Lu) site was performed.

2.2.1 2-D Simulation of a Water Balance in a Field-Scale Engineered Barrier

Two designs were considered in the 2-D simulations, the 80-cm thick monofill with a biointrusion layer and the 100-cm monofill with a biointrusion layer. Both designs consisted of 30-cm-thick silt with pea gravel admix underlain by a silt-loam layer of varying thicknesses, depending on the overall thickness of the barrier. For the 80-cm-thick barrier, the silt-loam layer varied from 0.21 m to 0.48 m, whereas in the 100-cm-thick design, it varied from 0.21 m to 0.68 m. The silt-loam layer was underlain by a 0.20-m-thick layer of compacted Environmental Remediation Disposal Facility (ERDF) spoil pile sediments that was placed on top of a 0.10-m-thick graded filter gravel. This filter was underlain by a 0.30-m-thick layer of ballast rock that formed the bio-barrier. The entire barrier was assumed to lie on top of a 6.6-m-thick zone of native sediment characterized as a gravel-dominated Hanford H1 unit.

The dimensions of the grid used in the 80-cm-thick profile were 62×1×59 (3658 cells) whereas the dimensions of the grid used for the 100-cm-thick profile was 63×1×65 (4095 cells). Horizontal discretization was variable, ranging from 0.32 m to a maximum of 7 m. The smallest cells were in the side-slope region where it was impossible to eliminate stair-stepping on the sloped surface. Vertical discretization ranged from 0.04 m to 1.6 m with the smallest cells occurring in fine-textured layers and near interfaces in the barrier. In general, cell sizes increased away from the barrier into the native H1 sediments. One shortcoming with this approach is that the ballast rock and the associated graded filter used to construct the bio-barrier were also rotated counterclockwise from the horizontal configuration to take on a 2% slope. However, it was estimated that the error due to this configuration would be quite small compared to that resulting from flow along stair-stepped interfaces. Both domains extended some 50 m from the west boundary to the crown at the east boundary. Simulations were performed using both the serial and parallel versions of STOMP.

2.2.1.1 Comparison of Serial and Parallel Results

The simulation with an 80-m-thick bio-barrier was executed in serial with both STOMP-WAE-B and STOMP-WAE-B-Sc, and in parallel with STOMP-WAE-B-Sc on a workstation, Pandora, which has dual quad-core 2.66-GHz Xeon 5355 processors, and the Environmental and Molecular Sciences Laboratory (EMSL) supercomputer mpp2, which has 900 dual-core 1.5-GHz Itanium-2 Madison processors. Figure 2.3 shows the difference in code execution time required for these different cases. STOMP-WAE-B-Sc runs in 74% of the time required by STOMP-WAE-B. This difference is largely due to the PETSc solver used in STOMP-WAE-B-Sc being more efficient than the SPLIB solver used by STOMP-WAE-B. On four processors, STOMP-WAE-B-Sc runs in 76% of the time it requires on one processor. Ideally, on four processors, this problem would run in 25% of the time required on one processor, but ideal scaleup is not achieved due to the overhead of inter-processor communication and redundant calculations. Execution of the same problem on eight processors on mpp2 is slightly slower because the individual processors are slower on mpp2. This is a fairly small problem, with only 62 × 59 grid cells. Problems with greater than 100,000 grid cells will benefit more from execution on the many processors available on mpp2 because the computation time required on each processor will be greater than the time needed for inter-processor communication.

Figure 2.4 shows a comparison of serial and parallel code time steps required vs. simulation time for a 2D simulation with 62 × 59 grid cells. Because time steps are automatically reduced when the linear solver does not converge, this is a measure of the similarity in convergence behavior between the two versions
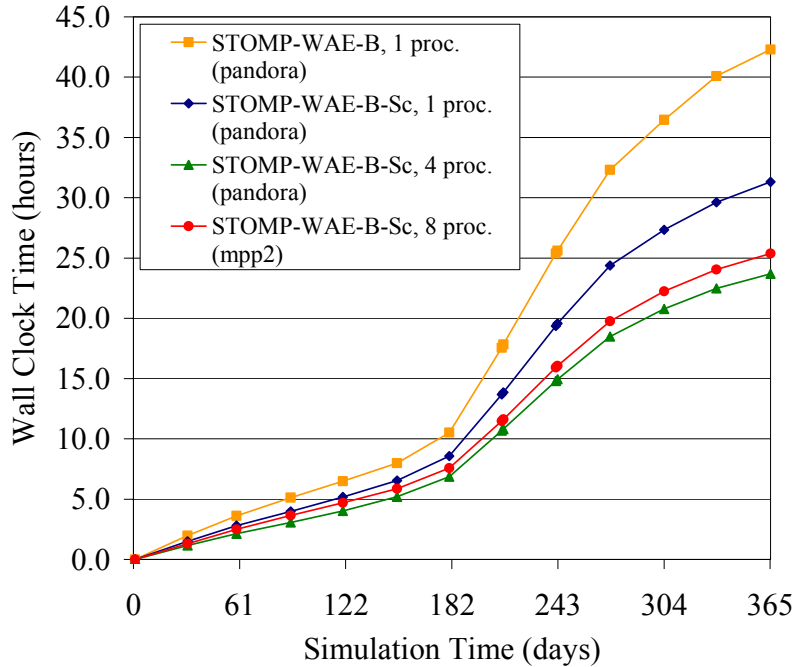
Figure 2.3. Comparison of Serial and Parallel Code Execution Time vs. Simulation Time for a 2D Simulation with 62 × 59 grid cells. Pandora is a dual quad-core 2.66-GHz Xeon 5355 workstation, whereas mpp2 has 900 dual-core 1.5-GHz Itanium-2 Madison processors.
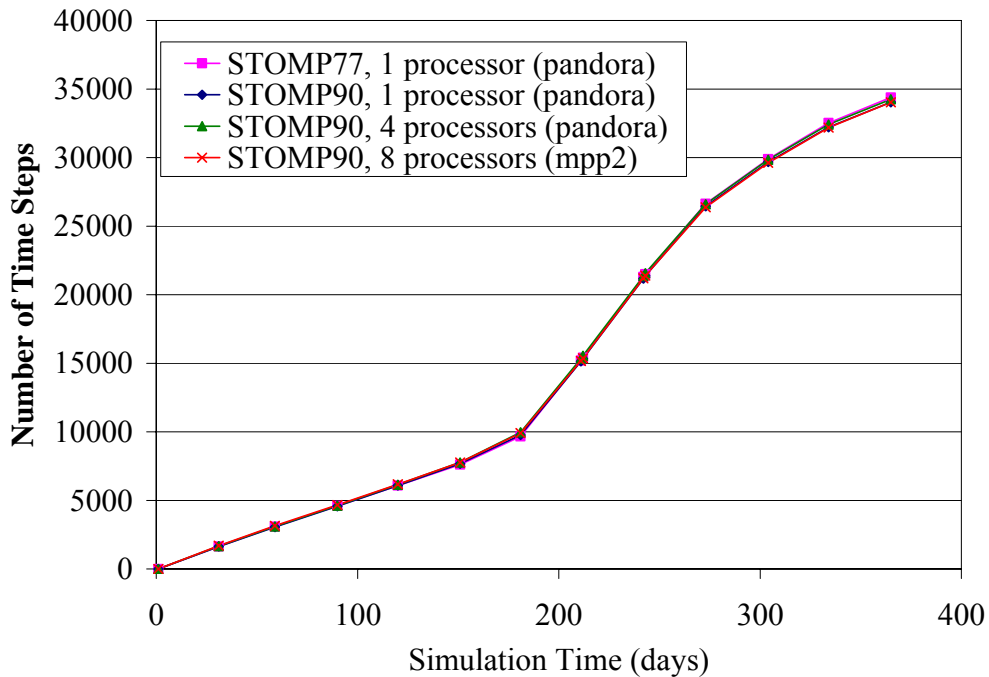
Figure 2.4. Comparison of Serial and Parallel Code Time Steps Required vs. Simulation Time for a 2D Simulation with 62 × 59 grid cells. Pandora is a dual quad-core 2.66-GHz Xeon 5355 workstation, whereas mpp2 has 900 dual-core 1.5-GHz Itanium-2 Madison processors.

of the code. The number of time steps taken is not appreciably different, indicating similarity in convergence behavior between STOMP-WAE-B and STOMP-WAE-B-Sc.

Results for STOMP-WAE-B and STOMP-WAE-B-Sc run in serial and parallel are comparable. Saturations predicted by serial STOMP-WAE-B (Figure 2.5) are virtually identical to those predicted by parallel STOMP-WAE-B-Sc (Figure 2.6). Temperatures also compare well between the serial (Figure 2.7) and new parallel (Figure 2.8) versions of the code. Calculated transpiration (Figure 2.9), evaporation (Figure 2.10), and runoff rates (Figure 2.11) calculated by the serial and parallel version of the code are also comparable.
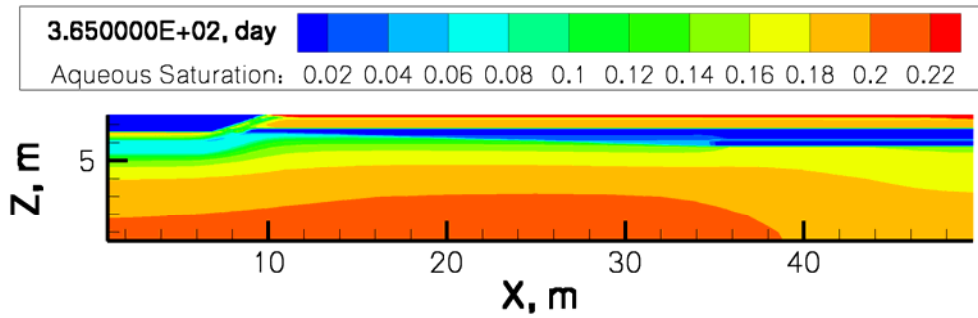
Figure 2.5. Saturations Predicted at 1 Year of Simulation Time by Serial STOMP-WAE-B
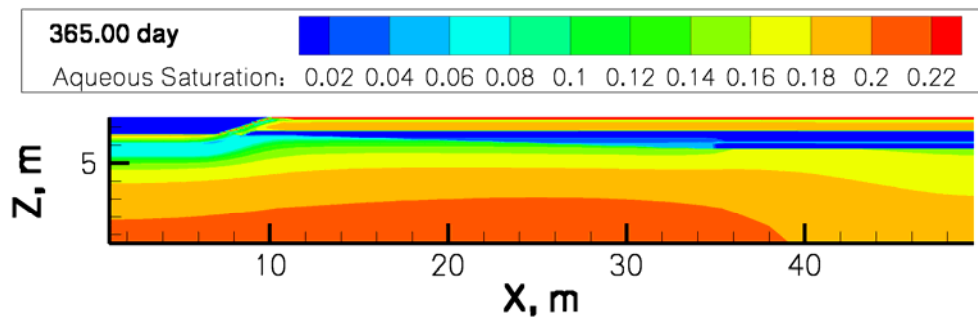
Figure 2.6. Saturations Predicted at 1 Year of Simulation Time by Parallel STOMP-WAE-B-Sc
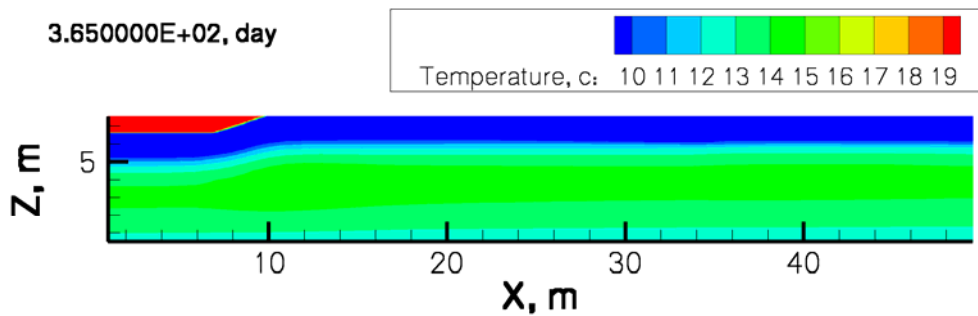
Figure 2.7. Temperatures Predicted at 1 Year of Simulation Time by Serial STOMP-WAE-B
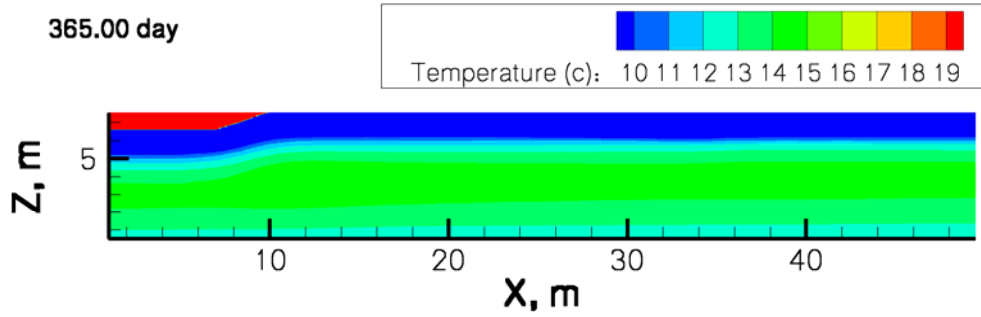
Figure 2.8. Temperatures Predicted at 1 Year of Simulation Time by Parallel STOMP-WAE-B-Sc
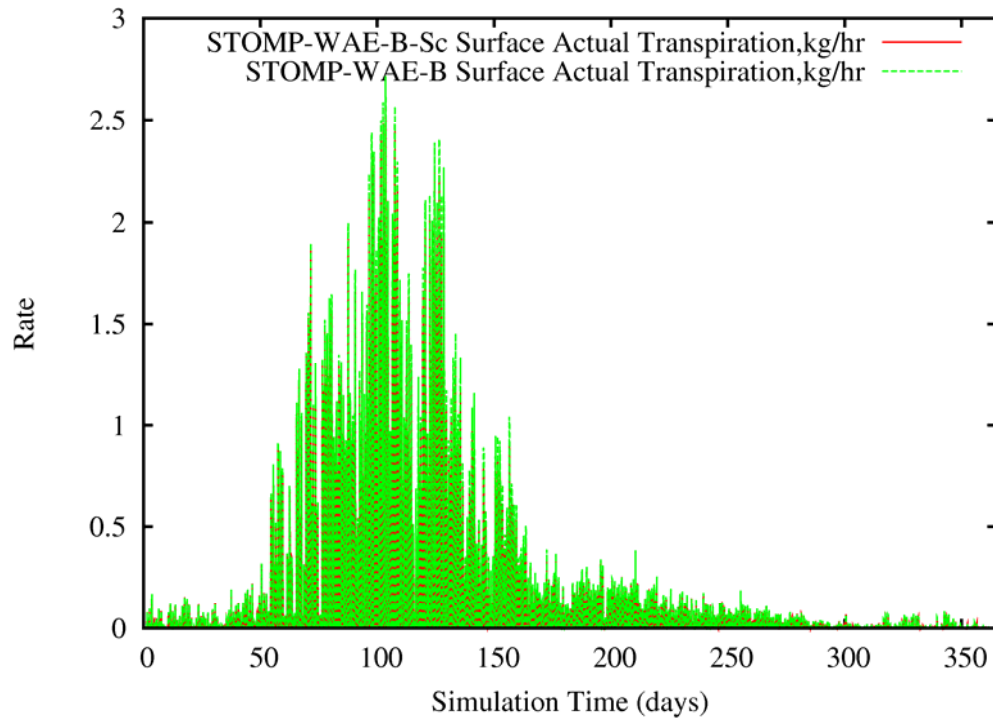
Figure 2.9. Comparison of Transpiration Rate Calculated by Serial STOMP-WAE-B and Parallel STOMP-WAE-B-Sc
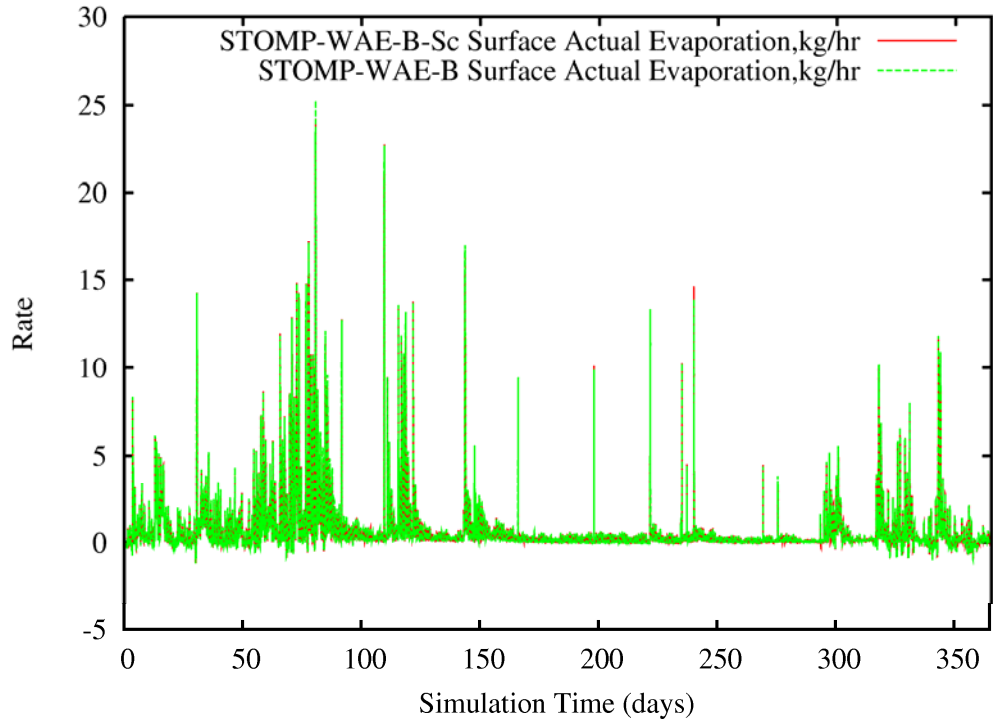
Figure 2.10. Comparison of Evaporation Rate Calculated by Serial STOMP-WAE-B and Parallel STOMP-WAE-B-Sc
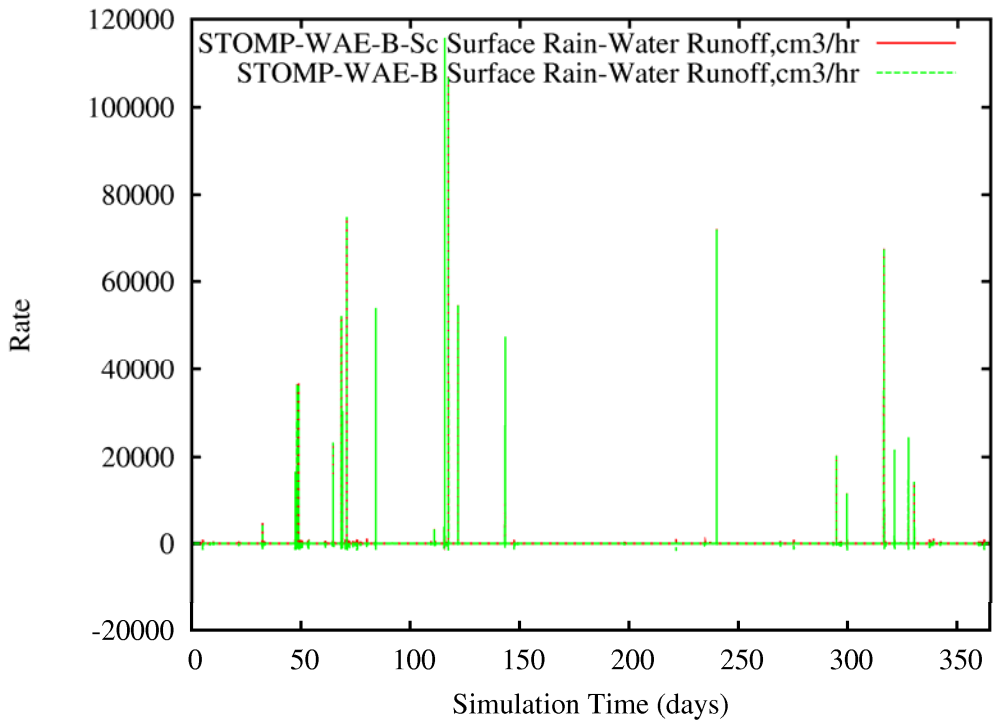
Figure 2.11. Comparison of Runoff Rate Calculated by Serial STOMP-WAE-B and Parallel STOMP-WAE-B-Sc

2.2.2   3-D Simulation of Sisson and Lu Test Site

A three-dimensional simulation of a soil-desiccation well operating at the Sisson and Lu Test site is presented as an example of the type of field-scale simulation that STOMP-WAE-B-Sc was designed for. This problem was run as a test of the 3D capabilities of the code. Comparisons with STOMP-WAE-B have not yet been performed but are planned for FY08. The initial gas pressure in the formation was assumed to be 101,325 Pa. The injection-well gas pressure was 103,000 Pa, and the injection well gas temperature was 80°C. Temperature increased around the injection well (Figure 2.12) and water saturations decreased (Figure 2.13) because of the injection of hot, dry air.

2.3   Summary

STOMP-WAE-B has been enhanced by adding gas injection/withdrawal wells for soil-desiccation studies. Input for these well models is specified in the Source Card. STOMP-WAE-B is now available for scalable execution on multiple processor (i.e., parallel) computers. The parallel version of the simulator is written in pure FORTRAN 90 with embedded directives that are interpreted by a FORTRAN preprocessor. Without the preprocessor, the scalable version of the simulator can be executed sequentially on a single processor computer.
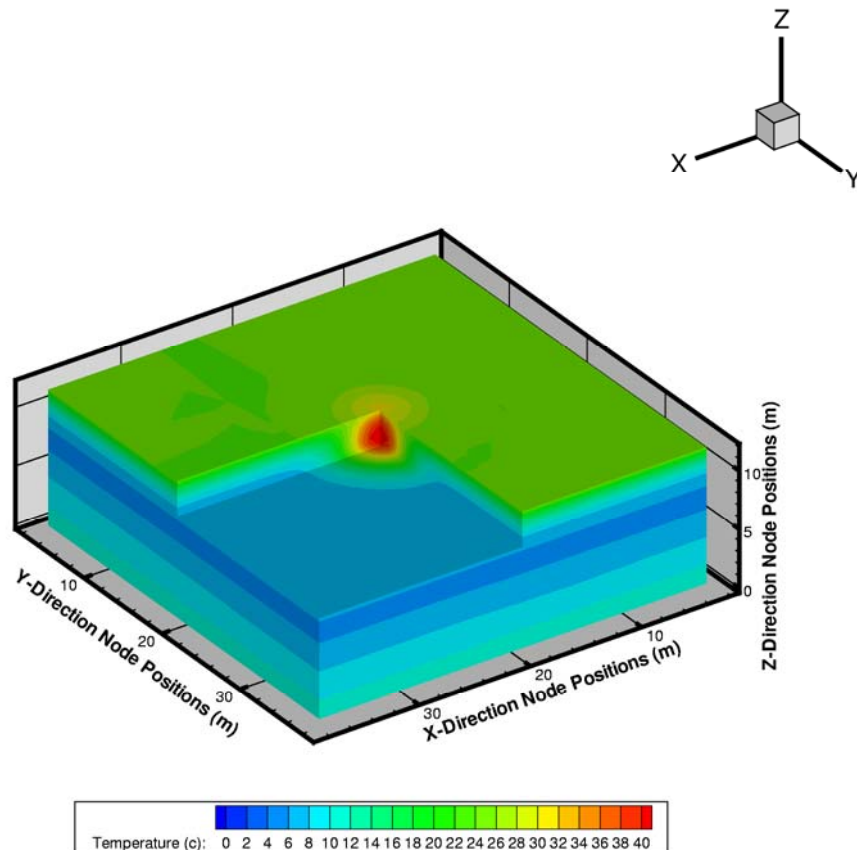
Figure 2.12.   Temperatures Predicted at Sisson-Lu site with Hot Air Injection Well at 133 Days of Simulation Time by Parallel STOMP-WAE-B-Sc
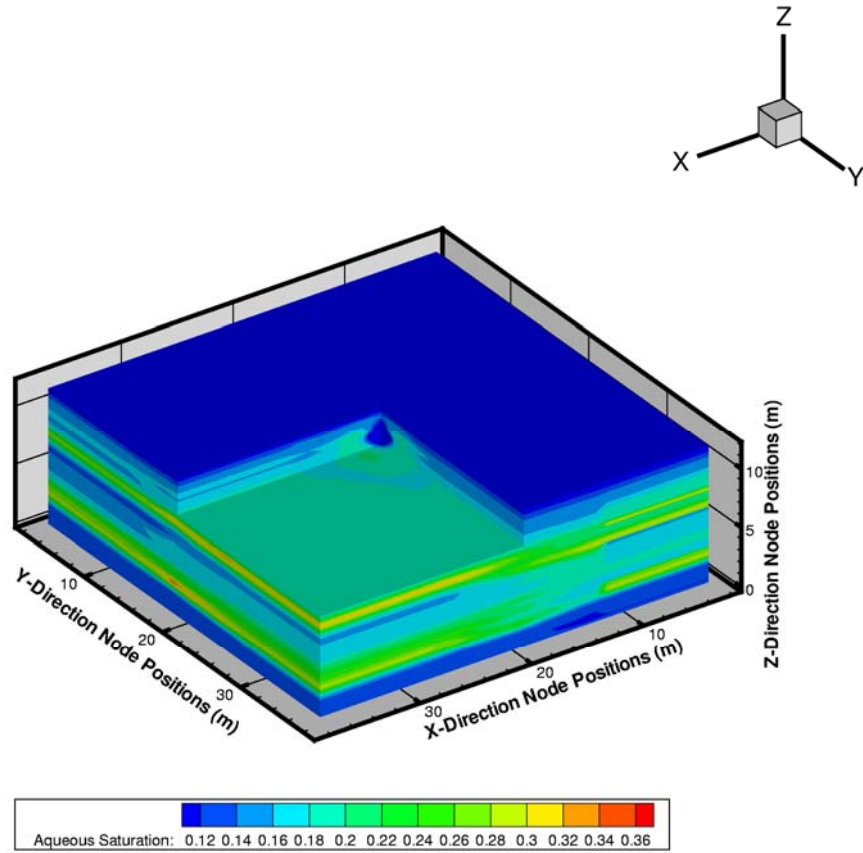
Figure 2.13. Saturations Predicted at Sisson-Lu Site with Hot Air Injection Well at 133 Days of Simulation Time by Parallel STOMP-WAE-B-Sc

3.0 Intermediate-Scale Laboratory Desiccation Experiments

One of the three knowledge gaps identified by the expert panel convened to evaluate deep vadose zone remedial technologies was a need for focused laboratory experiments to demonstrate the technique and to address technical concerns related to the energy balance and osmotic effects (FH 2006). Another gap was related to the potential for remobilization after the desiccation period. Both of these knowledge gaps are best addressed through detailed intermediate-scale experimentation. Thus, in response to these needs, a series of intermediate scale flow cell experiments were designed and conducted as a first step in quantifying how the energy balance impacts the capability of desiccation to limit the downward migration of contaminants as driven by water infiltration. The objectives of this series of experiments were threefold, 1) to demonstrate the desiccation process at the intermediate scale, 2) to develop a detailed temperature and relative humidity data set, and 3) to test and verify the water-air-energy mode of the STOMP simulator (White and Oostrom 2006).

3.1 Materials and Methods

3.1.1 Flow-Cell Experiments

A total of four experiments, one in homogeneous and three in heterogeneous sand packs, were conducted in a wedge-shaped intermediate-scale flow cell. Details of the experiments are presented in Table 3.1. Schematics of the flow cell for the homogenous and heterogeneous experiments are shown in Figure 3.1.

Table 3.1. Overview of the Conducted Flow-Cell Experiments. In all experiments, 22°C air was injected with a rate of 2 L/min.

Experiment	Sand	Insulation	Sand Mass (kg)	Water Mass (kg)
HOM1[a]	40/50	2.54 cm PVC[c] foam sheet	17.1	0.427
HET1[b]	40/50 matrix; 70 inclusion	None	40/50: 12.7 70: 3.98	40/50: 0.318 70: 0.200 *Total:* 0.518
HET2	40/50 matrix; 70 inclusion	2.54 cm PVC foam sheet	40/50: 12.7 70: 3.98	40/50: 0.318 70: 0.200 *Total:* 0.518
HET3	40/50 matrix; 70 inclusion	5.08 cm PVC foam sheet	40/50: 12.7 70: 3.98	40/50: 0.318 70: 0.200 *Total:* 0.518
(a) HOM1 = homogeneous experiment (b) HET1, 2, 3 = heterogeneous experiments (c) PVC = polyvinyl chloride				

The medium-grained 40/50-mesh and fine-grained 70-mesh Accusands were obtained from the Unimin Corporation (Le Sueur, MN). The flow-cell had a wedge angle of 20 degrees, with an internal thickness of 6.25 cm, and was made out of $^3/_8$-in. polycarbonate. The flow cell was packed with 80 cm of moist

porous media, occupying a volume of 9.425 L. The 40/50-mesh and 70-mesh sands were mixed with 25 g and 50 g water per kg, respectively. Figure 3.2 shows photographs of the wedge-shaped flow cell packed with Accusands. Figure 3.2a shows the homogeneous pack of 40/50 Accusand while Figure 3.2b shows the heterogeneous pack consisting of 70-mesh sand zone emplaced in a 40/50-mesh matrix. Experiments conducted in the heterogeneous pack were also designed to investigate the effects of insulation. Thus, an additional variable of interest was the amount of PVC foam insulation (McMaster-Carr, Los Angeles, CA) on the outside of the flow cell.
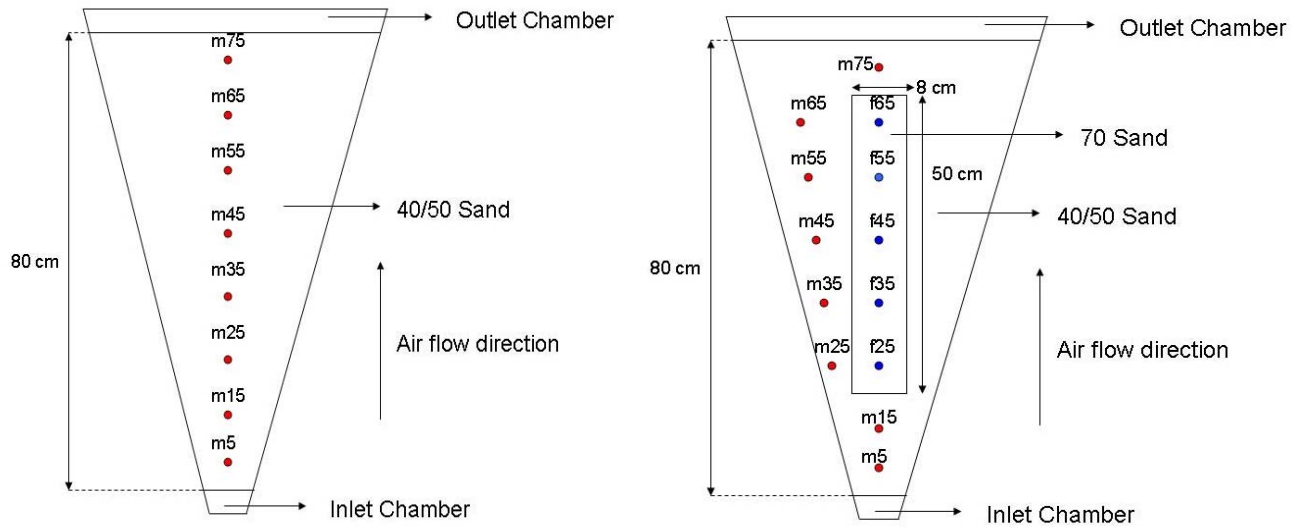
Figure 3.1.   Schematic of Wedge-Shaped Flow Cell Used for the (a) Homogeneous-Porous Media Experiment (HOM1) with 40/50 mesh Accusand. The red dots indicate the location of the temperature/humidity probes (m5, m15, m25, m35, m45, m55, m65, and m75), and (b) heterogeneous experiments (HET1, HET2, and HET3. The blue dots indicate the location of the temperature/humidity probes (f25, f35, f45, f55, and f65) in the fine-grained sand. The red dots indicate the location of the temperature/humidity probes (m5, m15, m25, m35, m45, m55, m65, and m75) in the medium-grained sand.

In all experiments, air was injected with a constant rate of 2 L/min at 22°C. The rate was controlled using an Alicat Scientific (Tucson, AZ) flow controller in combination with a custom-designed J-KEM gas temperature controller. The air was injected into an inlet chamber before it moved into the porous media (Figure 3.1 and Figure 3.3). The temperature and relative humidity were measured with Precon sensors (Kele Company, Memphis, TN). The probes were calibrated at relative humidity values of 0 and 100%. In experiment HOM1, eight probes were installed with an internal distance of 10 cm (m5, m15, m25, m35, m45, m55, m65, and m75). The number in the probe name indicates the distance from the gas inlet chamber. In experiments HET1, HET2, and HET3, eight probes were located in the medium-grained sand (m5, m15, m25, m35, m45, m55, m65, and m75) and five probes in the fine-grained sand (f25, f35, f45, f55, and f65). The out-flowing air was channeled through a PVC-foam wedge placed on top of the flow cell (Figure 3.3). This inverted wedge had a 0.1-cm opening at the top that was kept at 100%
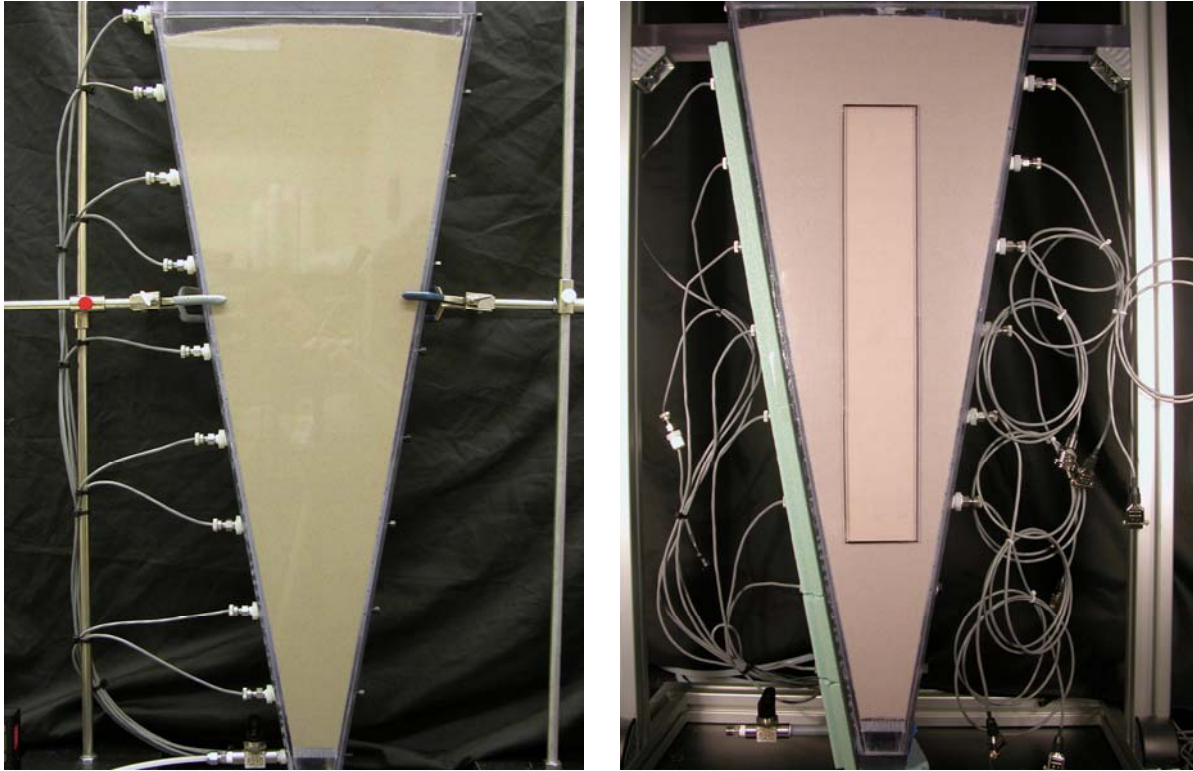
Figure 3.2. Photographs of Flow Cell Packed with Accusands, (a) Homogeneous Pack of Medium-Grained 40/50 Accusand and (b) a Heterogeneous Pack 70-Mesh Sand Zone Emplaced in a 40/50-Mesh Matrix

relative humidity. The upper wedge structure allowed for temperature and humidity control of the upper porous medium boundary.

3.1.2   Numerical Simulations

The experiments were simulated with the standard version of the water-air-energy mode of the STOMP simulator (White and Oostrom 2006). This mode uses the same general mass and energy conservation equations as the STOMP-WAE-B mode. The configuration of the heterogeneous experiments requires the use of a three-dimensional model. Since the experiments are symmetric in the horizontal x- and y-directions, only one quarter of the total experimental domain was modeled. To evaluate the effect of the insulation material, both the polycarbonate flow cell wall and the PVC foam sheet were explicitly included in the model as porous media (Table 3.2). For this model configuration, boundary conditions for the three equations were needed at the bottom, top, and the front side of the flow cell. For all other boundaries (back, west, and east sides), zero flux conditions were imposed. For the energy equation, the incoming dry air and the wall temperature were assumed to be at 22°C. An outflow boundary condition was imposed at the top of the porous medium. For the injected air, a constant flux (Neumann) boundary condition was used at the bottom by dividing the injection rate by the cross-sectional area, and a constant (atmospheric) pressure was maintained at the top and side of the flow cell. No water was allowed to be transported across the boundaries. The porous media, with a modeled thickness of 6.25 / 2 = 3.125 cm,

Figure 3.3. Insulated Flow Cell (1-in. PVC foam; Experiment HET2) with Chimney to Control Outflow Boundary Conditions

were discretized into cells with dimensions of $0.5 \times 1.0416 \times 1.0$ cm in the x, y, and z direction, respectively. The polycarbonate wall and PVC insulation were discretized into three cells per material. The porous medium and thermal properties of the sands and wall materials are listed in Table 3.2. The thermal properties of the sands were obtained using a KD2 thermal properties analyzer (Decagon Devices, Inc., Pullman, WA). The thermal properties of the polycarbonate and PVC were obtained from the manufacturer (McMaster-Carr, Robbinsville, NJ). A relation from Somerton et al. (1974) was used to compute the thermal conductivity as a function of water saturation. The hydraulic properties of the polycarbonate and PVC foam were chosen to avoid any air or water movement in these materials. A sensitivity analysis showed that the values for these materials, as listed in Table 3.2, were appropriate.

3.2   Results and Discussion

Observed and simulated temperatures and relative humidity as a function of time for all probes are shown in Figure 3.4 and Figure 3.5, respectively, for experiment HOM1. Figure 3.4 shows that the predicted temperature values match the experimental results well, although the predicted values closest to the inlet chamber (at locations m5 and m15; Figure 3.1) show more cooling than the observed temperatures. The simulated values indicate a cooling down to $\sim 10^{o}$C, while the observed values were not smaller than $\sim 12^{o}$C. The cooling decreased with increased distance from the inlet chamber. This result is related to the decreased air velocity and heat transport through the insulation and the wall into the porous

Table 3.2. Hydraulic and Thermal Properties of the Sand, Wall, and Insulation Material

Property	40/50 Sand	70 Sand	Poly-Carbonate	PVC Foam
Hydraulic Conductivity (cm/min)	4.33[a]	0.9[b]	10^{-5}	10^{-5}
Brooks-Corey Entry Pressure Head (cm)	19.4[a]	41.0[b]	10^{5}	10^{5}
Brooks-Corey Pore Geometry Factor	6.17[a]	5.8[b]	5	5
Irreducible Water Saturation	0	0	0	0
Porosity	0.32	0.40	10^{-5}	0.97[c]
Initial Saturation	0.142	0.181	10^{-5}	10^{-5}
Heat Capacity (J/ kg K)	773	781	914[c]	816[c]
Unsaturated Thermal Conductivity (W/ m K))	0.21	0.19	0.61[c]	0.036[c]
Saturated Thermal Conductivity (W/ m K))	2.51	2.16	0.61[c]	0.036[c]
(a) Schroth et al. (1996)				
(b) Oostrom et al. (2005)				
(c) McMaster-Carr, Los Angeles, CA				

medium. Differences between the temperatures at the various locations at the end of the experiment are artifacts of the PreCon temperature probes. Both the experiment and the simulations showed a rapid decrease in relative humidity when the drying front passed (Figure 3.6). For all locations, the experimental drying fronts arrived a few hours earlier than the predicted fronts, which is reasonable given the duration of the experiment. The water in the flow cell was completely removed after 10 days of desiccation. In Figure 3.6, the observed temperature and relative humidity values at all locations are shown in a single plot. The plot shows that, consistent with theory, the timing of the minimum temperatures coincide with the passage of the drying fronts.
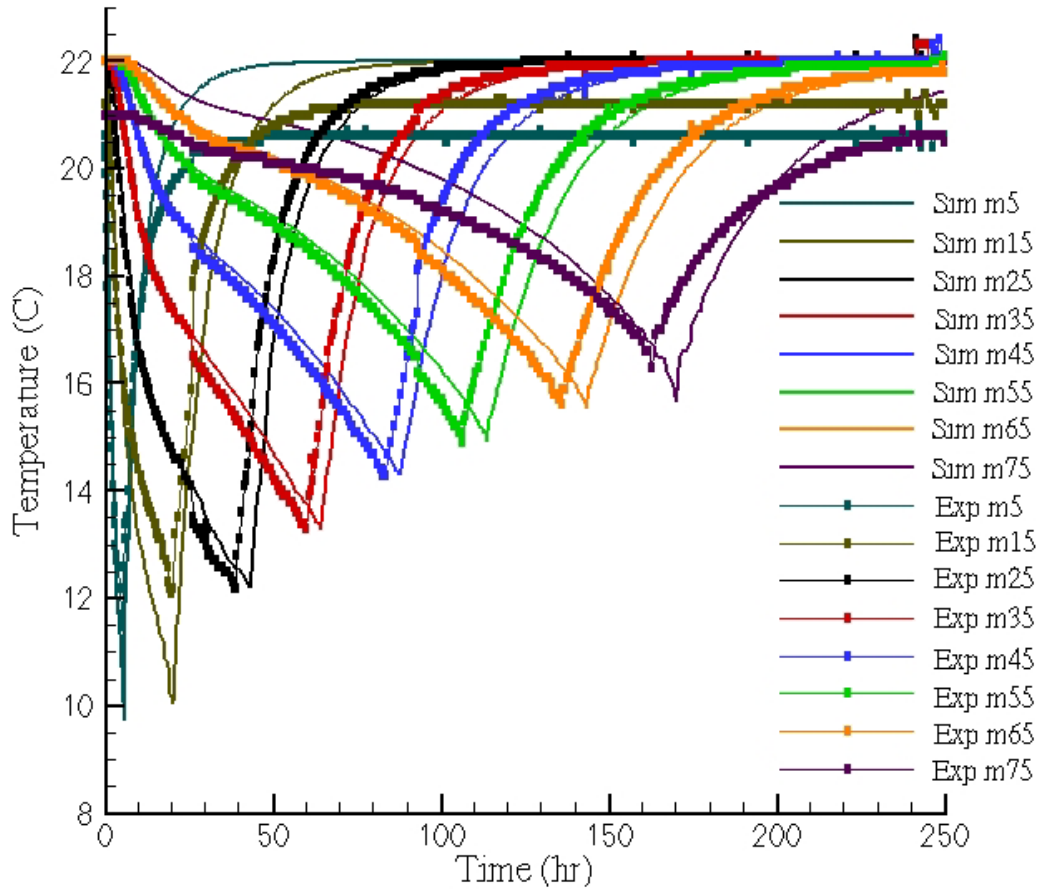
Figure 3.4. Observed (symbols) and Simulated Temperatures (solid lines) for Experiment HOM1
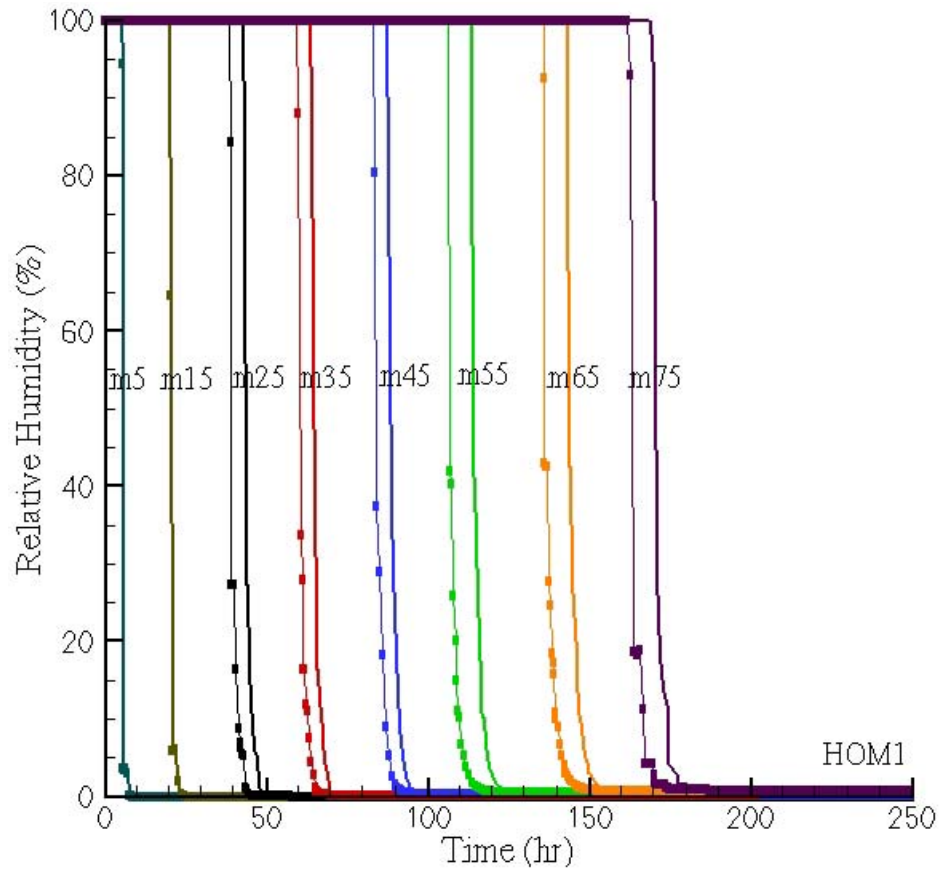
Figure 3.5. Observed (symbols) and Simulated Relative Humidity (solid lines) for Experiment HOM1
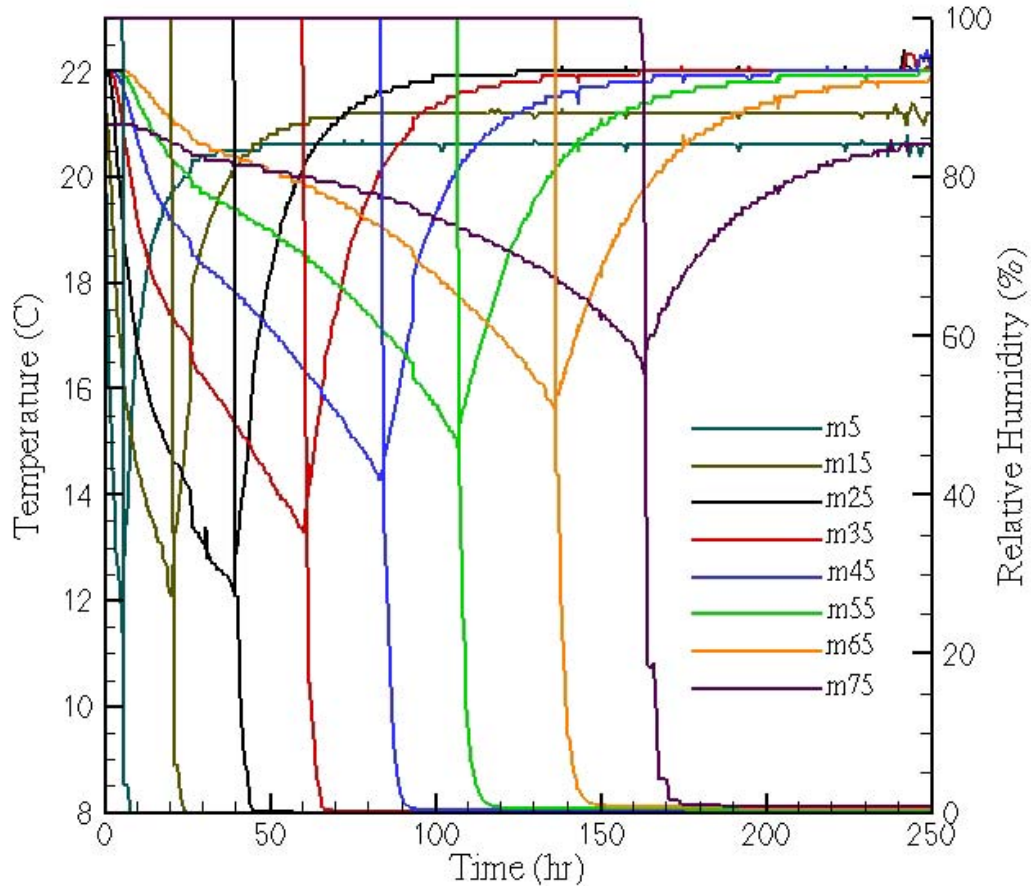
Figure 3.6. Observed Temperature and Relative Humidity Behavior for Experiment HOM1

When comparing the effects of the inclusion of the 70-sand zone, the results of experiment HOM1 need to be compared to experiment HET2. The observed and simulated temperatures for HET2 are shown in Figure 3.7 and Figure 3.8 for selected locations in the medium-grained and fine-grained sand, respectively. The relative humidity results are shown in Figure 3.9 for the locations in the medium-grained sand and in Figure 3.10 for all locations in the fine-grained sand. Temperature and relative humidity comparisons for the probes in the medium- and fine-grained sand at $z = 35$ cm are depicted in Figure 3.11. Similar to experiment HOM1, the temperature results for experiment HET2 show the most pronounced evaporative cooling near the inlet (Figure 3.7). In the medium grained sand, the observed cooling resulted in a minimum temperature of approximately 12°C at 5 cm from the inlet, with gradually less cooling for a minimum temperature of ~20°C at 5 cm from the upper boundary (Figure 3.7). The temperature plots for the fine-grained sand show two local minima (Figure 3.8). The first minimum is associated with the cooling due to evaporation in the adjacent medium-grained sand. The second minimum, which occurs later in time, is correlated with the evaporative cooling in the fine-grained sand itself. The cause of these cooling trends can be derived from relative-humidity plots for experiment HET2, shown in Figure 3.9 and Figure 3.10 for the probes in the medium- and fine-grained sands. The first minimum occurred when the relative humidity in the medium-grained sand started to decrease (Figure 3.9). The second minimum occurred when the relative humidity in the fine-grained sand decreased (Figure 3.10). The relative humidity in the fine-grained sand dropped relatively fast from 100 to 0% when the drying front passed by. The relative humidity decrease in the medium-grained sand was

fast from 100 to about 30%, but slowed down considerably after that (Figure 3.9). The long tailing period of decreasing relative humidity is the result of water vapor moving into the medium-grained sand from the fine-grained sand, after the medium-grained sand had been desiccated. Although the water in the medium-sand disappeared before the water saturations started to decrease in the fine-grained sand, the relative humidity in the medium-grained sand was affected for a considerable time because of the continued desiccation in the fine-grained sand. In general, the predicted time for the decrease in relative humidity in the medium-grained sand, when the fine-grained sand is desiccated, is typically longer than was observed in the experiments. Figure 3.11, depicting comparisons in relative humidity and temperature between adjacent probes at $z = 35$ cm, shows an increasing time lag in desiccation between the medium- and fine-grained sand with increasing distance from the inlet.

Figure 3.7. Observed (symbols) and Simulated Temperature (solid lines) at Locations m15, m35, m55, and m75 for Experiment HET2

Figure 3.8. Observed (symbols) and Simulated Temperature (solid lines) at the Locations in the Fine-Grained Sand for Experiment HET2

Figure 3.9. Observed (symbols) and Simulated Relative Humidity (solid lines) at Locations m15, m35, m55, and m75 for Experiment HET2

Figure 3.10. Observed (symbols) and Simulated Relative Humidity (solid lines) at the Locations in the Fine-Grained Sand for Experiment HET2

Figure 3.11. Observed Temperature and Relative Humidity Behavior at Locations m35 and f35 for Experiment HET2

The effects of insulation on desiccation of the same heterogeneous system are apparent when comparing results of experiments HET1, HET2, and HET3. Results for experiment HET1 (no insulation) are shown in Figure 3.12 through Figure 3.16. The observed and simulated temperatures are shown in Figure 3.12 and Figure 3.13 for selected locations in the medium-grained and fine-grained sand, respectively. The relative humidity results are shown in Figure 3.14 and Figure 3.15 for the locations in the medium- and fine-grained sands, respectively. Temperature and relative humidity comparisons for the locations in the medium- and fine-grained materials at $z = 35$ cm are depicted in Figure 3.16. Unfortunately, probe f65 for this experiment failed directly from the start of the desiccation process, and no data could be collected. Results for experiment HET 3 (double the PVC foam insulation) are depicted in Figure 3.17 through Figure 3.21. The observed and simulated temperatures are shown in Figure 3.17 and Figure 3.18 for selected locations in the medium-grained and fine-grained sand, respectively. The relative humidity results are shown in Figure 3.19 and Figure 3.20, for the locations in the medium- and fine-grained sands, respectively. Temperature and relative humidity comparisons for the locations in the medium- and fine-grained sand at $z = 35$ cm are depicted in Figure 3.21. The results show that the experiment with more insulation (HET3) resulted in increased cooling and a slightly slower desiccation of primarily the fine-grained sand. Differences in desiccation of the medium-grained sand were small. Removing all insulation (experiment HET1) resulted in lesser cooler and generally higher temperature during

3.13

desiccation. Desiccation of the fine-grained sand was faster in the non-insulated experiment HET1 than for the insulated heterogeneous experiment HET3.

A comparison of the removed water mass as a function in time for the three heterogeneous experiments is shown in Figure 3.22. The results reflect the fact that one quarter of the actual domain was included in the simulations. Since, according to Table 3.1, a total of 518 g of water was added for each experiment, 129.5 g of water was initially present in the simulations using one quarter of the domain. It can be seen from this plot that the differences in desiccation time for the three experiments was relatively small. This observation is interesting because of the considerable differences in temperature behavior between the three experiments. These results show that the gas that is initially passing through cooler zones is able to increase its vapor concentration when moving through warmer, moist porous media higher up in the flow cell. Given sufficient time, complete desiccation was obtained for all three experiments with heterogeneous systems.

Although some minor differences were observed, the presented results clearly demonstrate that the STOMP water-air-energy mode was able to simulate desiccation and the associated thermal behavior well in both homogeneous and relatively simple heterogeneous systems. The numerical results were obtained using independently determined hydraulic and thermal properties. The good match for both temperature and relative humidity data shows that the STOMP simulator is using appropriate conservation equations and constitutive relations to describe the experimental observations.
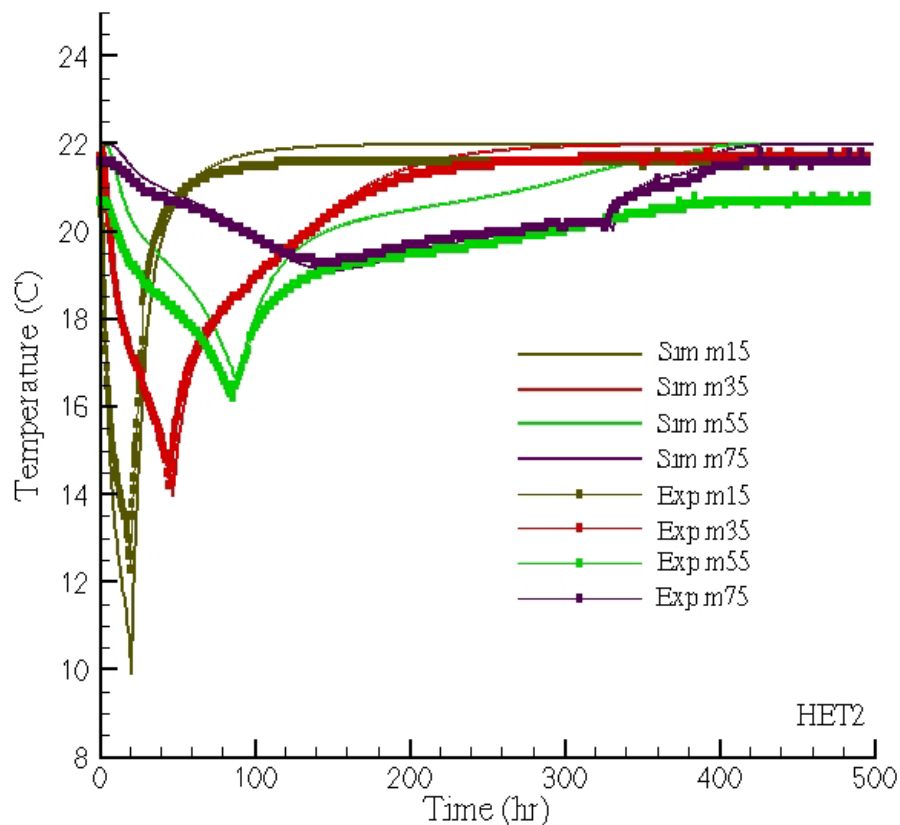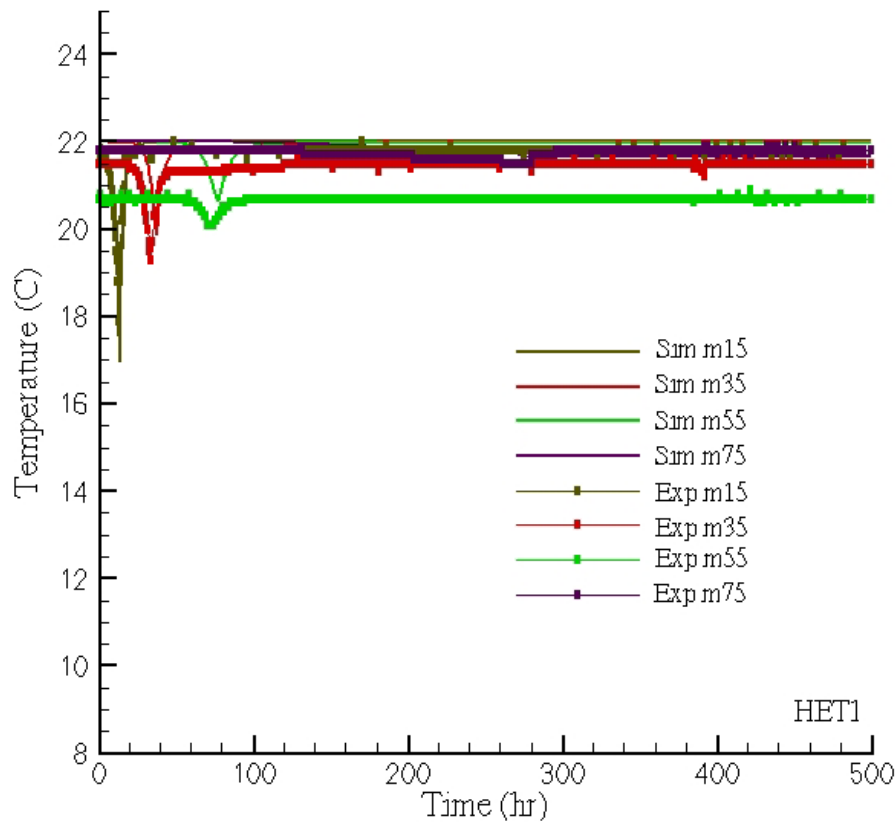

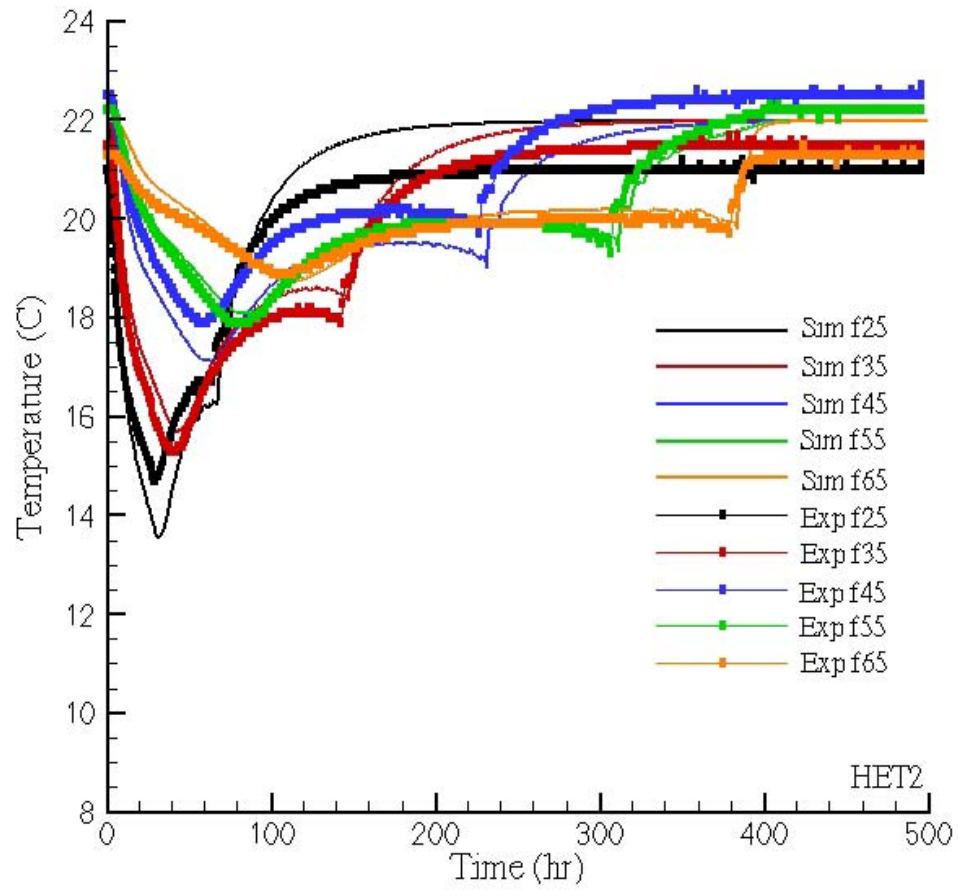**Figure 3.12.** Observed (symbols) and Simulated Temperature (solid lines) at Locations m15, m35, m55, and m75 for Experiment HET1

Figure 3.13. Observed (symbols) and Simulated Temperature (solid lines) at the Locations in the Fine-Grained Sand for Experiment HET1
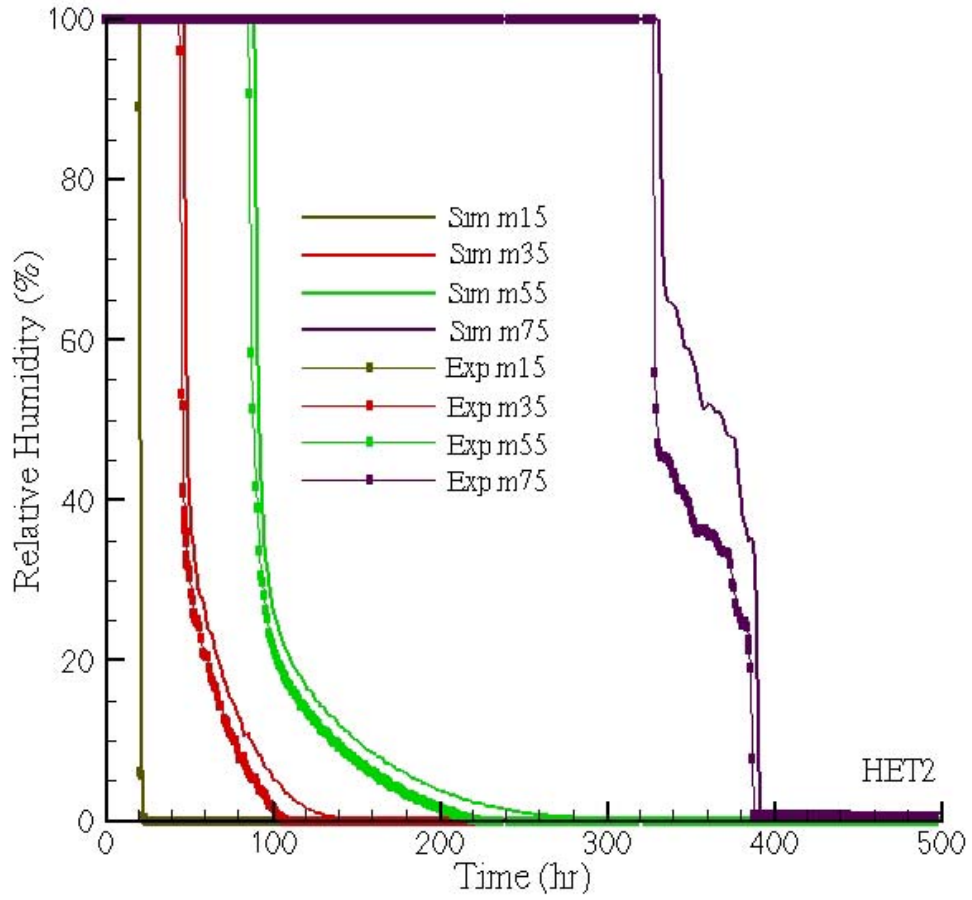
3.15

Figure 3.14. Observed (symbols) and Simulated Relative Humidity (solid lines) at Locations m15, m35, m55, and m75 for Experiment HET1
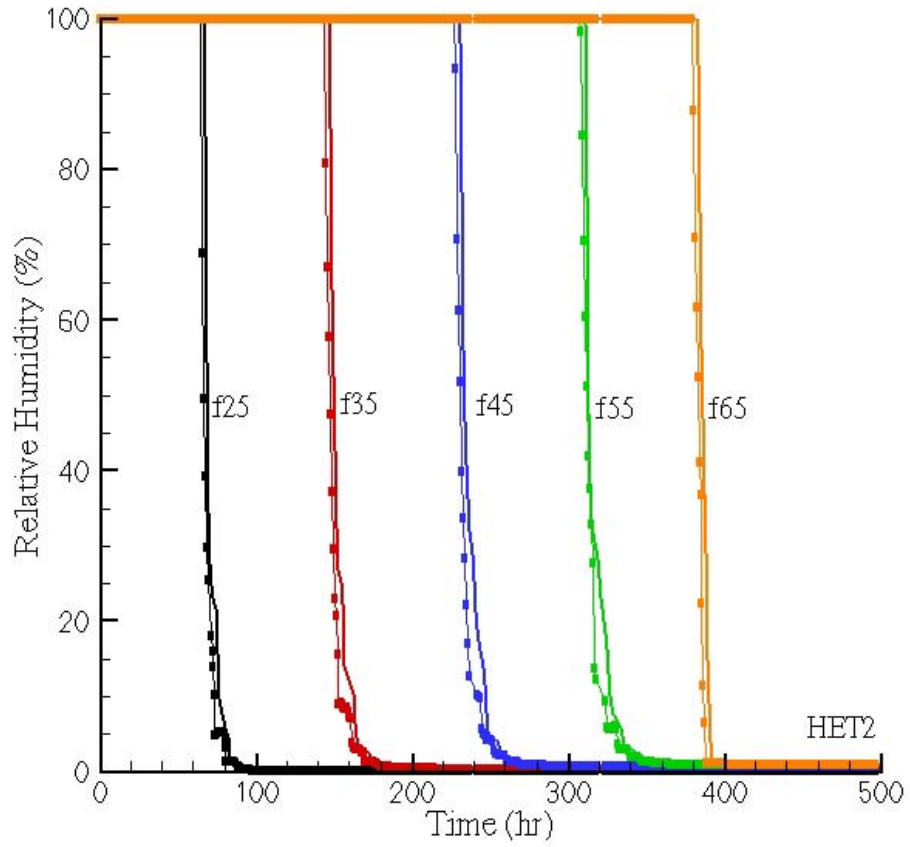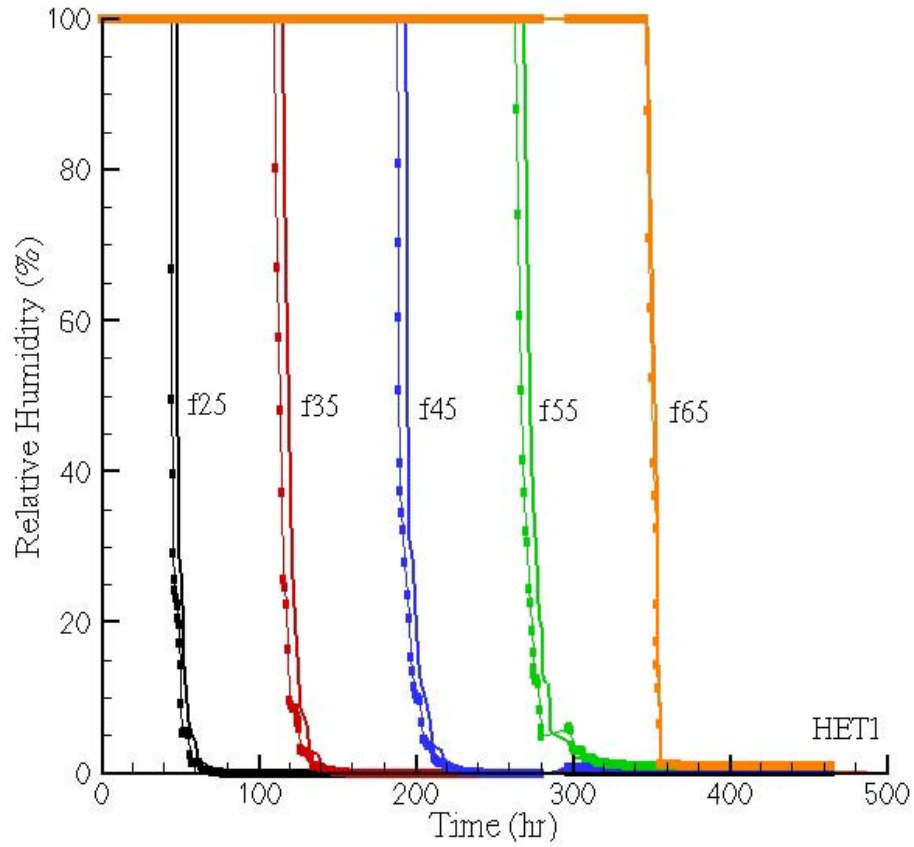
Figure 3.15. Observed (symbols) and Simulated Relative Humidity (solid lines) at the Locations in the Fine-Grained Sand for Experiment HET1
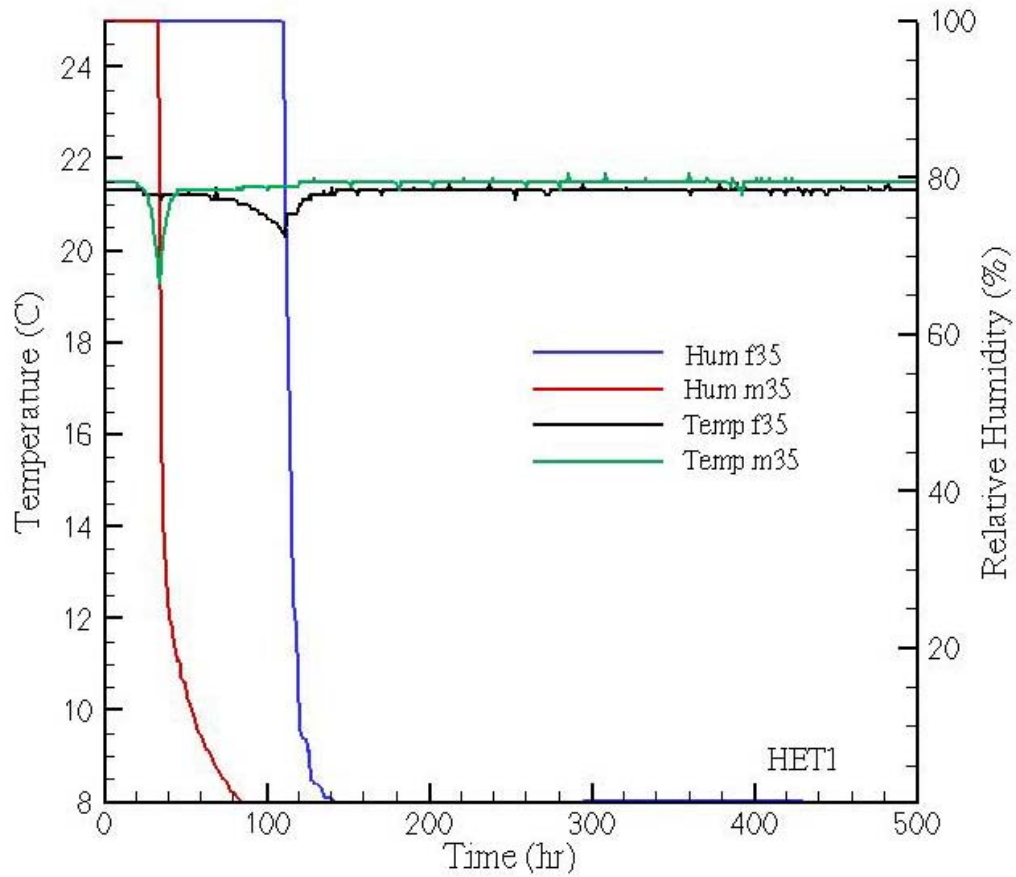
Figure 3.16. Observed Temperature and Relative Humidity Behavior at Locations m35 and f35 for Experiment HET1
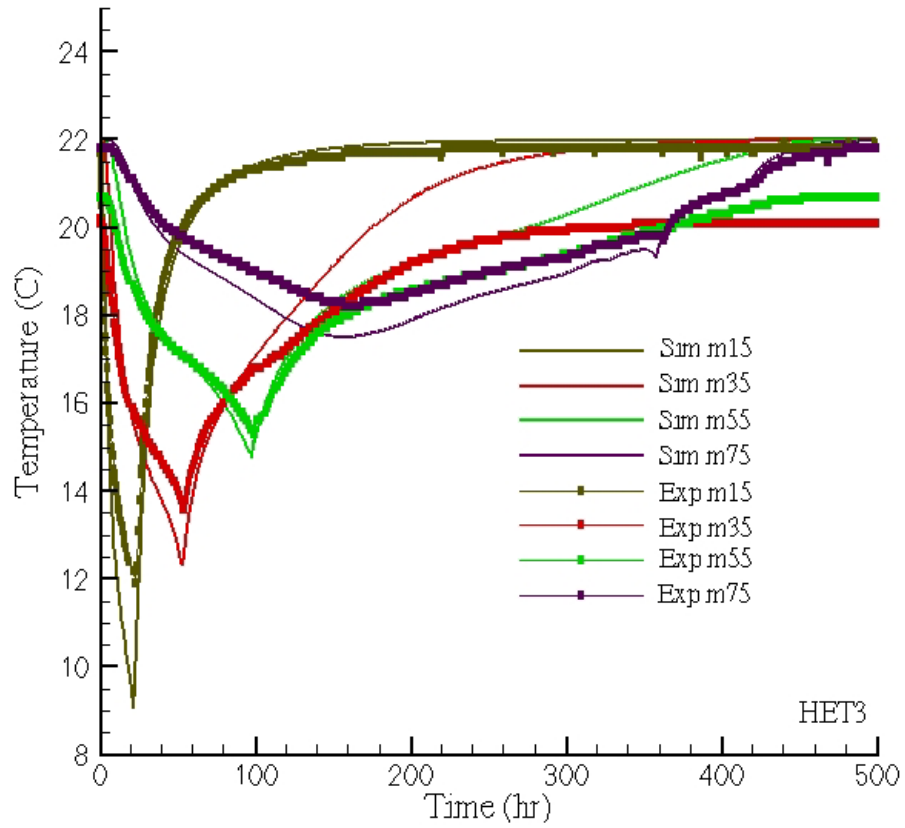
Figure 3.17. Observed (symbols) and Simulated Temperature (solid lines) at Locations m15, m35, m55, and m75 for Experiment HET3
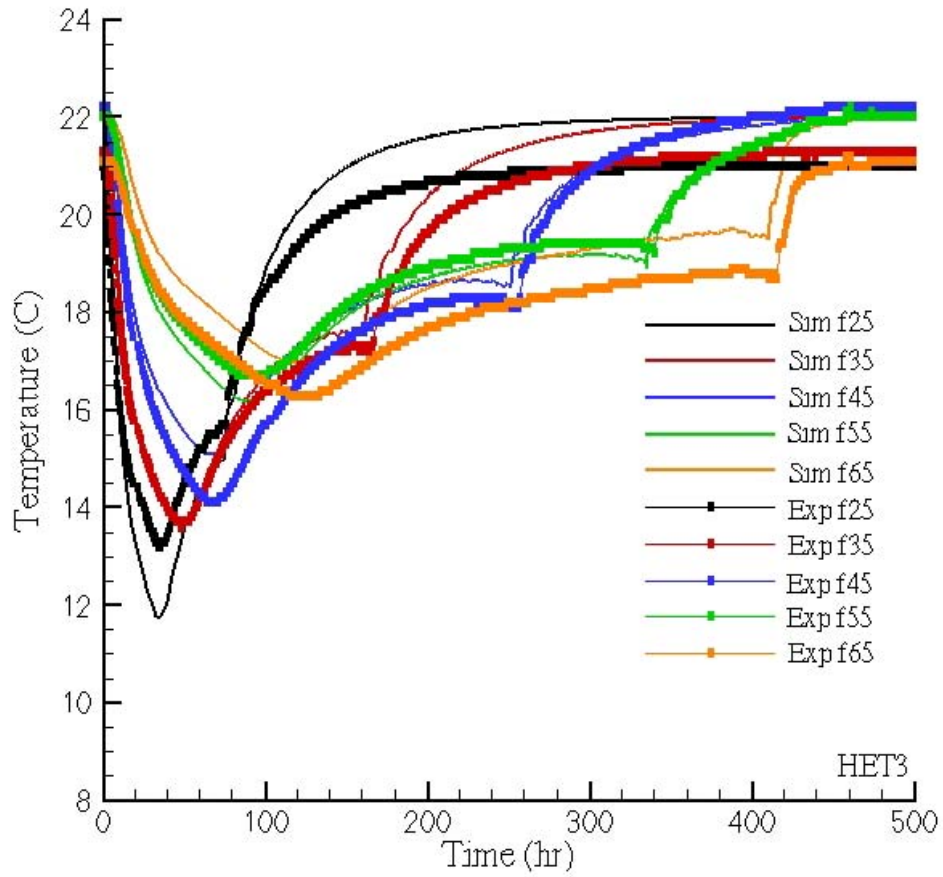
Figure 3.18. Observed (symbols) and Simulated Temperature (solid lines) at the Locations in the Fine-Grained Sand for Experiment HET3
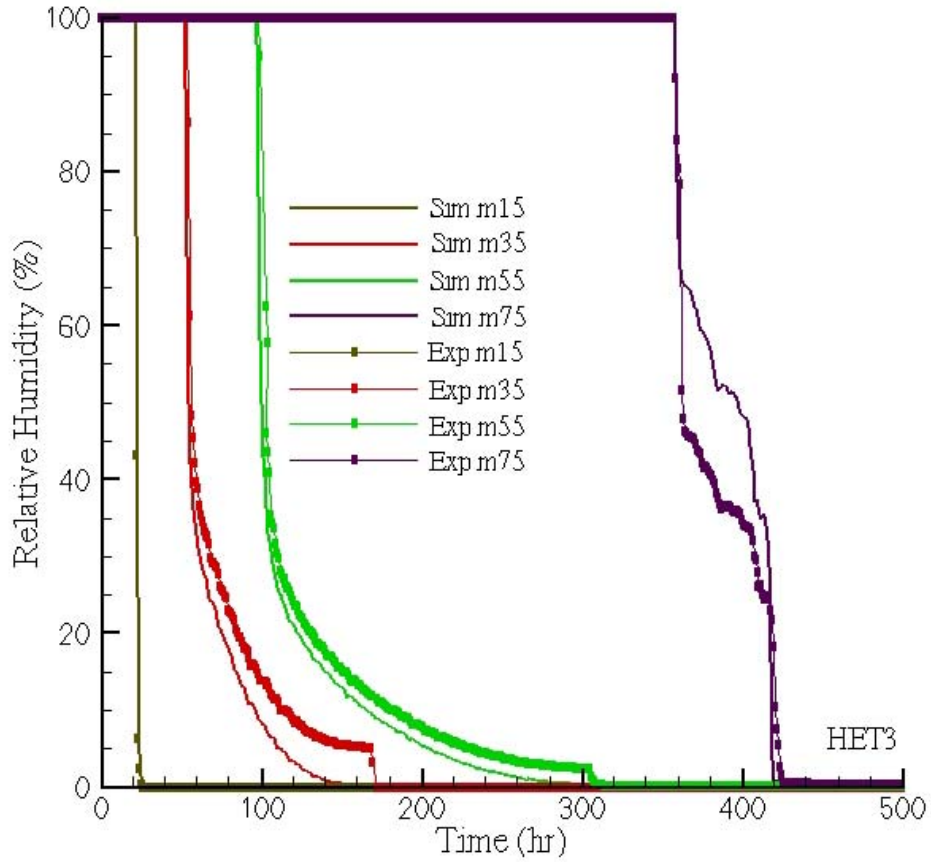
Figure 3.19. Observed (symbols) and Simulated Relative Humidity (solid lines) at Locations m15, m35, m55, and m75 for Experiment HET3
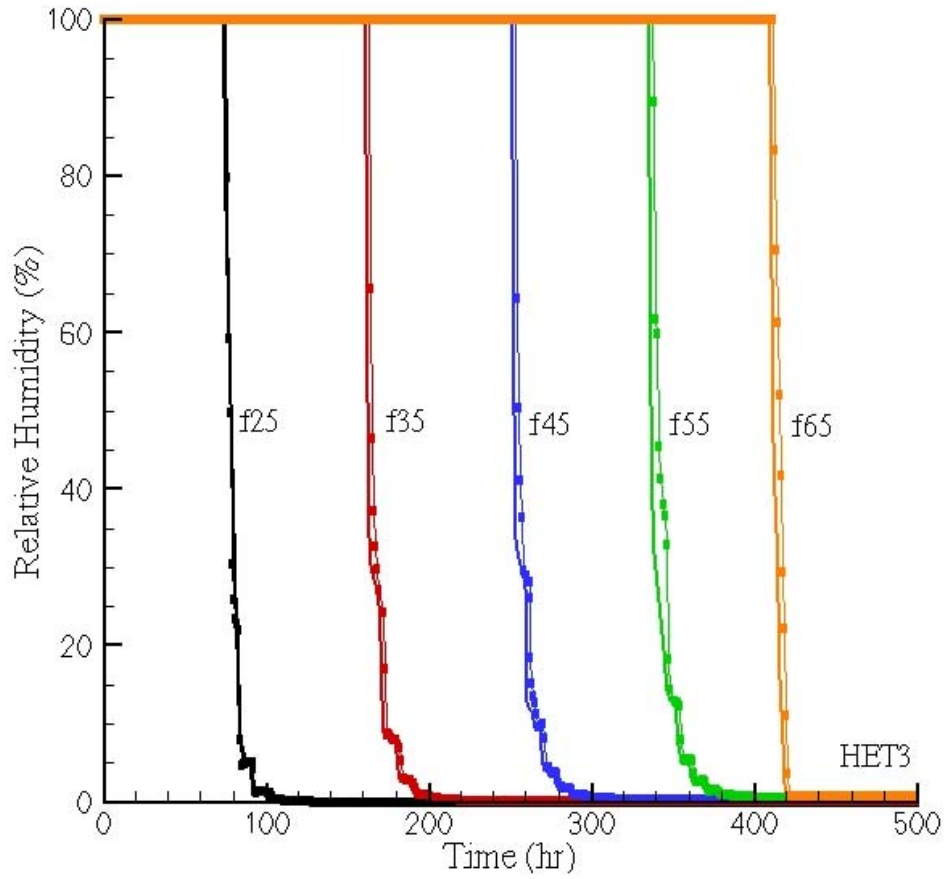
Figure 3.20. Observed (symbols) and Simulated Relative Humidity (solid lines) at the Locations in the Fine-Grained Sand for Experiment HET3
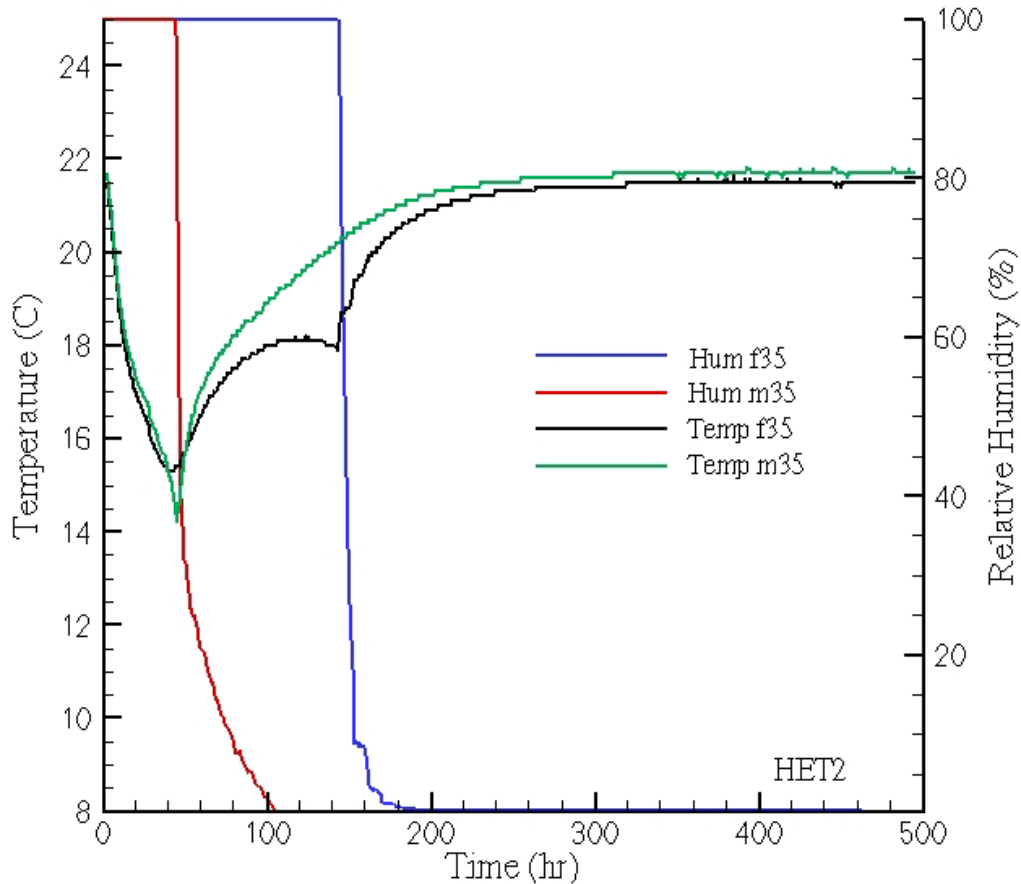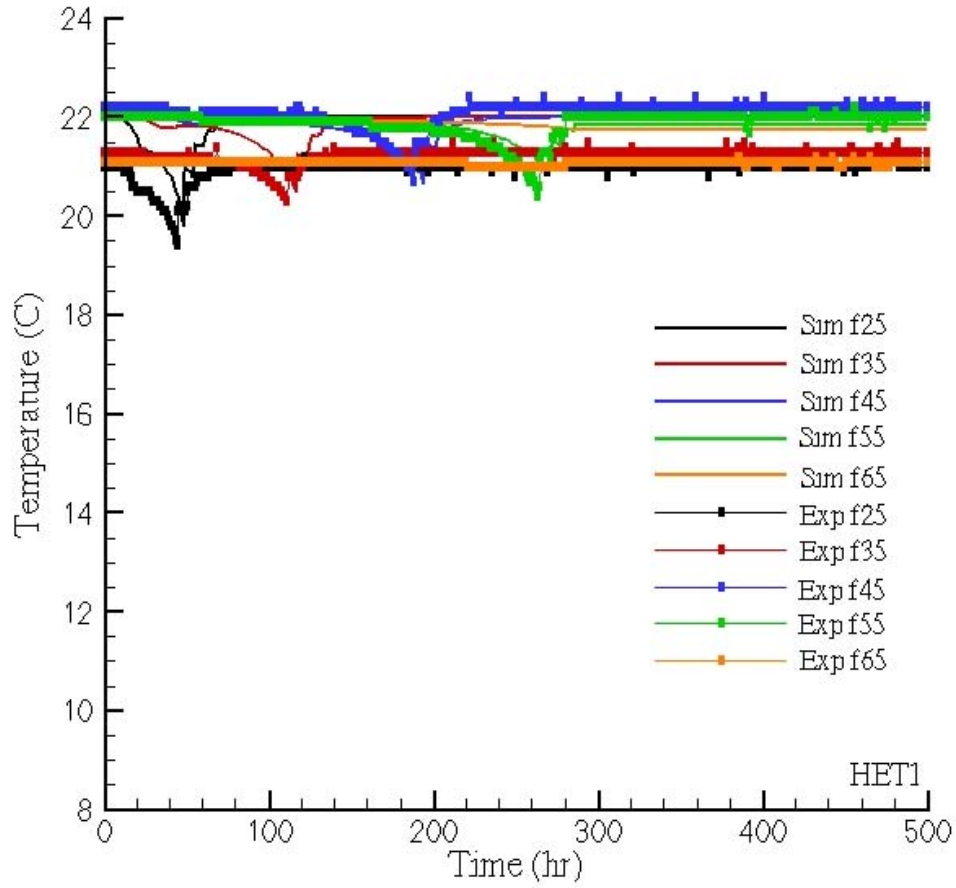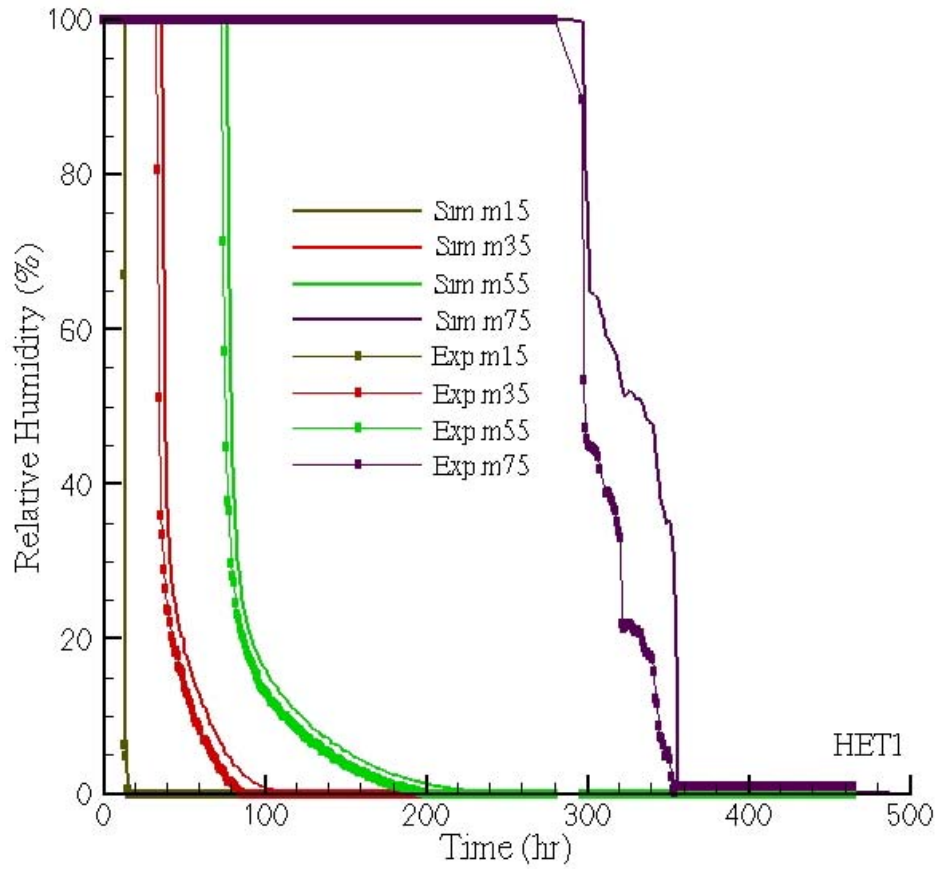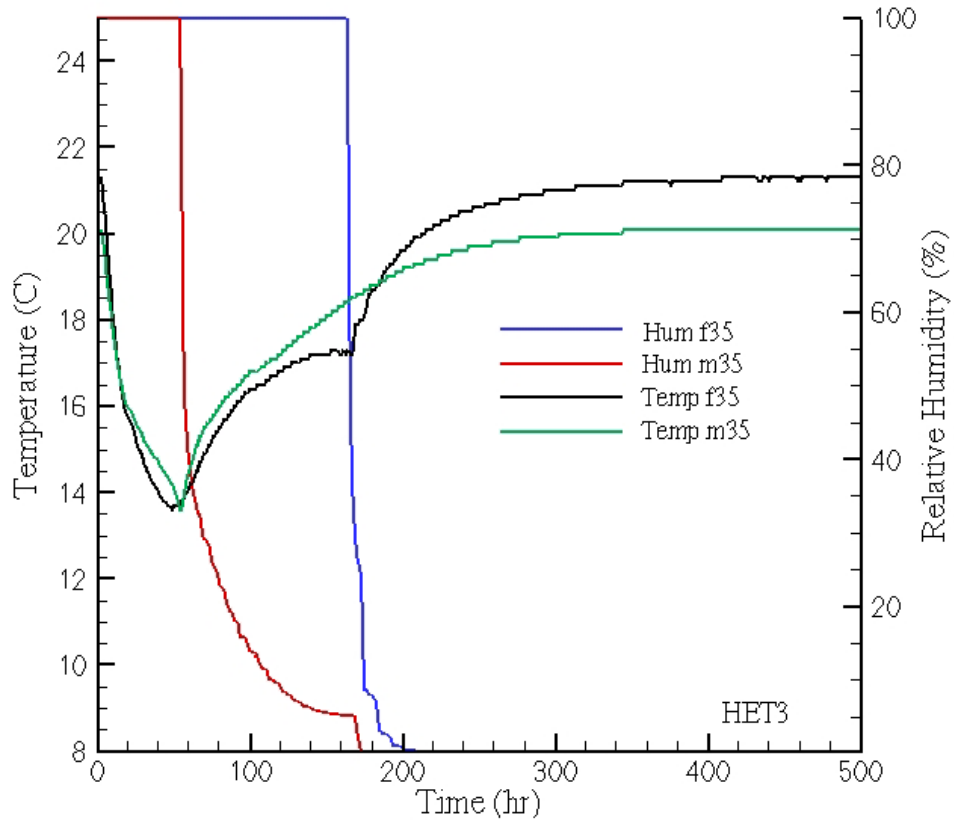
Figure 3.21. Observed Temperature and Relative Humidity Behavior at Locations m35 and f35 for Experiment HET3
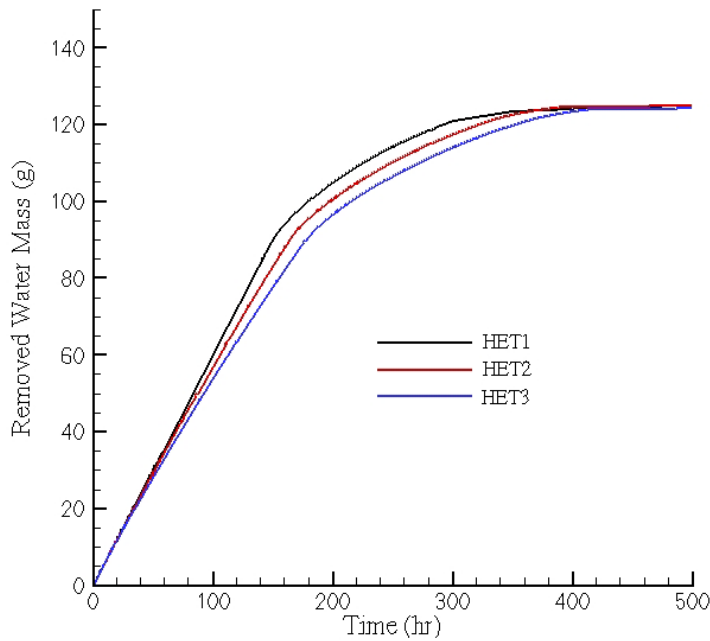
Figure 3.22. Cumulative Simulated Removed Water Mass for Experiments HET1, HET2, and HET3

3.23

4.0   Factors Controlling Soil Desiccation

Soil desiccation has the potential to remove moisture by evaporation and decrease the permeability, thereby reducing the potential for contaminant mobilization. Owing to the reduction in water content and the increase in gas-phase permeability, desiccation can improve access for other treatments that would be difficult to implement under normal conditions (e.g., gas-phase manipulations). For desiccation to be effective, there must be favorable contact between the injected air and wet/contaminated zones as the removal of water from contaminant source zones is limited by the amount of air contact. A clear understanding of the migration of injected air is therefore essential to aid in the design process, to minimize cost, and to maximize the chances of the desiccation system achieving its objectives. Although there are no published studies of the factors affecting soil desiccation, some insight can be gained from studies of soil venting in which desiccation is an undesirable side effect. Based on these studies, the effectiveness of soil desiccation will depend on the ability to achieve and maintain a sufficient flow of air and energy to support the dominant processes. These processes will be governed mainly by the air permeability of the soil, which determines the relationship between applied pressure, or vacuum, gas flow rate, and the evaporation rate. The effectiveness of soil-desiccation techniques will therefore depend on soil texture, soil temperature, air temperature, air pressure, and soil moisture content through its effect on phase partitioning and diffusion, but more importantly, on air permeability.

Mathematical models can be used to improve our understanding and ability to predict air migration patterns in a range of geological formations under a range of initial and boundary conditions. In light of this capability, the expert panel identified the development, testing, and verification of a multiphase numerical simulator for field-scale modeling as a prerequisite to field evaluation of desiccation. Simulating the desiccation process requires consideration of the multidimensional flow of water in the aqueous and vapor phases, as well as the flow of heat. All of these processes are influenced by subsurface heterogeneities. Therefore, to understand the interplay between efficiency, subsurface heterogeneities, and contaminant plume size, large-scale simulations using parallel computing schemes are needed.

Section 3 described modifications to the water-air-energy operational mode of the STOMP simulator to support large-scale desiccation simulations while considering meteorological and other surface boundary conditions that affect the energy balance. This section uses the upgraded water-air-energy operational mode of STOMP to investigate the factors controlling the desiccation process and gain insight into the key parameters needed to optimize the design and operation, including monitoring, of the field-scale desiccation test.

4.1 Materials and Methods

4.1.1 Simulations

To investigate the effect of low-permeability surface seals, soil temperature, injected air temperature, humidity of injected air, and injection pressures, simulations assumed a homogeneous isotropic sand formation with properties derived from the literature. Parametric simulations were performed to determine the effect of these properties on the air-flow pattern and energy balance of the desiccation system. To investigate the effect of soil texture on the air-flow pattern and effective extraction radius,

simulations were conduced using 5 of the12 soil textures identified in the U.S. Department of Agriculture (USDA) textural classification scheme. The parameters needed to describe the hydraulic properties with the Brooks-Corey (1964) model are summarized in Table 4.1 (Rawls et al. 1992). The first five textures were used in the simulations to investigate texture effects. These properties were chosen because they provide the means for studying system performance over a range of textures expected in natural soils. Hanford-specific databases are not sorted according to sedimentary lithofacies and contain limited data for the fine-textured facies that are typically present as thin interbeds.

Table 4.1. Hydraulic Properties of the Soil Textures

USDA Texture Class	Porosity ϕ_s $(cm^3\ cm^{-3})$	Saturated Hydraulic Conductivity K_s $(cm\ hr^{-1})$	Bubbling Pressure ψ_b (cm)	Pore-Size Distribution λ	Residual Saturation S_r
Sand	0.437	21	15.98	0.69	0.046
Loamy Sand	0.437	6.11	20.58	0.55	0.080
Sandy Loam	0.453	2.59	30.2	0.38	0.091
Loam	0.463	1.32	40.12	0.25	0.058
Silt Loam	0.501	0.68	50.87	0.23	0.030
Sandy Clay Loam	0.398	0.43	59.41	0.32	0.171
Clay Loam	0.464	0.23	56.43	0.24	0.162
Silty Clay Loam	0.471	0.15	70.33	0.18	0.085
Sandy Clay	0.430	0.12	79.48	0.22	0.253
Silty Clay	0.479	0.09	76.54	0.15	0.117
Clay	0.475	0.06	85.6	0.17	0.189

Soil thermal properties also play a critical role in the water and energy balance. These properties were estimated using pedotransfer functions that take into account the mineralogy and water-retention relationships of the porous materials (Ward 2007). Some properties were also derived from literature values measured on Hanford sediments (Cass et al. 1984; Shannon and Wilson 1994). In the simulations, the *Cass* STOMP option was used to describe thermal properties. The *Cass* option was chosen because it allows the additional specification of non-isothermal enhancement factors for vapor flow, which become important as the moisture content approaches the irreducible or residual content. The *Cass* option uses the model of Cass et al. (1984) to describe the thermal conductivity as a function of water content.

All of the simulations were conducted in two-dimensional homogeneous formations composed of the textures described in Table 4.1. One set of simulations was conducted in a heterogeneous formation composed of alternating layers of sand and silt loam, intended to mimic the lithology at the BC Cribs and Trenches Site (Ward et al. 2004). All of the simulations were conducted with a 25- × 25-m spatial domain discretized with a variable grid spacing ranging from 0.30-m to 1-m grid cells. For the base case, the top boundary was specified as a zero-flux (no-flow) with respect to the aqueous and gaseous phases and a Dirichlet (constant-value) boundary with respect to temperature with a constant temperature of 25°C. The exception was in the investigation of the effects of a low-permeability surface seal in which case the zero-flux boundary condition for the gaseous phase was replaced with a constant-pressure condition that kept the gas pressure equal to atmospheric pressure. The seal was assumed to be a clay soil with the properties described in Table 4.1.

At the bottom boundary, a zero-flux (no-flow) condition was imposed for the aqueous and gaseous phases whereas a Dirichlet (constant-value) condition was imposed for the energy equation with the temperature fixed at 25°C. The injection and extraction wells were used to define the side boundaries as shown in Figure 2.1. Heated dehumidified air was injected into a well on the left boundary whereas air humidified by soil desiccation was extracted from an extraction well on the right boundary such that air flow was left to right. For the base case, the temperature of the injected air was maintained at 25°C whereas the relative humidity was fixed at 0%. In addition to the base case, a number of simulations were conducted to investigate the effects of 1) soil temperature, with temperatures of 5, 12, 22, and 40°C, 2) air temperature (0 to 70°C), and 3) relative humidity (0 to 100%), at injection pressures ranging from atmospheric pressure (101,325 Pa) to 40 kPa above atmospheric. Air was extracted at pressures ranging from 0.9 atmospheres to 40 kPa below atmospheric pressure. Table 4.2 gives a summary of the cases simulated and the associated initial and boundary conditions.

Table 4.2. Initial and Boundary Conditions Used in the Numerical Simulations

Case	Initial and Boundary Temp. (°C)	Air Temp. (°C)	Injection Well Pressure (Pa)	Extraction Well Pressure Pa	Relative Humidity (%)
Base (w/surface seal)	25	25	101325	91192.5	0.0
Soil Temperature	5,12[a], 22, 40	20,30,40,50,60,70	101325	91192.5	0.0
Air Humidity	25	10,20,30,40,50	101325	91192.5	0, 10, 50, 75, 100
Air Pressure	25	25	101325 Pa + (0 10, 20, 30,40) kPa	101325 Pa - (0 10, 20, 30,40) kPa	0.0
(a) Mean annual air temperature for Hanford.					

The effects of soil texture were investigated using selected textures from the USDA textural triangle with the base case initial and boundary conditions. For each soil texture, the initial saturation was specified at 20%, which resulted in moisture contents ranging from 0.08 m^3 m^{-3} for sand to about 0.12 m^3 m^{-3} for silt loam to as high as 0.15 m^3 m^{-3} for clay. STOMP-WAE was used to simulate the spatial distribution of water content, capillary pressure, temperature, water-gas mass fraction, and gas pressure. For all simulation cases, continuous air injection was assumed over a 1-yr period.

4.2   Results and Discussion

4.2.1   Low-Permeability Surface Seal

In soil applications of soil vapor extraction, surface seals are often employed to prevent surface-water infiltration that can reduce air flow rates, reduce the emission of contaminant vapor, and minimize vertical short-circuiting of air flow. Figure 4.1 shows the simulated temperature distribution for homogeneous sand without a low-permeability surface seal whereas Figure 4.2 shows the distribution for the same formation with a low-permeability surface seal. Without a surface seal, air flow is from the injection well toward the extraction well (left to right), as expected. However, there is a significant contribution to the air-flow pattern from air that is drawn in through the ground surface. As the extraction well is approached, the gas-phase velocity vectors show a strong downward component as air is pulled toward the extraction well. Such "short-circuiting" would be compounded in the presence of geological

structures, such as high-permeability zones, that could cause the injected/extracted air to follow these paths rather than disperse evenly throughout the target zone. This phenomenon also appears to give rise to a zone of predominantly vertical flow around the extraction well at elevations above the screened interval (e.g., elevations between 7 and 10 m near x=10 m in Figure 4.1). The size of this zone would depend on d, the depth to the top of the well screen and the distance between the injection and extraction wells. The presence of a surface seal eliminates imbibition of air from the atmosphere and increases the area exposed to the desiccating effects of the pre-treated air (Figure 4.2). This plot shows that a much larger area is exposed to the injected air when a surface seal is present as the air flow is primarily horizontal. The evaporative front, as evidenced from the distribution of temperatures, is also more symmetric and approaches much closer to the extraction well after the same amount of simulation time.

The effect on the rate and efficacy of the desiccation process is clearer in plots of soil temperature and water content over time, as shown in Figure 4.3 and Figure 4.4, respectively. Without a surface seal, the reduction in temperature that accompanies evaporation is significantly less than when a seal is present. After 87 days of treatment, the time step from which the preceding figures were developed, the soil temperature at a hypothetical monitoring point (x=6 m, Elev. =4) had dropped from 25°C to 10°C with a seal present but only to 14°C without a seal. Soil moisture content decreased from 0.13 m^3 m^{-3} to 0.09 m^3 m^{-3} with a seal and 0.10 m^3 m^{-3} without a seal. By the end of a 1-yr simulation with a continuous injection of air heated to 25°C, the soil temperature had equilibrated to 8.7^{o}C with a seal present but only to 11.6^{o}C without a seal. The efficacy of the desiccation process was also dramatically impacted with the soil-water content decreasing to 0.03 m^3 m^{-3} with a seal and 0.06 m^3 m^{-3} without a seal. These effects are primarily due to differences in the flux of latent heat through the system and its effect on evaporation. Atmospheric air, pulled into the soil when there is no seal, is at the ambient temperature and relative humidity with a lower latent heat content and higher vapor pressure than the heated dehumidified air injected in the subsurface. The localized cooling, in the absence of dehumidified air, would lower moisture removal rates. Surface seals therefore restrict vertical air flow from the ground surface, near the extraction well and insulates the soil surface to minimize thermal gradients. With a seal, wells can be then be spaced farther apart because air imbibition from the surface is minimized, forcing pretreated air to be drawn from a greater lateral distance through the treatment zone.

Depending on the characteristics of the site, different materials can be used to seal the surface. On relatively flat sites that are free of surface structures, flexible membrane liners (FMLs) are commonly used. FMLs are available in a variety of materials, with high-density polyethylene (HDPE) being the most common. These liners are relatively easy to install and remove as they can be rolled out over the surface and rolled up for removal at the end of the treatment. One potential drawback is that the life expectancy of FMLs is shortened considerably when exposed to sunlight. There are numerous other geotextiles and natural materials that could serve as seals. These include HDPE liners, clay or bentonite seals, concrete, or asphalt paving. Under arid conditions, like those at Hanford, care would have to taken to prevent cracking of clay liners. At sites where desiccation is intended to supplement engineered surface barrier technology, the surface barrier would form a surface seal. The depth of the contaminant, although not evaluated in these simulations, would also be an important factor. Desiccation targeted tens of meters below the surface is unlikely to be impacted by short circuiting through the surface, although short-circuiting along improper seals could be a potential concern.
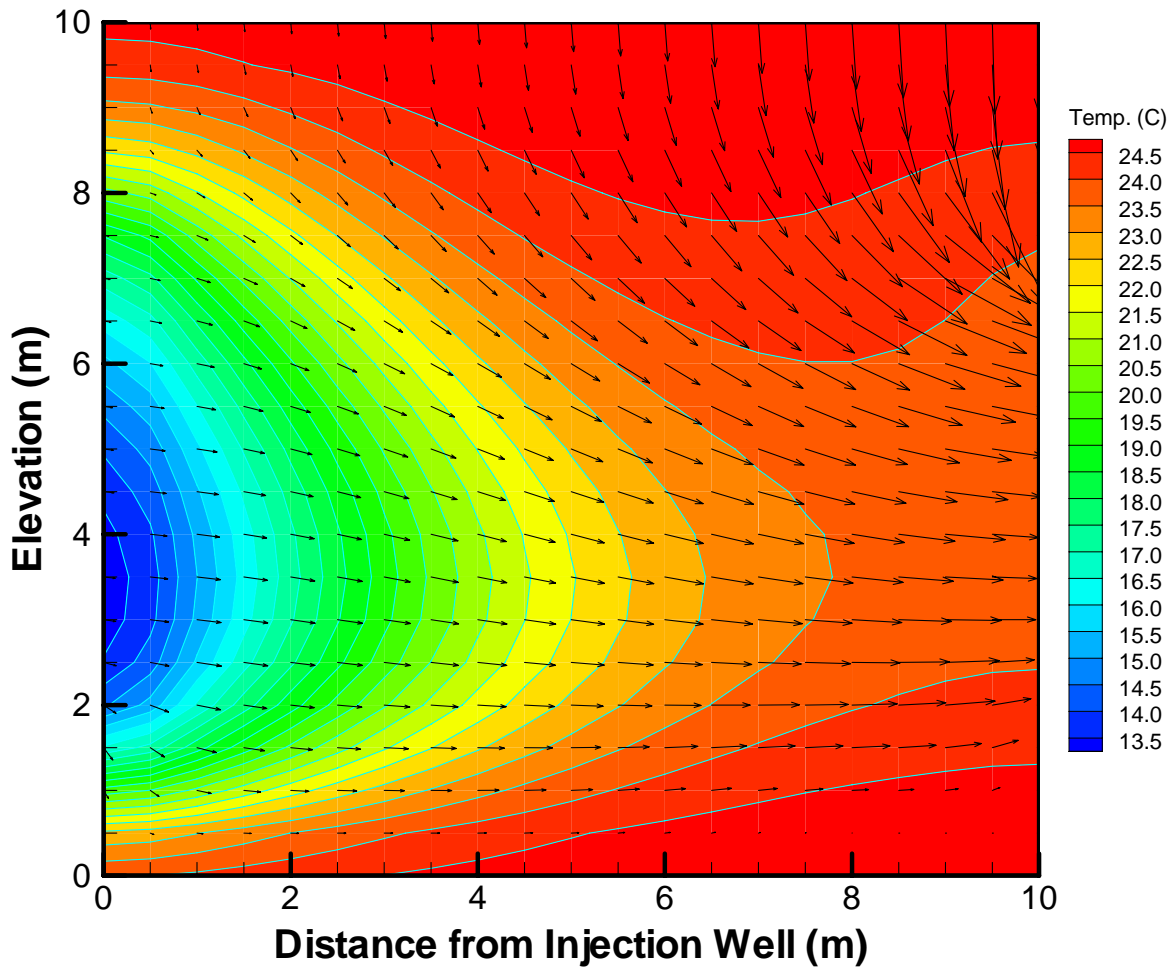
Figure 4.1. Predicted Soil Temperature Without a Low-Permeability Surface Seal After 87 days of Desiccation. Air at 25ºC and relative humidity (RH) 0% was injected at 1 Atm. into a sand at 25ºC and extracted at a pressure of 0.9 Atm. Black arrows are gas-velocity vectors.
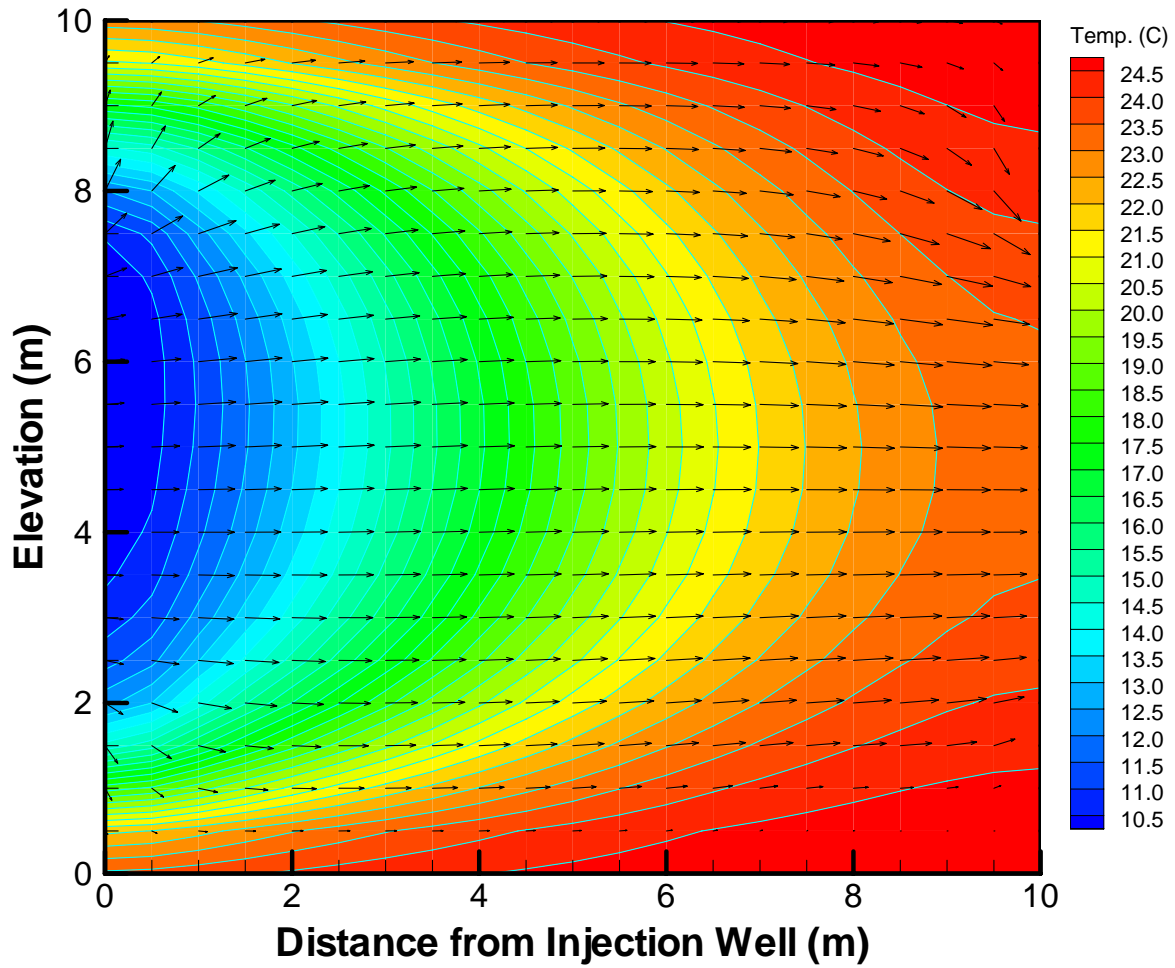
Figure 4.2. Predicted Soil Temperature with a Low-Permeability Surface Seal After 87 Days of Desiccation. Air at 25ºC and RH 0% was injected at 1 Atm. into a sand at 25ºC and extracted at a pressure of 0.9 Atm. Black arrows are gas-velocity vectors.
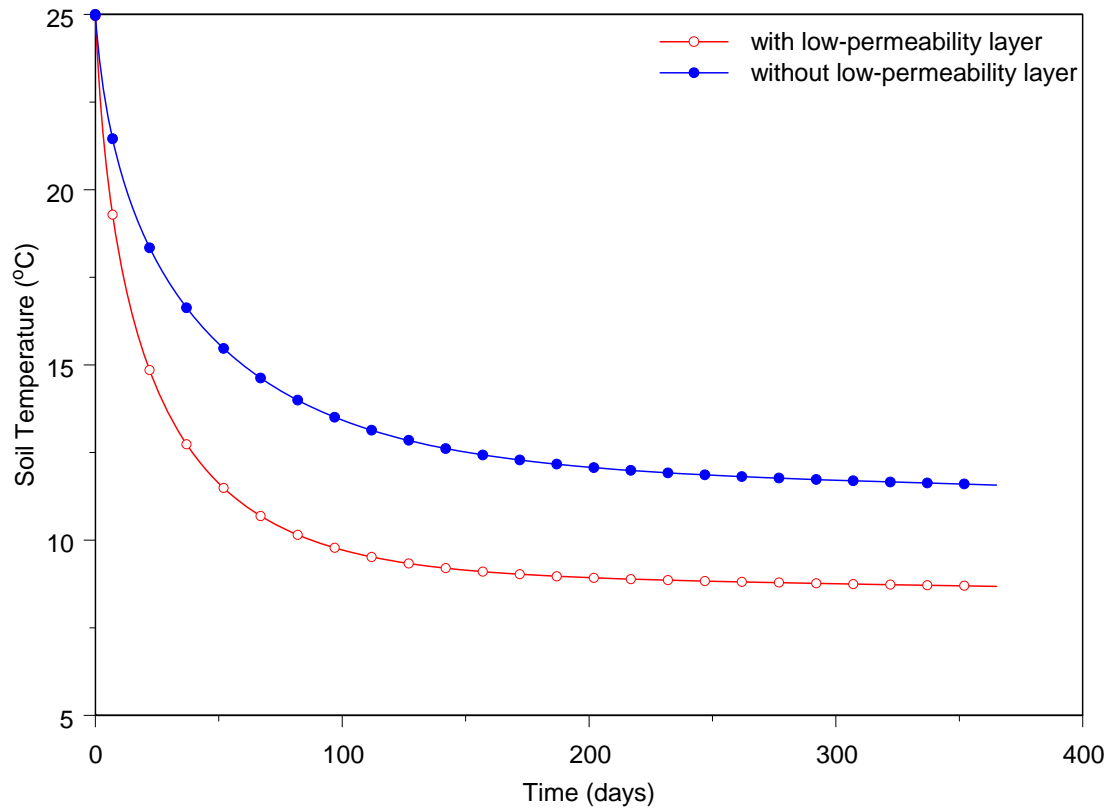
Figure 4.3. Predicted Soil Temperature Near The Injection Well with and Without a Low-Permeability Surface Seal. Air at 25ºC and RH 10% was injected at 1 Atm. into a sand at 25ºC and extracted at a pressure of 0.9 Atm.
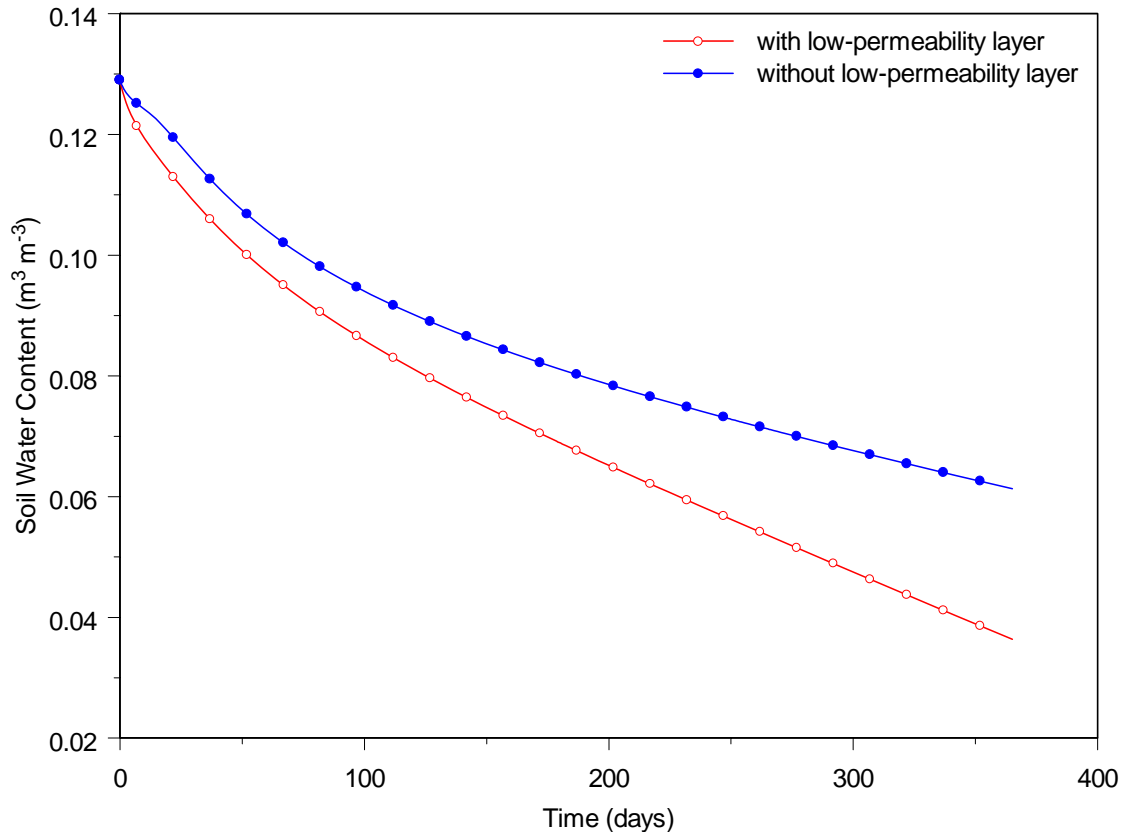
Figure 4.4. Predicted Soil Water Content Near the Injection Well with and Without a Low-Permeability Surface Seal. Air at 25ºC and RH 10% was injected at 1 Atm. into a sand at 25ºC and extracted at a pressure of 0.9 Atm.

4.2.2 Injected Air Pressure

Simulations to investigate the effects of injection pressure were also conducted in a homogenous sand formation. The initial condition for the soil assumed an aqueous saturation of 20% and a temperature of 25ºC. In the base case, dehumidified (RH=0%) heated air (25ºC) was injected continuously at a pressure of 101 kPa (1 Atm) whereas air was removed from the extraction well at a pressure of 91 kPa (0.9 Atm). Additional simulations were performed in which warm dehumidified air was injected at pressures of 10, 20, 30, and 40 kPa above atmospheric pressure. In each case, the extraction well was operated at 10, 20, 30, or 40 kPa less than atmospheric pressure.

All injection pressures showed a cooling effect, associated with passage of the evaporative front, which decreased with distance from the injection well. However, the degree of cooling and the passage of the drying front were strongly dependent on injection pressure. Figure 4.5 shows the temperature history at a hypothetical monitoring well located 10 m from the injection well. At the lower injection pressures, the rate of cooling was much slower than at the higher pressures, but the minimum temperature attained was lower. The injection at atmospheric pressure cooled the soil down to 11ºC compared to 11ºC at +10 kPa and 12ºC at +20 kPa. The minimum temperature observed at +30 kPa was 13ºC whereas +40 kPa resulted in a decrease to only 13ºC. The temperature minima coincide with the passage of the evaporative

front, and a rebound would be expected following the passage of this front for air injected at a temperature higher than the soil temperature. Figure 4.5 shows that at the lower pressures (+ 0 kPa, +10 kPa), the drying front had not passed the hypothetical monitoring well, even after 1-yr of injection. However, increasing the pressure by 20 kPa increased the rate of passage with the temperature minimum occurring at 180 days. A 30-kPa increase in injection pressure resulted in a decrease in the time of arrival of the desiccation front to 110 days whereas a 40-kPa increase in pressure reduced the arrival time to only 90 days. In accordance with the theory, these effects should translate into differences in the rate and total amounts of moisture removed.

Figure 4.6 shows the history of predicted moisture content and changes from the initial condition of 0.09 m^3 m^{-3}. After 1 yr, moisture content had decreased, by less than half, to 0.04 m^3 m^{-3} for injections at atmospheric pressure. A 10-kPa increase in injection pressure significantly increased the rate and efficacy of desiccation with water content declining to 0.01 m^3 m^{-3} after 1 yr of treatment. The +30-kPa and +40-kPa injections removed essentially all of the water from the system with water content declining to 0.0 m^3 m^{-3} after about 180 days and remaining unchanged for the duration of the simulation. These effects are primarily due to the lower air velocities at the lower injection pressures and the associated reduction in the rate of latent heat flux through the system. The simulations were all performed with a zero-flux surface boundary condition (i.e., no recharge), so persistence of the desiccation effects is currently unknown.

These results suggest that the choice of air compressor/blower for a particular site is important. A compressor/blower should be large enough to inject air at a sufficient pressure such that flow can be maintained at a reasonable rate to at least one well and ideally to multiple wells. Given the time required to desiccate homogenous sand, the compressor/blowers should be capable of long periods of operation. It is important to note, however, that the rate of flow though the soil is ultimately controlled by the air permeability. Fine textured soils can therefore be expected to require higher injection pressures. Although higher injection pressures will produce higher flow rates, they also increase the potential for bypassing low-permeability zones and can cause fracturing. Over pressuring could also affect the annular well seal creating a path for untreated air to enter directly from the atmosphere and the creation of stagnation zones that would reduce efficacy.

While these results provide insight into the importance of the injection pressure or volumetric injection rate, the rate at which air can be injected and/or extracted may be determined only after considering the site geology, constitutive properties (aqueous and air phase permeability-saturation relations), contaminant distribution, and end point for the desiccation treatment.

4.9
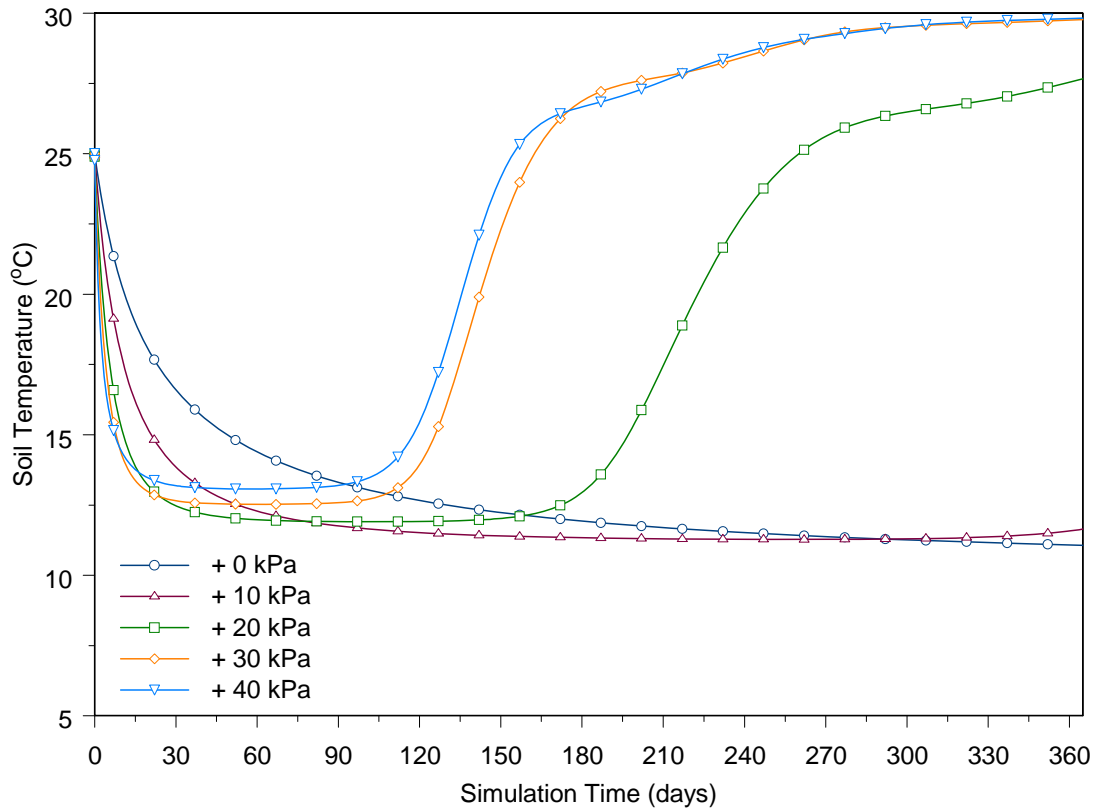
Figure 4.5. Predicted Temperature 10 m from the Injection Well Showing the Effect of Injected Air Pressure. Air at 30ºC and RH 0% was injected at atmospheric pressure (101 kPa) designated as + 0 kPa and as well as 10, 20, 30, and 40 kPa above atmospheric pressure.

Figure 4.6. Predicted Moisture Content 10 m from the Injection Well Showing the Effect of Injected Air Pressure. Air at 30ºC and RH 0% was injected at atmospheric pressure (101 kPa) designated as +0 kPa and as well as 10, 20, 30, and 40 kPa above atmospheric pressure.

4.2.3   Injected Air Temperature

As demonstrated experimentally and numerically in preceding sections, evaporation, powered by the latent heat from injected air, can lead to significant changes in soil temperature and moisture content in the subsurface. The ideal system is one in which the desiccation process is promoted with the minimum expenditure of energy for pretreating the injected air. The need for heating during pretreatment could dictate which times of the year are best for running a desiccation system. This section summarizes the results of numerical experiments performed to investigate the effects of injected air temperature on the rate and efficiency of desiccation. Simulations to investigate these effects were conducted in a homogenous sand formation. The initial aqueous saturation of the soil was fixed at 20%, and the temperature at 25ºC. Dehumidified air (RH = 0%) at temperatures ranging from 10ºC to 70ºC was injected at 141,325 Pa (40 kPa above atmospheric pressure) whereas the extraction well as maintained at a pressure of 40 kPa below atmospheric pressure (61,325 Pa).

Figure 4.7 shows a plot of soil temperature at a hypothetical monitoring well located 10-m from the injection well. The injection of air at temperatures between 10 and 40ºC caused a reduction in soil temperature. The soil temperature decreased from 25ºC to temperatures ranging from 3.2ºC, at an air temperature of 10ºC, to around 20ºC when air was injected at 40ºC. In contrast, injection of air heated to temperatures greater than the ambient soil temperature resulted in a two-step increase in soil temperature.

Temperatures increased to values ranging from 27°C at an air temperature of 50°C to 38°C when air at 70°C was injected. Following the initial increase, temperatures remained relatively steady until passage of the drying front, after which the soil continued to heat up to equilibrate with the temperature of the injected air. Both the time at which the minima in soil temperature occurs and the equilibrium temperature attained after passage of the desiccation front appear to be strongly dependent on air temperature. Given that the temperature minima and the first maxima in the case of air heated above the soil temperature are indicators of the passage of the desiccation front, the behavior of the moisture-content profile should provide further insight.

Figure 4.8 shows a plot of soil moisture content as a function of simulation time and injected air temperature. Regardless of the temperature, dehumidified air was able to remove essentially all of the soil moisture. However, the rate at which desiccation occurred was strongly controlled by the injected air temperature. The injection of cold, dehumidified air into a warm soil resulted in the slowest rate of desiccation. Air injected at temperatures less than the ambient soil temperature required from 50 days (20°C) to 75 days (10°C) for the moisture content to decrease by 50%. Injection at temperatures above the ambient soil temperature required between 21 days (70°C) and 32 days (30°C). The time for completely removing all of the soil moisture showed a similar dependence, ranging from 262 days at 10°C to as little as at 80 days at 70°C. Both the time at which the minima in soil temperature occurred and the equilibrium temperature attained after passage of the desiccation front appear to be strongly dependent on air temperature. As the temperature of the injected air increases, soil warming occurs faster, requiring less air. The strong dependence of performance on input air temperature is due to the nonlinear relationship between the saturation vapor pressure for water and temperature. Warm air holds more water vapor and therefore more thermal energy than cold air.

Based on these simulations, heating air above the ambient temperature will significantly increase the efficiency of a desiccation system. Even a 5-degree increase above the ambient temperature had a significant effect on system performance. Heating air to 70°C was the most efficient in terms of desiccation rate and final moisture content. However, estimating the system efficiency will require a cost-benefit analysis of the incremental increase in efficiency with increasing temperature, which is beyond the scope of this work. Nonetheless, the relationship between soil temperature and cleanup efficiencies observed in soil venting and bioventing applications has led to the development of a variety of methods to increase temperature (Walton and Anker 1996). Approaches range from simple diurnal variations in atmospheric temperature to the use of industrial waste heat. Solar heating is an approach that could have potential applications for the Hanford Site (Walton and Anker 1996; Chakraverty and Das 1992).
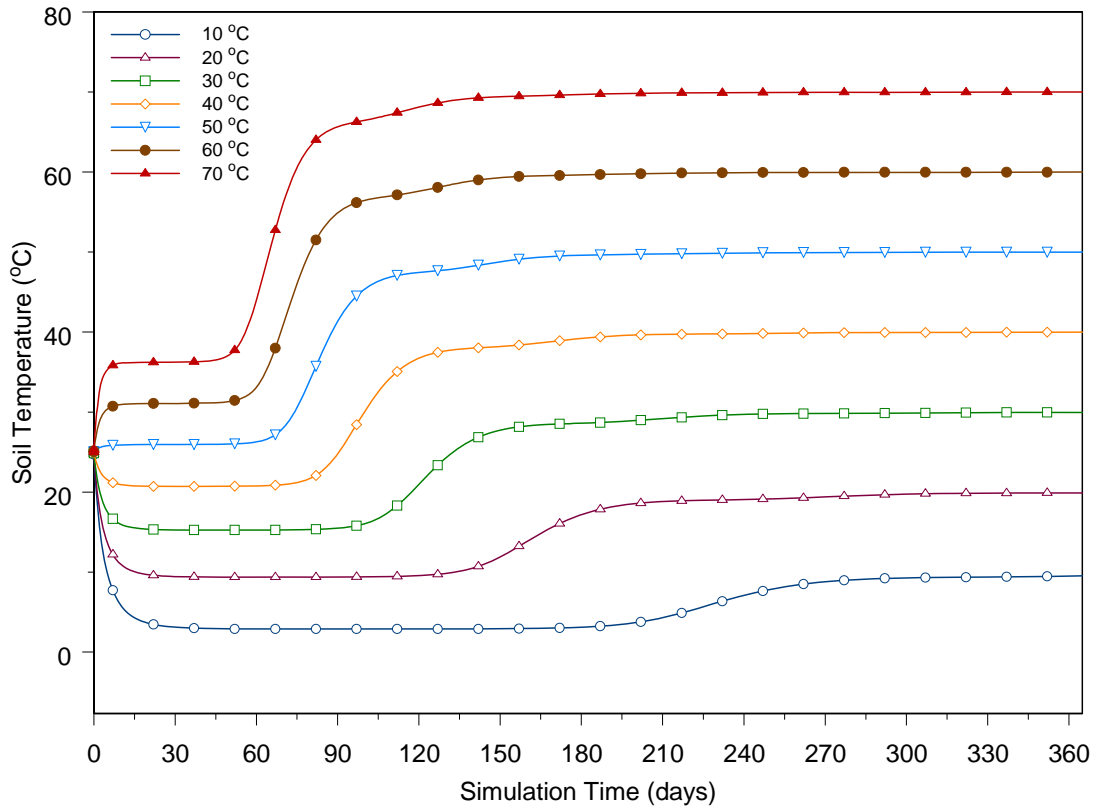
Figure 4.7. Predicted Soil Temperature 10 m from the Injection Well Showing the Effect of Injected Air Temperature. Air heated to various temperatures and dehumidified to RH 0% was injected at 40 Kpa above atmospheric pressure.

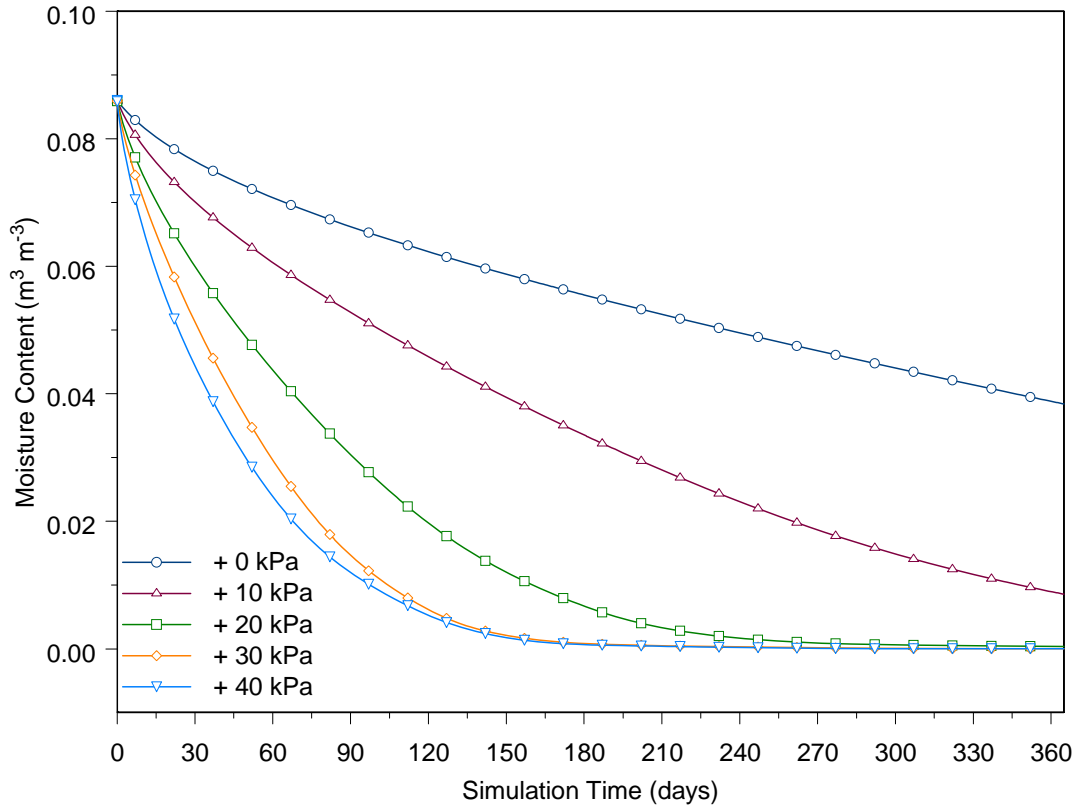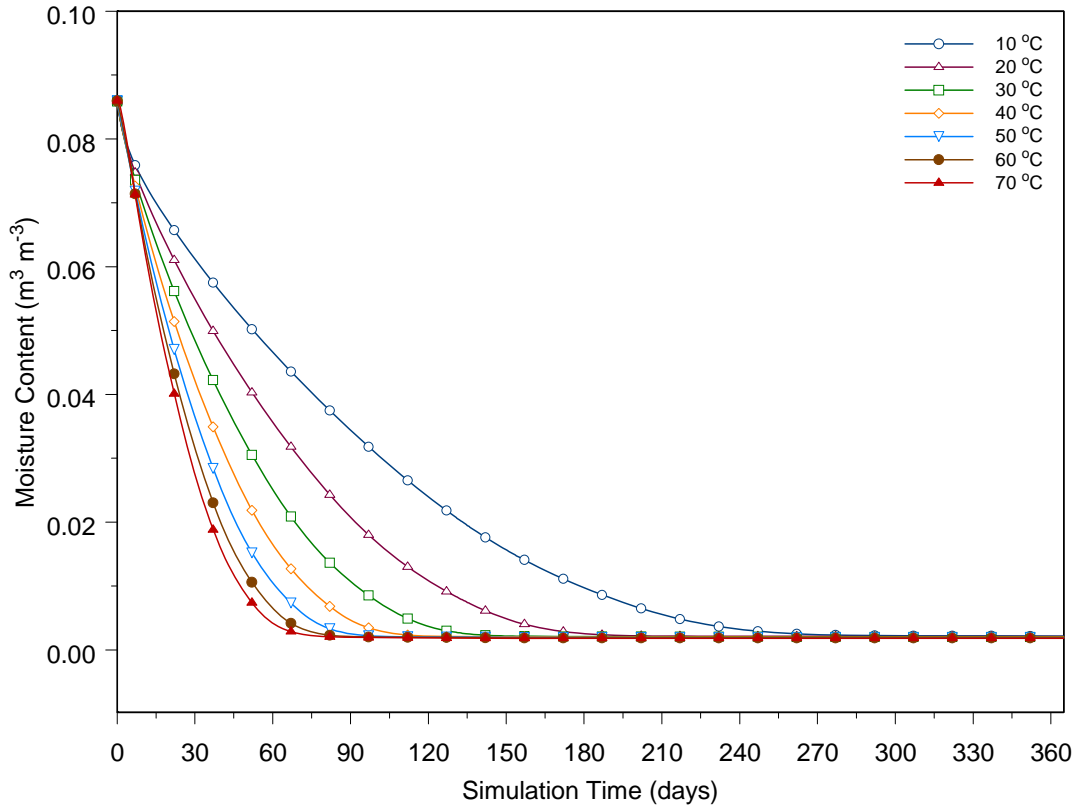**Figure 4.8.** Predicted Moisture Content 10 m from the Injection Well Showing the Effect of Injected Air Temperature. Air heated to various temperatures and dehumidified to RH 0% was injected at 40 kPa above atmospheric pressure.

4.2.4 Injected Air Humidity

Studies of soil vapor extraction have shown that the injection of dry air (<100% RH) can increase vapor-phase retardation of organics, primarily through a decrease in the soil moisture content in response to evaporation. Evaporation also causes a decrease in soil temperature, which can change sorption equilibrium and kinetic parameters. Although these sorption phenomena are not considered here, changes in soil moisture are important as they can give rise to capillary pressure gradients and changes in water flow. All of the simulations thus far used an arbitrary value of humidity. However, an improved understanding of the interplay between injected-air humidity and soil drying is important to predicting the efficiency of the desiccation process. This section summarizes the results of numerical simulations conducted to investigate the effects of injected-air humidity on the rate and efficiency of desiccation. Simulations to investigate these effects were conducted in a homogenous sand formation initially at an aqueous saturation of 20% and a temperature at 25°C. Air was assumed to be exposed to different pretreated regimes to establish relative humidity values of 0, 10, 50, 75, and 100% and temperatures ranging from 0 to 50°C. Heated, dehumidified air was injected at 141,325 Pa (40 kPa above atmospheric pressure) whereas the extraction well was maintained at a pressure of 40 kPa below atmospheric pressure (61,325 Pa). Only simulations for RH values of 0, 50, and 100% and an air temperature of 30°C are presented because these simulations demonstrate the primary impact of injected air humidity.

Figure 4.9 shows soil temperature as a function of time during the injection of air at 0%, 50%, and 100% relative humidity. The soil used in this simulation is a homogeneous sand initially with an aqueous saturation of 20% and a temperature of 25°C. These results show that air injected at 100% relative humidity is much more effective at heating the soil than dehumidified air. Within 8 days of starting the injection with humidified air, the soil temperature increased from 25°C to 29°C; by 21 days, the temperature had equilibrated with the air temperature. In contrast, dehumidified air caused a decrease in soil temperature, reaching 22.5°C within 21 days at 50% humidity and 13°C within a similar timeframe when dried to 0% relative humidity.
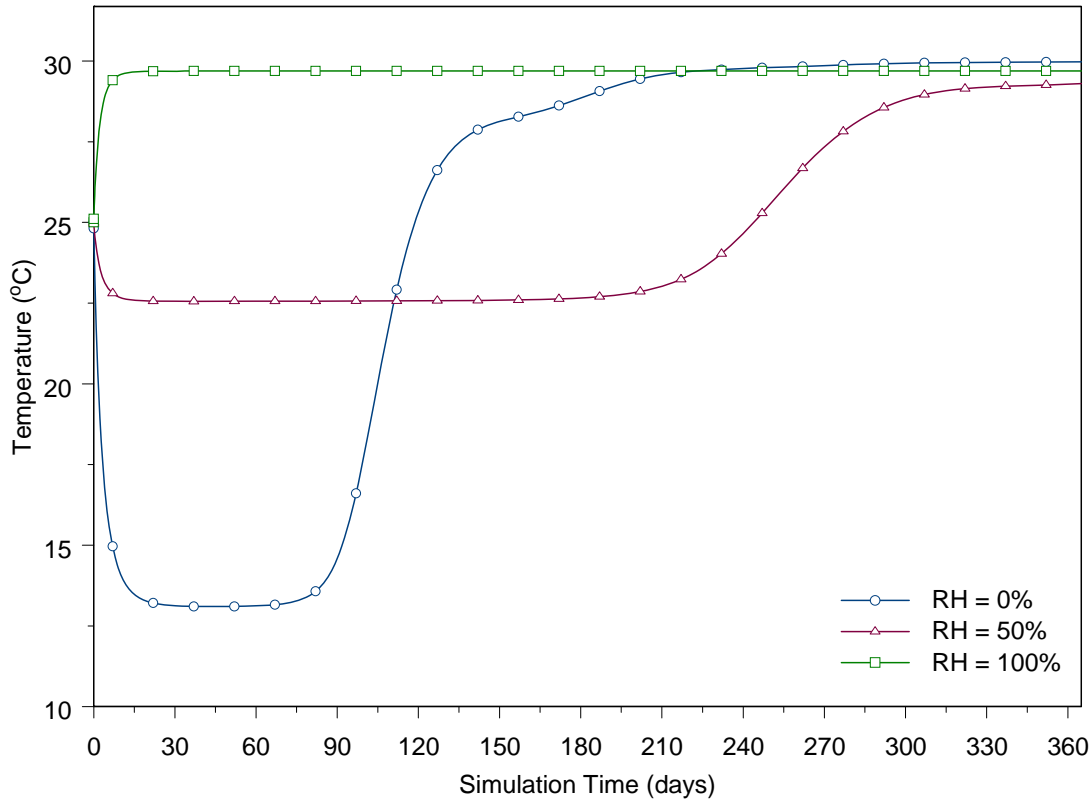
Figure 4.9.   Predicted Soil Temperature 10 m from the Injection Well Showing the Effect of Injected Air Humidity. Air at different values of relative humidity and heated to 30°C was injected at a pressure of 104 kPa into a homogenous sand at 25°C.

The soil warming observed during the injection of humidified air is due to the contribution of the latent heat of vaporization to the energy balance. This is because humidified air has a higher energy content than dehumidified air at the same temperature. Soil heating results from domination of the energy balance by the latent heat of vaporization. Even though dehumidified air is injected at a temperature higher than the soil temperature, the energy balance is negative, and soil cooling is observed. These results suggest that dry air (0% humidity), even when warmed, is not very effective at heating the soil. Our simulations suggest that the temperature of dry air must be above 60°C before the energy balance becomes positive and soil heating occurs. This phenomenon is also evident in Figure 4.7; dry air (RH=10%) must be heated to at least 50°C before soil heating occurs. Below 50°C, the energy balance is negative, and soil cooling occurs.

The effect of humidity on the desiccation process is readily apparent from a plot of moisture content (Figure 4.10). Injection of humidified air caused an increase in moisture content with increases as high as 0.02 m^3 m^{-3} observed for air heated to 70°C (not shown).
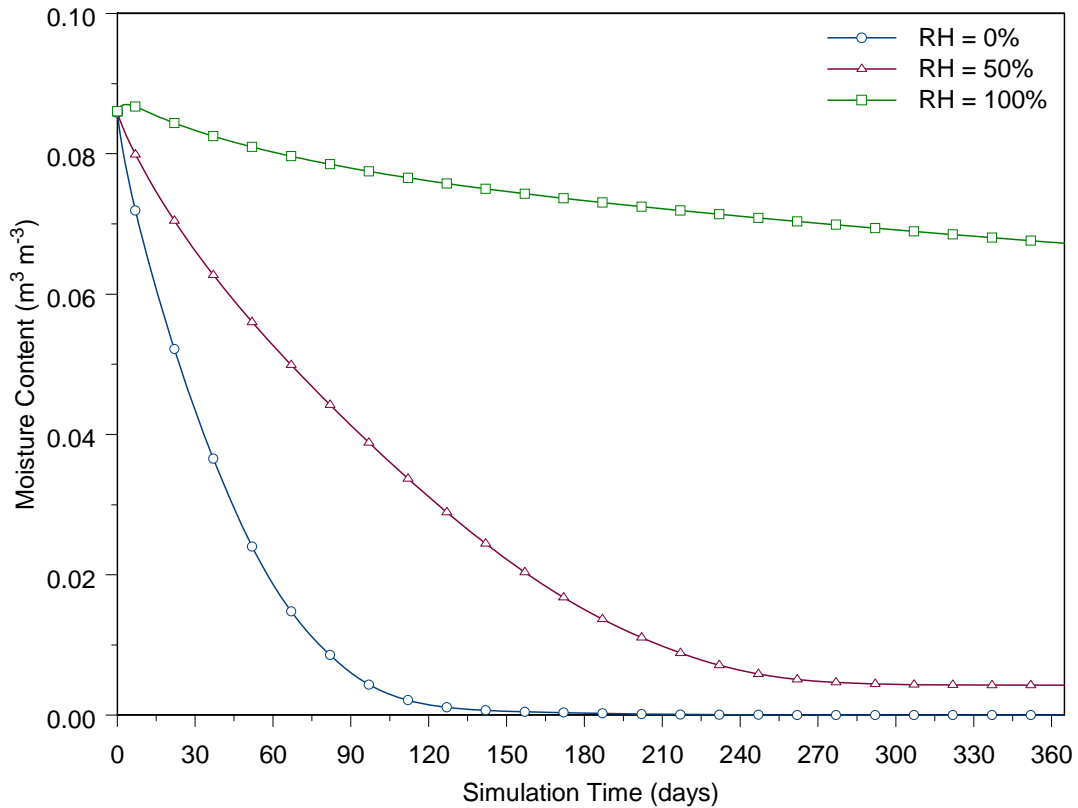
Figure 4.10. Predicted Moisture Content 10 m from the Injection Well Showing the Effect of Injected Air Humidity. Air at different values of relative humidity and heated to 30°C was injected at a pressure of 104 kPa into a homogenous sand at 25°C.

Owing to the high value of the latent heat of vaporization/condensation of water, the soil moisture content increases by only about 10^{-3} m^3 m^{-3} per ^{o}C increase in soil temperature due to condensation. This observation is consistent with that of Walton and Anker (1996). These results also suggest that the average moisture content does not decrease significantly with the injection of warm, humid air. After 1 yr of injection of warm humid air, the moisture content only decreased to 0.07 m^3 m^{-3}. Dehumidified air, at elevated temperatures, is quite effective at drying the soils. Injection of air at a relative humidity of 50% decreased the water content to 0.005 m^3 m^{-3} by day 277 whereas dry air (RH=0%) completely dried the soil by 126 days. These observations will have important implications for the operation of a desiccation system as diurnal and seasonal changes in atmospheric temperature and humidity will have to be factored in the pretreatment of air for injection.

4.2.5 Soil Texture

All geological systems are heterogeneous, and experimental studies on soil venting suggest that these techniques are most effective in relatively coarse-grained soils (Johnson et al. 1993). In most cases, air flow appears to occur in small continuous channels, and low sweep efficiencies can develop as a consequence of porous medium heterogeneities that channelize flow. To study the effects of soil texture on performance of the desiccation process, a series of simulations were performed in homogeneous sediments typical of those found at Hanford. These included the first five textural classes listed in Table 4.1, i.e., 1) sand, 2) loamy sand, 3) sandy loam, 4) loam, and 5) silt loam. In addition to these homogenous formations, simulations were also performed in a heterogeneous system composed of arbitrarily placed silt-loam inclusions in a sand matrix (Figure 4.11).
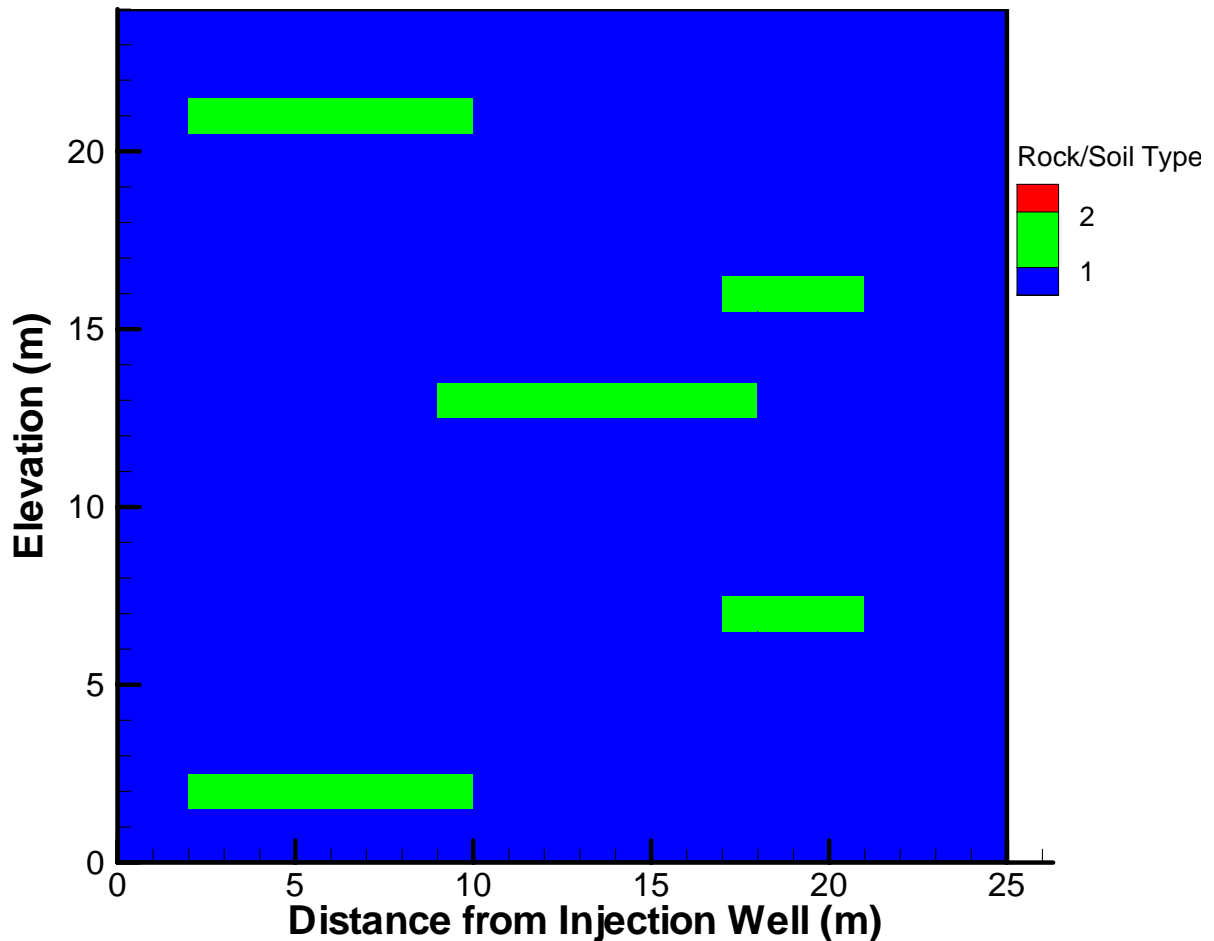
Figure 4.11. Domain Used to Study Impact of Heterogeneity. Fine-textured silt-loam inclusions (rock type 2) were arbitrarily imbedded in a homogeneous sand formation (rock type 1).

Figure 4.12 shows an example of the moisture distribution in a homogeneous sand after 87 days of desiccation. As expected, a parabolic-shaped distribution of the drying front results from the homogeneous formations with a minimum saturation near the screened section of the air-injection well. With a no-flow (perfect seal) upper boundary condition, there is also significant drying above the injection point. The dimensions of the parabolic shape can be used to estimate the radius of influence of the injection system and as the basis for identifying the spacing between injection and extraction wells. In the homogeneous sand, the zone of influence is in on the order of 20 m with the reduction in water content ranging from 40 to 50%. In general, simulations showed good air flow between the injection and extraction wells, even at separations of 20 m. In the finer textured homogeneous sediments, air distribution was constrained by the low air permeability, and well spacing had to be reduced, in some cases, to around $^1/_4$ that used in the sand simulations. Nonetheless, the radius of influence can be expected to increase with injection pressure and can only be truly determined from pilot tests at the site of interest.

Although there are no data with which to compare these results, they are qualitatively consistent with the observations of Thomson and Johnson (2000). They reported that air flow was confined to a zone with a 0.3- to 0.6-m radius in homogenous formations. Similar patterns were reported by Lundegard and LaBrecque (1998), who used an electrical resistance tomography system to map air distributions, and McKay and Acomb (1996), who mapped air distributions with neutron logs. In both cases, steady-state air distribution was centered on the injection point with the bulk of the flow occurring within a 0.3- to 1-m radius. In general, the air-flow pattern is quite symmetric with the flow vectors connecting the screened intervals of the injection and extraction wells. Predictions of gas-phase saturations and relative permeabilities reflect these patterns. Figure 4.12 also shows a large dry zone developing quite rapidly in the vicinity of the injection well. This zone, which at this time step is on the order of 5 m × 15 m, progressed though the system behind the evaporative front. The association between this zone of low moisture and the energy balance is more apparent in the temperature distribution.

Figure 4.13 shows a plot of temperature in response to the air injection. There is evidence of cooling in the vicinity of the injection well with soil temperature initially dropping to around 12°C as water evaporates from the pore space. As the drying front progressed, a rebound in temperature was evident between 0 and 2 m. This observation is consistent with the theory that predicts a negative energy balance (soil cooling) when dry air is injected, even at temperatures above the ambient soil temperature. Following the passage of the drying front, the energy contained in the air is then used to heat the soil to a temperature equal to the injected air temperature.

4.18

Figure 4.12. Predicted Moisture Content in a Homogenous Sand Formation After 87 Days of Desiccation. Air at a relative humidity of 0% and heated to 30ºC was injected at a pressure of 104 kPa initially at a temperature of 25ºC and an aqueous saturation of 20%. The black arrows are the gas-phase velocity vectors. The moisture content legend is in $m^3 \ m^{-3}$.
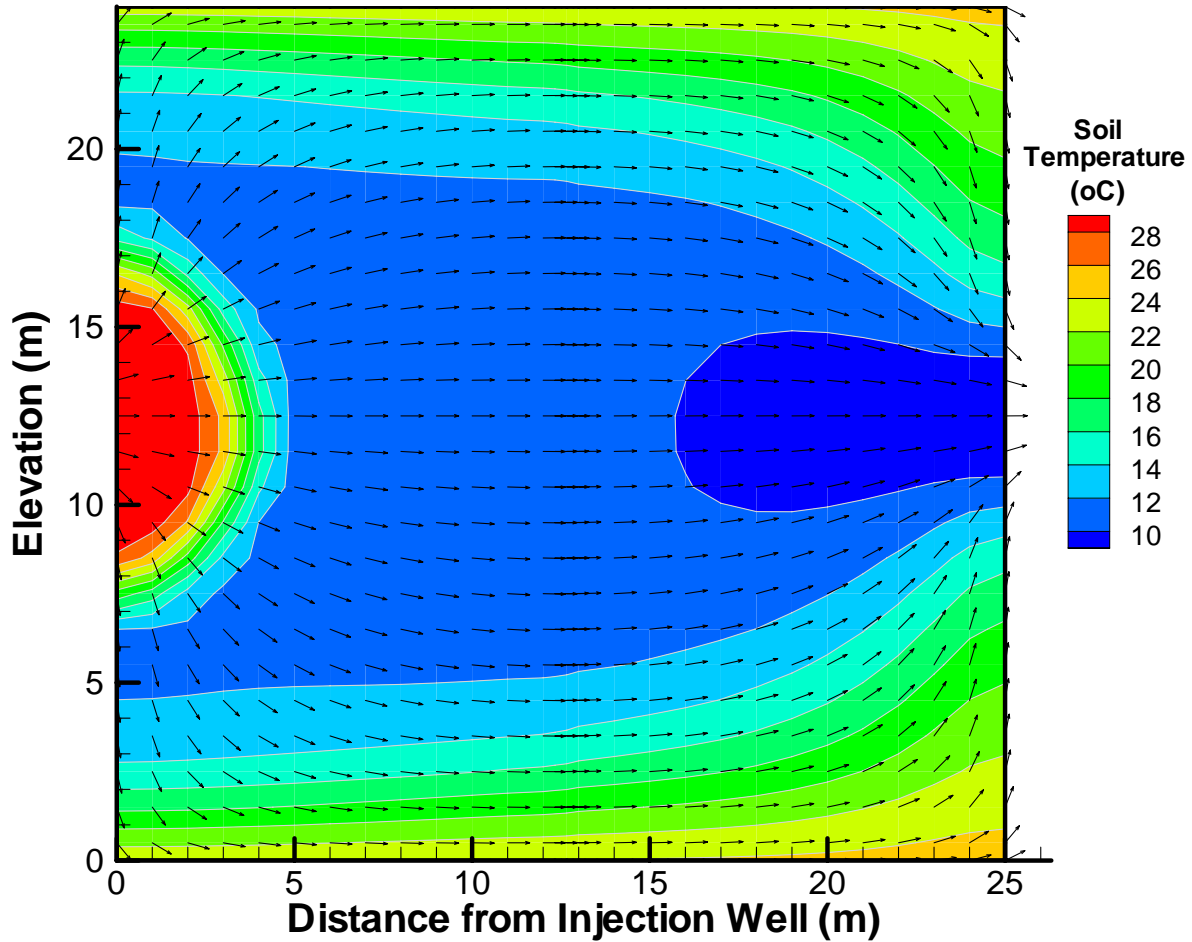
Figure 4.13. Predicted Temperature in a Homogenous Sand Formation After 87 Days of Desiccation. Air at a relative humidity of 0% and heated to 30°C was injected at a pressure of 104 kPa initially at a temperature of 25°C and an aqueous saturation of 20%. The black arrows are the gas-phase velocity vectors. The temperature legend is in °C.

Figure 4.14 shows a plot of soil temperature at a hypothetical monitoring well located 10-m from the injection well. Both the homogenous sand and sand with silt-loam interbeds show similar results, including the effects of evaporative cooling. High-permeability sand dominates the air flow field, which results in the similarity in behavior between the homogenous and heterogeneous sands. Nonetheless, the development of an evaporative front is strongly dependent on texture. Within 90 days, the evaporative front had developed, and the energy from the air had started to heat the soil in the sand simulations. The loamy sand, a texture that is also common at Hanford, showed a much-delayed response with the front passing after 240 days. This difference is due primarily to the difference in permeabilities (21 cm/hr for sand and 6.11 cm/hr for loamy sand). All other textures showed a very gradual decline in temperature, but none showed clearly defined minima.
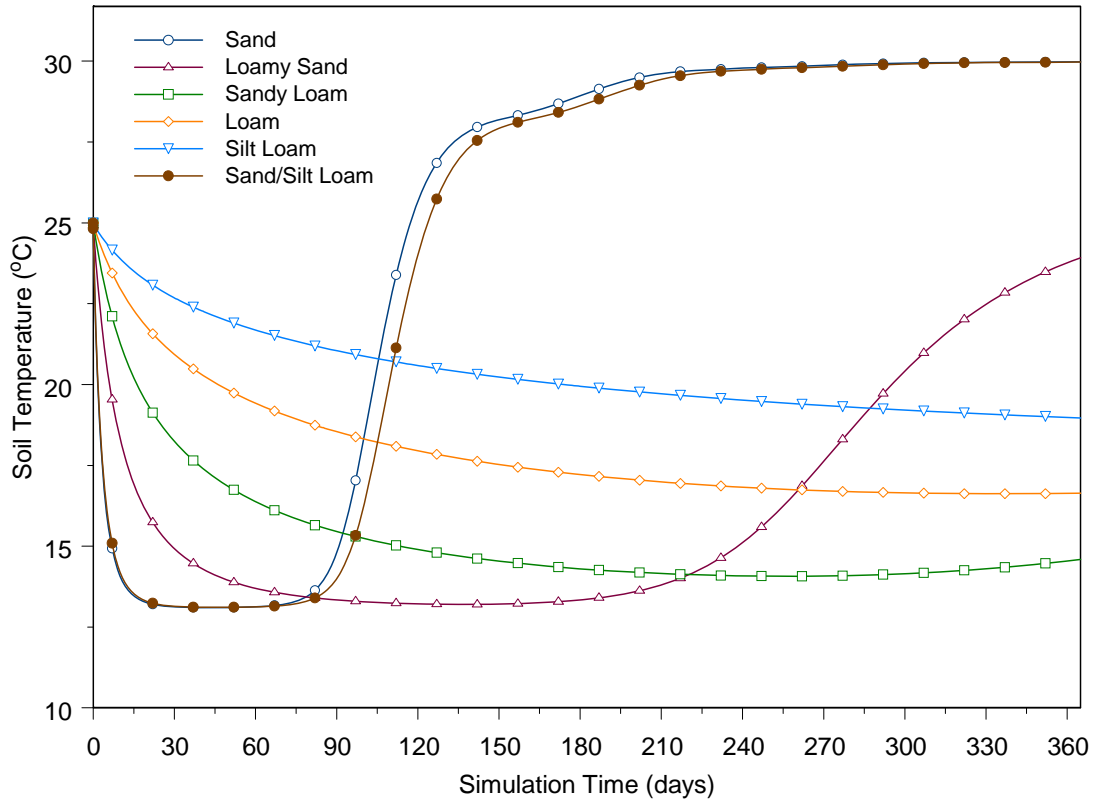
Figure 4.14. Predicted Moisture Content near the Injection Well Showing the Effect of Soil Texture. Air at a relative humidity of 0% and heated to 30°C was injected at a pressure of 104 kPa into different soil textures initially at a temperature of 25°C and an aqueous saturation of 20%.

Figure 4.15 shows a plot of soil moisture content as a function of simulation time for each texture. Regardless of the texture, all injections resulted in a decline in moisture. However, the rate of this decline and the moisture end point were both texture dependent. Owing to the larger permeability, the sand allowed the highest air-flow rates, and desiccation was fastest, reaching completion after 120 days. The loamy sand was considerably slower with moisture content approaching dryness towards the end of the 1-yr simulation. In the same period, the moisture content in the sandy loam had only declined to 0.03 m^3 m^{-3}, whereas the loam and silt loam had declined to 0.06 m^3 m^{-3} and 0.08 m^3 m^{-3}, respectively.

These results suggest that desiccation technology may have limited applications in homogeneous formations of fine-textured sediments. However, such deposits are rare at Hanford, and the more common formation is a coarse-textured host with fine-textured interbeds. In such systems, air flow can still occur but is confined to continuous channels of high-permeability sediments. Preferential movement of air in these formations would bypass the fine-textured, high-moisture lenses. Although the rate of desiccation would be quite slow for the fine-textured layers, the intervening coarse materials would be dried quite rapidly. The result is a creation of multiple local capillary breaks that would prevent the downward migration of water and contaminants. This phenomenon is illustrated in Figure 4.16, which is a plot of moisture distributions of the formation consisting of silt loam interbeds in a sand matrix. The
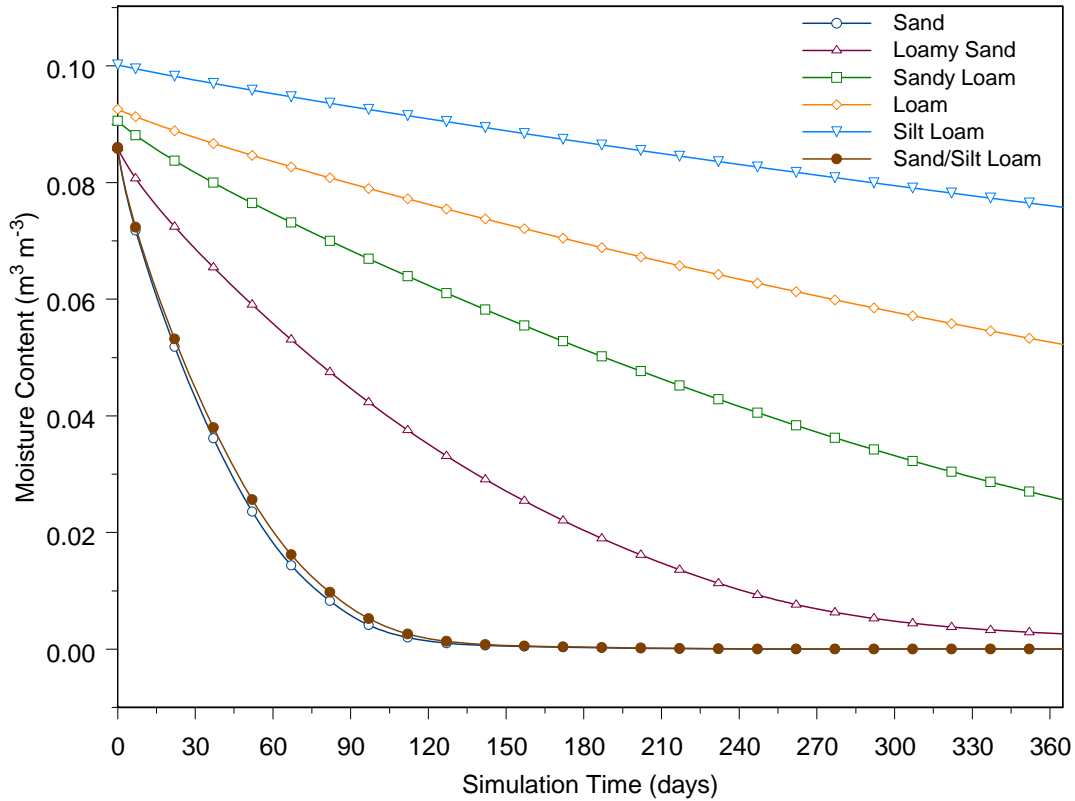
Figure 4.15. Predicted Moisture Content near the Injection Well Showing the Effect of Soil Texture. Air at a relative humidity of 0% and heated to 30°C was injected at a pressure of 104 kPa into different soil textures initially at a temperature of 25°C and an aqueous saturation of 20%.

development of the drying front is readily apparent around the injection well, encompassing a zone of around 5 m × 15 m. There is evidence of drying in the silt-loam lenses, but a more important observation is the development of low-moisture zones, mostly beneath these lenses.

Preferential air flow is consistent with the observations of Tomlinson et al. (2003), who noted the entrapment of air beneath fine-textured lenses with air movement being a combination of lateral spreading with a lesser amount of upward migration through the low-permeability lenses. In fact, Johnson et al. (1997), using SF_6 gas, were able to show that in a fine sand with interbedded clayey silts, air movement was predominantly lateral, and this lateral migration continued until a monitoring well was intersected. In this simulation, air movement was also mostly through the coarse layers, but it did not significantly impact the desiccation process. Initially, desiccation was confined to a small zone around the injection point, but as the coarser sediments dried out, air could come in contact with more surface area of the fine-textured sediments. As water moved toward the now drier surfaces in response to capillarity, this water was quickly evaporated by the injected air. These lenses are typically the location of high contaminant concentrations. The concept of a capillary break dictates that the movement of moisture out of these lenses into the underlying dry soils would require the fine-textured lenses to reach a capillary pressure equal to the bubbling pressure of the sand (-16 cm). Rewetting to this suction under natural recharge rates has a low probability that would be even lower if an engineered surface barrier is constructed over the

waste site to limit recharge. As shown in Figure 4.15, the soil moisture content decreased quite rapidly from a high of near 0.10 m^3m^{-3} to less than 0.05 m^3m^{-3} in less than 100 days. At the observation point located 1 m from the injection well, the steady-state water content was near zero in less than 1 year.
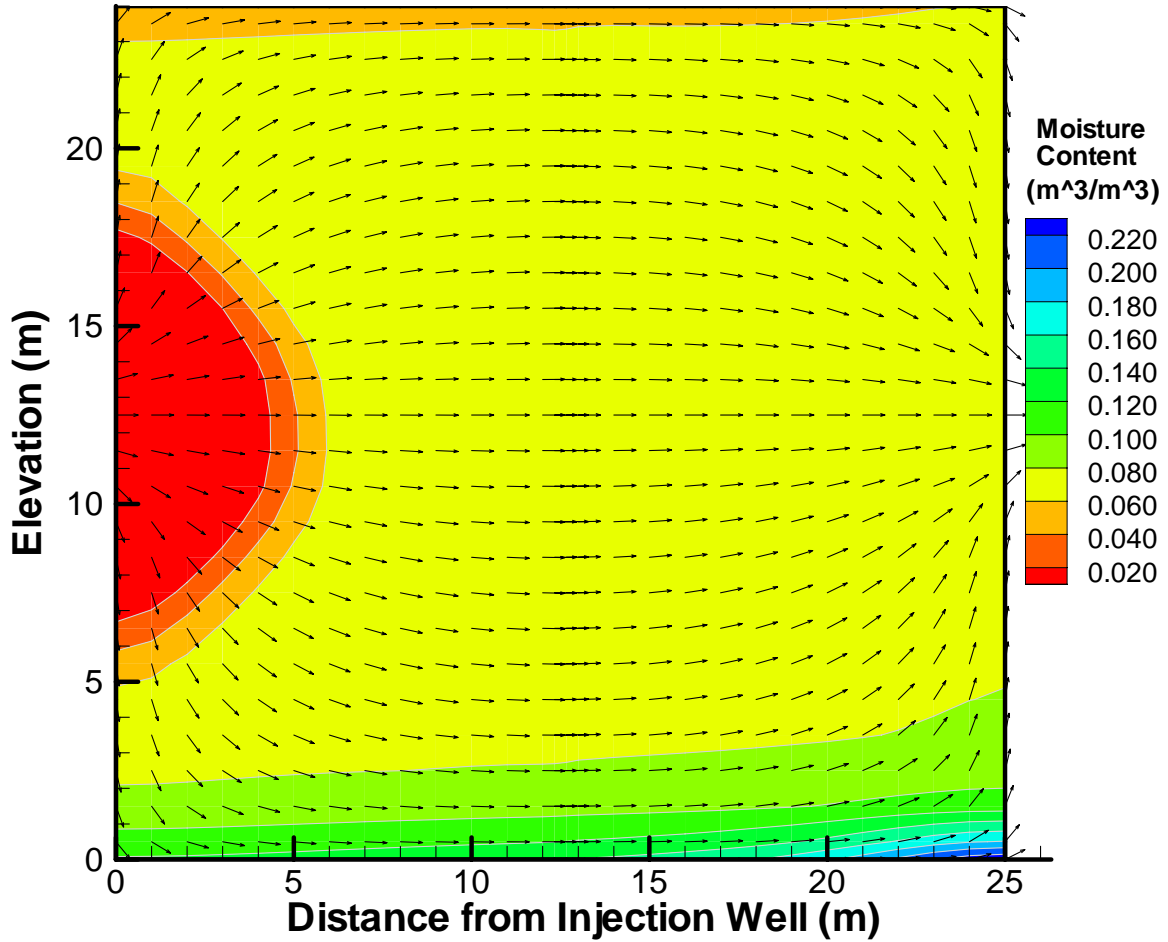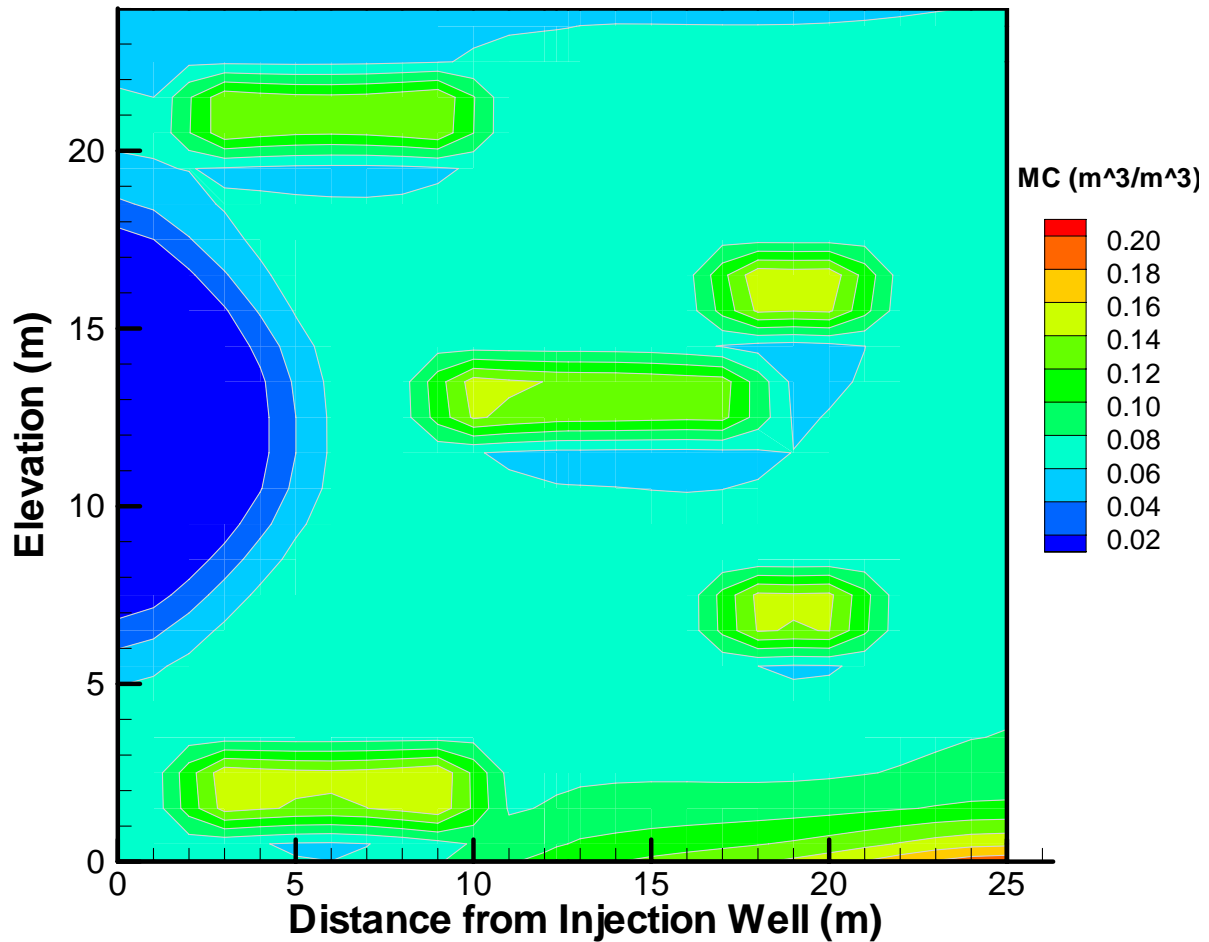

Figure 4.16. Predicted Moisture Content in Heterogeneous Formation After 87 Days of Desiccation. Air at a relative humidity of 0% and heated to 30°C was injected at a pressure of 104 kPa initially at a temperature of 25°C and an aqueous saturation of 20%.

4.2.6   Well Spacing

Well spacing, which is also an important parameter to be considered in the design of a soil desiccation system, is controlled by the radius of influence (ROI) of the injection/extraction wells. The ROI is often defined as the greatest distance from an injection/extraction well at which a sufficient pressure/vacuum and air flow can be induced to increase evaporation and ultimately remove water from the soil. Previous sections suggest that air-flow patterns are controlled by several factors, but for a given set of conditions, the injection pressure appears to have the greatest influence on desiccation rates and efficiency. Thus, to demonstrate the effects of well spacing, hypothetical monitoring wells were placed at 1-m intervals from the injection well in a homogenous sand formation, and the desiccation process was simulated. Predicted air pressure and moisture content were analyzed to determine the radius of influence.

Simulations suggest that the ROI increases significantly with the simultaneous operation of an injection and extraction well. Thus, all simulations were performed with an extraction well operating at 20 kPa (2.9 psi), the mean operational range of commercial vacuum pumps (Suthersan 1996). Injection pressures were also chosen to match the operation ranges of typical commercial air compressors and are shown in Table 4.3. The common value of 10% of the injection pressure is assumed here. Figure 4.17 shows a plot of the subsurface pressure as a function of distance from the injection well in a homogenous sand after 365 days of air injection. Air pressure shows a nonlinear decrease with distance from the injection well. The ROI is essentially the distance at which a sufficient level of pressure/vacuum is present to induce air flow. This "cut-off" pressure/vacuum level has been defined differently by a number of researchers, but is essentially an empirical value based on prior experience and geologic conditions (Suthersan 1996). Nonetheless, the simultaneous use of an injection and extraction well, operating at a typical level of vacuum, results in adequate air flow to the extent of the simulation domain of 25 m (82 ft). Based on reports from the vapor-extraction literature, a spacing of 25 to 30 m (80 to 100 ft) is considered quite good. However, owing to the nonisothermal nature of the process and the need for latent heat to power evaporation, the distribution of air pressure is not sufficient to determine the ROI.

Table 4.3. Dependence of Radius of Influence on Injection Pressure for Homogenous Sand Simulations

Injection Pressure (psi)	Injection Pressure (kPa)	Cut-off Pressure Pressure (kPa)	Radius of Influence (m)
15	103	10	5
25	172	17	8
50	344	34	12
100	689	69	> 25
200	1378	138	> 25
300	2068	207	> 25

Figure 4.18 shows a plot of soil moisture content as a function of distance from the injection well in a homogenous sand after 365 days of air injection. These results provide additional insight on the efficiency of the system and are perhaps a better indicator of the radius of influence than the air pressure distribution. At an injection pressure of 103 kPa (15 psi), the evaporation front extends only to a distance of about 5 m, even after 1-yr of injection. Increasing the injection pressure to 172 kPa (25 psi) pushes the evaporation front out to about 8 m whereas an injection pressure of 344 kpa (50 psi) pushes the front to about almost 12 m. All of the pressures above 344 kPa (50 psi) resulted in ROI values > 25 m, and desiccation was complete in less than 1 year. Because desiccation requires energy from the incoming air to power the evaporation process, defining the ROI will require consideration of air temperature as well as humidity as these will control to some extent the behavior of the evaporative front. Injecting heated dry air at pressures above 344 kPa (50 psi) and simultaneously operating an extraction well will lead to ROI values in excess of 25 m in sand.

It should be cautioned, however, that the ROI is an empirical value that can only be truly determined after considering site geologic conditions and material properties. This simulation was 2-D and considers only two wells. Ideally, wells should be spaced so that the overlap in their radii of influence completely covers the area of contamination, so in a 3-D simulation, well spacing would likely increase. A pilot test is recommended for evaluating effectiveness and ROI, especially where heterogeneity is known to exist.

Figure 4.17. Predicted Subsurface Air Pressure with Increasing Distance from the Injection Well Showing the Effect of Air Injection Pressure. Air at a relative humidity of 0% and heated to 30°C was injected at various pressures in a soil initially at the long-term average annual temperature of 12°C and an aqueous saturation of 20% (0.086 m^3 m^{-3}).
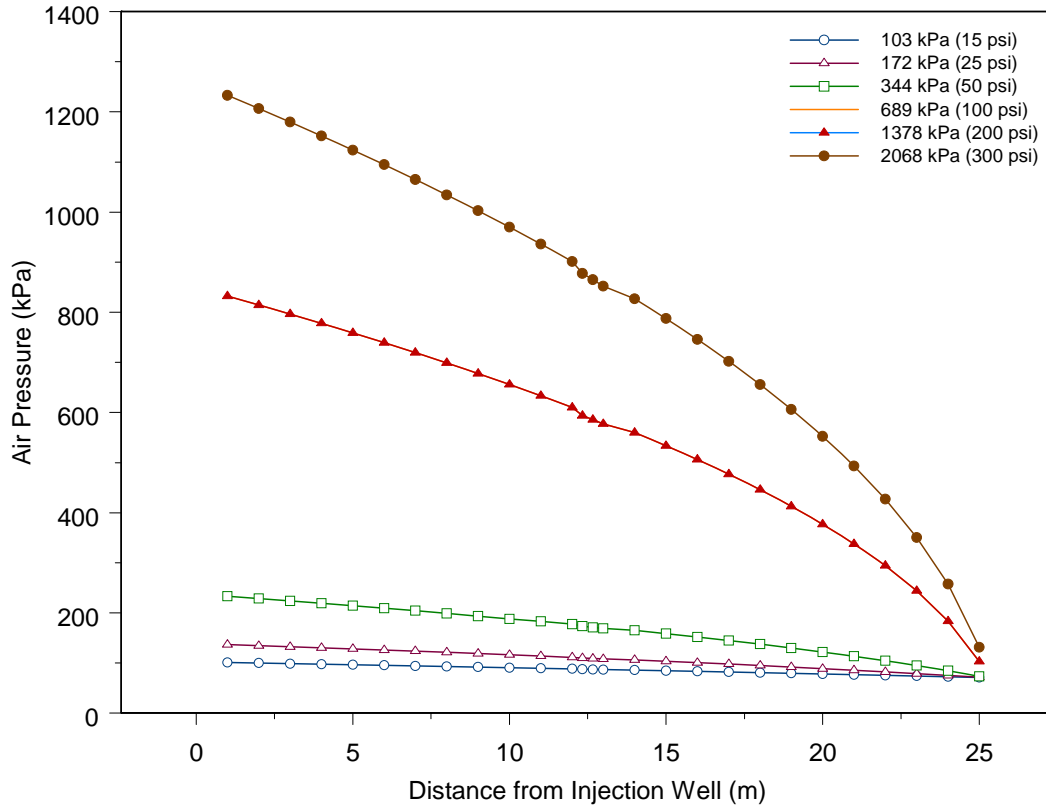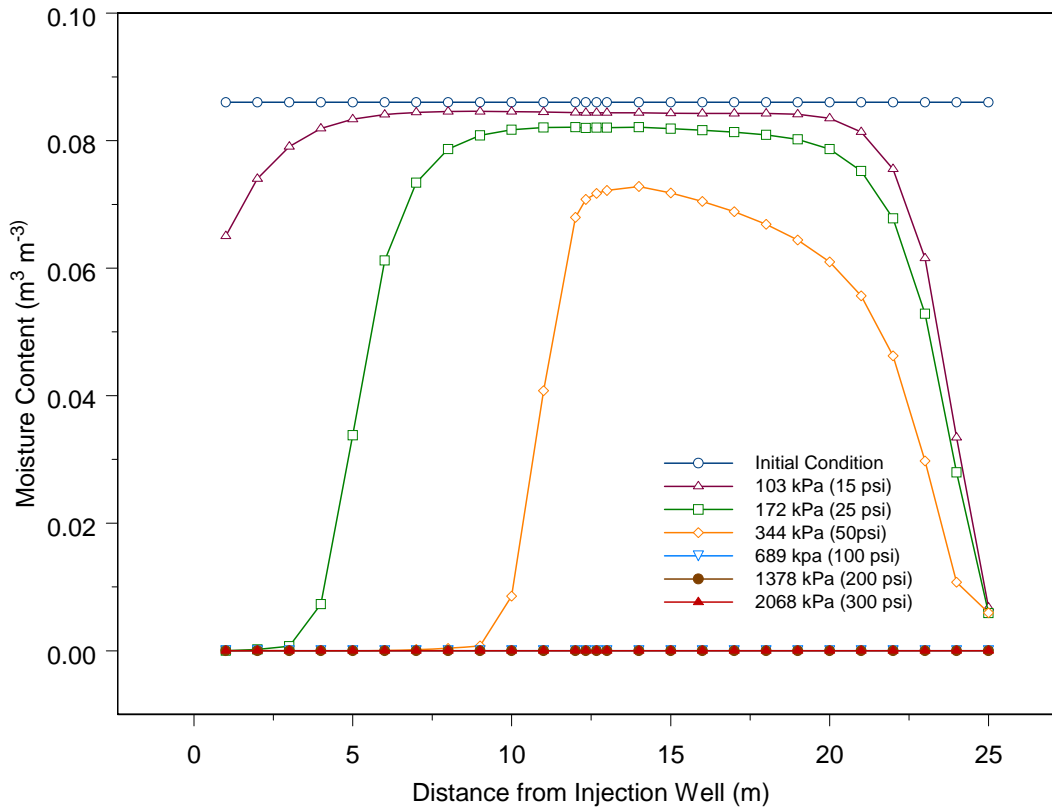
Figure 4.18. Predicted Soil Moisture Content with Increasing Distance from the Injection Well Showing the Effect of Air Injection Pressure. Air at a relative humidity of 0% and heated to 30°C was injected at various pressures in a soil initially at the long-term average annual temperature of 12°C and an aqueous saturation of 20% (0.086 $m^3 m^{-3}$).

5.0   Summary and Conclusions

Apart from source excavation, the options available for the remediation of vadose zone metal and radionuclide contaminants beyond the practical excavation depth (0 to 15 m) are quite limited. Of the available technologies, very few are applicable to the deep vadose zone. Ward et al. (2004) investigated the feasibility and efficacy of engineered barriers for the BC Cribs and trenches site, an area of concern because of elevated ^{99}Tc concentrations at a depth of 90 m below the surface. In relation to the same site, Truex reviewed six technology alternatives for minimizing downward contamination transport, of which soil desiccation ranked highest.[a] An expert panel review of the work by Ward et al. (2004) and that of Truex concluded that 1) there was a need for supplemental technologies for use with engineered barriers, and 2) there were a number of knowledge gaps that would need to be overcome before this desiccation could be deployed.[a] The report documents some of the research conducted in the last year to address some of these knowledge gaps. This work included 1) the performance of intermediate-scale laboratory flow-cell experiments to demonstrate the desiccation process, 2) the implementation of a scalable version of STOMP-WAE, and 3) the performance of numerical experiments to identify the factors controlling the performance of a desiccation system.

A total of four laboratory experiments were conducted in an intermediate-scale wedge-shaped flow cell to demonstrate the desiccation process and assess the impact of the energy balance on the desiccation process. One of the experiments was performed in homogeneous medium-grained sand, while the rest of the simulations were completed in a heterogeneous system with an inclusion of a fine-grained sand zone and varying levels of insulation. The sands were mixed with water to establish initial aqueous saturations ranging from 0.14 to 0.18. Several probes were installed to obtain temperature and relative humidity during the desiccation process with dry air. When explicitly accounting for the wall and insulation materials, the water-air-energy mode of the STOMP77 simulator was able to predict the observed experimental phenomena reasonably well in all four experiments. However, the simulator typically predicted a larger degree of cooling close to the gas-inlet boundary. In general, evaporative cooling decreased with increased distance from the inlet chamber. This result is related to the decreased air velocity and heat transport through the insulation material and the wall into the porous medium. Temperature plots for the fine-grained sands in the heterogeneous systems with PVC insulation typically showed two local minima. The first minimum is associated with the cooling due to evaporation in the adjacent medium-grained sand. The second minimum, which occurs later in time, is correlated with the evaporative cooling in the fine-grained sand itself. A comparison of the removed water mass as a function in time for the three heterogeneous experiments shows that the differences in desiccation time for the three experiments are relatively small. This observation is interesting because of the considerable differences in temperature behavior between the three experiments. This result indicates that the gas that is initially passing through cooler zones is able to increase its vapor concentration when moving through warmer moist porous media higher up in the flow cell. The results from these experiments provide an important dataset for calibration of the serial and parallel versions of the STOMP simulator.

STOMP-WAE-B has been enhanced by adding gas injection/withdrawal wells for soil-desiccation studies. Input for these well models is specified in the Source Card. STOMP-WAE-B is now available for scalable execution on multiple processor (i.e., parallel) computers. The parallel version of the

---

(a) MJ Truex. 2004. *Feasibility Study Evaluation of In Situ Technologies for Immobilization of Technetium Beneath the BC Cribs*. Letter Report, Pacific Northwest National Laboratory, Richland, Washington.

simulator is written in pure FORTRAN 90 with embedded directives that are interpreted by a FORTRAN preprocessor. Without the preprocessor, the scalable version of the simulator can be executed sequentially on a single-processor computer. The scalable version of the simulator is designated as STOMP-WAE-B-Sc. Performance tests comparing the serial and scalable versions of the code show that STOMP-WAE-B-Sc runs in 74% of the time required by STOMP-WAE-B. This difference is largely due to the PETSc solver used in STOMP-WAE-B-Sc being more efficient than the SPLIB solver used by STOMP-WAE-B. A discrepancy between the ideal scaleup and the observed can be attributed to the overhead of inter-processor communication and redundant calculations. Problems with greater than 100,000 grid cells should benefit more from execution on multiple processors on systems like EMSL's mpp2 because the computation time required on each processor will be greater than the time needed for inter-processor communication. Nonetheless, results for STOMP-WAE-B and STOMP-WAE-B-Sc run in serial and parallel are virtually identical.

Numerical studies performed with the upgraded STOMP-WAE have been used to examine the factors influencing system performance and to serve as a basis for designing remediation systems. Parametric tests suggest that the key factors controlling the desiccation process include soil texture, air-injection temperature, humidity and pressure, and the presence of a low-permeability surface seal. The effect of texture is primarily through its control of the antecedent moisture and permeability-saturation relationships. Small-scale textural changes resulting from the depositional environment will give rise to heterogeneities that can have a strong impact on the air-flow patterns and the efficacy of the desiccation process. Simulations with and without low-permeability surface seals suggest that seals essentially eliminate the short circuiting of air from the surface and eliminate zones of vertical flow around the extraction well, thereby allowing wells to be spaced farther apart. Determining the ideal spacing for a given site will require information from pilot studies that characterize field-scale air permeability and achievable air flow rates. Possible materials for use as surface seals include both synthetic (geofabrics) and natural (asphalt, bentonite) materials.

The simulations also provided insight in the importance of the injection pressure or volumetric injection rate. A 10-kPa increase in injection pressure above atmospheric pressure significantly increased the rate and efficacy of desiccation with water content declining to 0.01 m^3 m^{-3} after 1 yr of treatment. Injection at 40 kPa above atmospheric pressure removed essentially all of the water from the system after about 180 days. Heating the injected air to a temperature above the ambient soil temperature significantly increased the desiccation efficiency. Heating air to between 60 and 70°C was the most efficient in terms of desiccation rate and final moisture content, but the cost of heating was not considered. The effects of air humidity are also quite significant. Injecting humid air was very inefficient at removing moisture, even after heating, and in most cases led to the condensation of water near the injection well. Dehumidified air, even at elevated temperatures, is quite effective at drying the soils. Warm dry air (RH=0 %) completely dried the simulation domain after 126 days compared to almost 300 required when the relative humidity was 50%.

The effectiveness of desiccation is dependent on achieving and maintaining sufficient air flow to support the dominant processes. The key parameters that can be manipulated to enhance the desiccation potential include air injection temperature, humidity, and pressure. However, the entire process is governed by air permeability relationships, which in turn are governed by soil texture. Successful design and implementation of a field-scale system will require information on the heterogeneous permeability fields, including the mean and variance of the unsaturated hydraulic properties as well as the spatial correlation

structure. With the scalable implementation of STOMP, simulations of realistic desiccation targets can now be performed using parallel computing architectures at the level of discretization needed to represent the dominant processes. In the absence of highly refined field data, simulations must be based on assumed spatial correlation structure as well as the hydraulic and pneumatic property fields. Apart from the 299-E24-111 test site (Sisson and Lu site), there are essentially no data on the mean and variance of the hydraulic property field's spatial correlation structure for the Hanford Site at the scales of interest. Thus, for the design phase, pilot studies should be performed to constrain design information, including extraction well design, radius of influence, gas-flow rates, optimal applied vacuum, and water-removal rates as these are ultimately controlled by the site geology.

6.0 References

Ankeny M, and ME Burhard. 1995. "Means and method for hydraulically isolating unsaturated zones in soil." U.S. Patent #5,421,672.

Balay S, K Buschelman, V Eijkhout, WD Gropp, D Kaushik, MG Knepley, LC McInnes, BF Smith, and H Zhang. 2007. *PETSc Users Manual.* ANL-95/11 - Revision 2.3.3, Argonne National Laboratory, Argonne, Illinois.

Bramley R, and X Wang. 1996. *SPLIB: A Library of Iterative Methods for Sparse Linear Systems.* Indiana University Department of Computer Science, Bloomington, Indiana.

Brooks RH, and AT Corey. 1964. *Hydraulic Properties of Porous Media.* Hydrol. Paper 3. Colorado State University, Fort Collins, Colorado.

Cameron RJ, JC Evans, MD Johnson, and TL Liikala. 2002. *Summary of Hanford Subsurface Air Flow and Extraction (SAFE) Activities.* PNNL-13820, Pacific Northwest National Laboratory, Richland, Washington.

Cass A, GS Campbell, and TL Jones. 1984. "Enhancement of thermal water vapor diffusion in soil." *Soil Sci. Soc. Am. J.*, 48:25–32.

Chakraverty A, and SK Das. 1992. "Development of a two-directional air flow paddy dryer coupled with and integrated array of solar air heating modules." *Energy Conversion Management* 33(3):183-190.

Fayer MJ. 2000. *UNSAT-H Version 3.0: Unsaturated Soil Water and Heat Flow Model, Theory, User Manual, and Examples.* PNNL-13249, Pacific Northwest National Laboratory, Richland, Washington.

Fluor Hanford (FH). 2006. *Evaluation of Vadose Zone Treatment Technologies to Immobilize Technetium-99.* WMP-27397, Rev. 1, Fluor Hanford, Inc., Richland, Washington.

Gropp W, E Lusk, and A. Skjellum. 1999. *Using MPI: Portable Parallel Programming with the Message Passing Interface, 2nd edition.* MIT Press, Cambridge, MA.

Johnson RL, PC Johnson, DB McWhorter, RE Hinchee, and I Goodman. 1993. "An Overview of In Situ Air Sparging." *Ground Water Monitoring & Remediation* 13(4):127–135.

Johnson PC, RL Johnson, C Neaville, EE Hansen, SM Stearns, and IJ Dortch. 1997. "An assessment of conventional in situ air sparging pilot tests." *Ground Water* 35(5):765–77.

Lundegard PD, and D LaBrecque. 1998. "Geophysical and hydrologic monitoring of air sparging flow behavior: comparison of two extreme sites." *Remediation Journal*, 8(3): 59 – 71.

McKay DJ, and LJ Acomb. 1996. "Neutron moisture probe measurements of fluid displacement during in situ air sparging." *Ground Water Monitoring and Remediation* 16(4):86–94.

Oostrom M, JH Dane, and TW Wietsma. 2005. "Removal of Carbon Tetrachloride from a Layered Porous Medium by Means of Soil Vapor Extraction Enhanced by Desiccation and Water Table Reduction." *Vadose Zone Journal* 4:1170-1182.

Raimondi P, WP Acheson, and WK Overbey, Jr. 1997. "Barrier for blocking movement of contaminants within an aggregate particulate substrate." United States Patent 5591115.

Rawls WJ, LR Ahuja, and DL Brakensiek. 1992. "Estimating Soil Hydraulic Properties from Soils Data." In: *Proc. Indirect Methods for Estimating the Hydraulic Properties of Unsaturated Soils*, MT van Genuchten, FJ Leij, and LJ Lund (eds.), Riverside, California.

Rosing M. 2000. *DL Tutorial and Manual, Version 1.0*. Peak Five, Fort Collins, Colorado. Available at: http://www.peakfive.com. Accessed 12-18-2007.

Rosing M, and S Yabusaki. 1999. "A programmable preprocessor for parallelizing FORTRAN-90." In: *Proceedings of the IEEE/ACM SC99 Conference*. November 13–18, Portland, Oregon.

Schroth MH, SJ Ahearn, JS Selker, and JD Istok. 1996. "Characterization of Miller-similar silica sands for laboratory hydrologic studies." *Soil Sci. Soc. Am. J.* 60:1331-1339.

Shannon and Wilson Inc. 1994. *Geotechnical Investigation KEH W-236A Multi Function Waste Tank Facility, Hanford Site, Richland, Washington*. H-1070-50, Shannon and Wilson Inc., Kennewick, Washington.

Somerton WH, JA Keese, and SL Chu. 1974. "Thermal-Behavior of Unconsolidated Oil Sands." *Society of Petroleum Engineers Journal* 14(5):513-521.

Suthersan SS. 1996. *Remediation Engineering: Design Concepts*. Geraghty & Miller Environmental Science & Engineering Series, CRC Press, Inc., Boca Raton, Florida.

Tomlinson DW, NR Thomson, RL Johnson, and JD Redman. 2003. "Air distribution in the Borden aquifer during in situ air sparging." *Journal of Contaminant Hydrology* 67(1-4):13-132.

Thomson NR, and RL Johnson. 2000. "Air distribution during in situ air sparging: an overview of mathematical modeling." *Journal of Hazardous Materials* 72:265–282.

van Deuren J, T Lloyd, S Chetry, R Liou, and J Peck. 2002. *Remediation Technologies Screening Matrix and Reference Guide, 4th Edition*. SFIM-AEC-ET-CR-97053, U.S. Army Environmental Center, Aberdeen Proving Ground, Maryland. Available at: http://www.frtr.gov/matrix2/section1/toc.html. Accessed 12-18-07.

Walton JC, and CB Anker. 1996. "Secondary effects of soil venting and potential low cost enhancements." *Groundwater Monitoring and Remediation*, 16(3):91-97.

Ward AL. 2007. *Geotechnical, Hydrogeologic and Vegetation Data Package for 200-UW-1 Waste Site Engineered Surface Barrier Design*. PNNL-17134, Pacific Northwest National Laboratory, Richland, Washington.

Ward AL, GW Gee, JS Selker, and C Cooper. 2001. *Rapid Migration of Radionuclides Leaked from High-Level Water Tanks: A Study of Salinity Gradients, Wetted Path Geometry, and Water Vapor Transport*. Project 65410, Final Report, Environmental Management Science Program, U.S. Department of Energy..

Ward AL, GW Gee, ZF Zhang, and JM Keller. 2004. *Vadose Zone Contaminant Fate and Transport Analysis for the 216-B-26 Trench.* PNNL-14907, Pacific Northwest National Laboratory, Richland, Washington.

Ward AL, MD White, EJ Freeman, and ZF Zhang. 2005. *STOMP Subsurface Transport Over Multiple Phases Version 1.0 Addendum: Sparse Vegetation Evapotranspiration Model for the Water-Air-Energy Operational Mode*. PNNL-15465, Pacific Northwest National Laboratory, Richland, Washington.

White M D, and BP McGrail. 2005. *STOMP Subsurface Transport Over Multiple Phases, Version 1.0, Addendum: ECKEChem Equilibrium-Conservation-Kinetic Equation Chemistry and Reactive Transport.* PNNL-15482, Pacific Northwest National Laboratory, Richland, Washington.

White MD, and M Oostrom. 2006. *STOMP Subsurface Transport Over Multiple Phases, Version 4.0, User's Guide*. PNNL-15782, Pacific Northwest National Laboratory, Richland, Washington.

Appendix A

Example Input File for Simulation of Laboratory Experiments

Appendix A: Example Input File for Simulation of Laboratory Experiments

```
#----------------------------------------------------
~Simulation Title Card
#----------------------------------------------------
1,
Wedge,
Mart Oostrom,
PNNL,
October 2007,
15:15,
4,
EMSL Desiccation Wedge,
Heterogeneous Packing,
Experiment HET2,
Thickness insulation is 2.54 cm,
#----------------------------------------------------
~Solution Control Card
#----------------------------------------------------
Normal,
Water-Air-Energy,Courant,
1,
0,day,500,hr,1,s,1,hr,1.25,16,1.e-06,
100000,
Variable Aqueous Diffusion,
Variable Gas Diffusion,
0,
#----------------------------------------------------
~Grid Card
#----------------------------------------------------
Cartesian,
81,40,9,
14,cm,1@0.5,cm,80@1,cm,1@0.5,cm,
0,cm,40@0.5,cm,
0,cm,3@1.25,cm,3@0.125,cm,3@1.04666,cm,
#----------------------------------------------------
~Rock/Soil Zonation Card
#----------------------------------------------------
# Sand 1 is 40/50 sand
# Sand 2 is 70 sand
4,
PVC,1,81,1,40,1,3,
Glass,1,81,1,40,4,6,
Sand1,1,81,1,40,7,9,
```

Sand2,21,70,33,40,7,9,

#--
~Inactive Node Card
#--
Inactive nodes to allow for stairstepping
27,
1,3,1,35,1,9,
4,6,1,34,1,9,
7,9,1,33,1,9,
10,12,1,32,1,9,
13,15,1,31,1,9,
16,18,1,30,1,9,
19,21,1,29,1,9,
22,24,1,28,1,9,
25,27,1,27,1,9,
28,30,1,26,1,9,
31,33,1,25,1,9,
34,36,1,24,1,9,
37,39,1,23,1,9,
40,42,1,22,1,9,
43,45,1,21,1,9,
46,48,1,20,1,9,
49,51,1,19,1,9,
52,54,1,18,1,9,
55,57,1,17,1,9,
58,60,1,16,1,9,
61,63,1,15,1,9,
64,66,1,14,1,9,
67,69,1,13,1,9,
70,72,1,12,1,9,
73,75,1,11,1,9,
76,78,1,10,1,9,
79,81,1,9,1,9,
#--
~Mechanical Properties Card
#--
Sand porosities from experimental data
PVC,1400,kg/m^3,0.97,0.97,,,,,,
Glass,2650,kg/m^3,0.00001,0.00001,,,,,,
Sand1,2650,kg/m^3,0.32,0.32,,,,,,
Sand2,2650,kg/m^3,0.40,0.40,,,,,,
#--
~Hydraulic Properties Card
#--
40/50 Sand data from Schroth et al., SSSJA, 1996
70 Sand data from Hydraulic Prop. Apparatus in EMSL
PVC,0.00001,hc:cm/min,0.00001,hc:cm/min,0.00001,hc:cm/min,

A.2

Glass,0.00001,hc:cm/min,0.00001,hc:cm/min,0.00001,hc:cm/min,
Sand1,4.33,hc:cm/min,4.33,hc:cm/min,4.33,hc:cm/min,
Sand2,0.9,hc:cm/min,0.9,hc:cm/min,0.9,hc:cm/min,
#--
~Thermal Properties Card
#--
Sand data obtained with Decagon apparatus in EMSL lab
Glass and PVC data from supplier
PVC,Somerton,0.036,W/m K,0.036,W/m K,0.036,W/m K,0.036,W/m K,0.036,W/m K,0.036,W/m K,914,J/kg K,
Glass,Somerton,0.61,W/m K,0.61,W/m K,0.61,W/m K,0.61,W/m K,0.61,W/m K,0.61,W/m K,816,J/kg K,
Sand1,Somerton,0.21,W/m K,0.21,W/m K,0.21,W/m K,2.52,W/m K,2.52,W/m K,2.52,W/m K,773,J/kg K,
Sand2,Somerton,0.19,W/m K,0.19,W/m K,0.19,W/m K,2.16,W/m K,2.16,W/m K,2.16,W/m K,781,J/kg K,
#--
~Saturation Function Card
#--
PVC,Brooks and Corey,100,m,5.0,0.0,,
Glass,Brooks and Corey,100,m,5.0,0.0,,
Sand1,Brooks and Corey,19.4,cm,6.1,0.0,,
Sand2,Brooks and Corey,41.0,cm,5.8,0.0,,
#--
~Aqueous Relative Permeability Card
#--
PVC,constant,0,
Glass,constant,0,
Sand1,constant,0,
Sand2,constant,0,
#--
~Gas Relative Permeability Card
#--
PVC,constant,0,
Glass,constant,0,
Sand1,Mualem,,
Sand2,Mualem,,
#--
~Initial Conditions Card
#--
Aqueous Saturation,Gas Pressure,
8,
Aqueous Saturation,0.142,,,,,,,,1,20,1,40,8,9,
Aqueous Saturation,0.142,,,,,,,,21,70,1,35,7,9,
Aqueous Saturation,0.142,,,,,,,,71,81,1,40,7,9,
Aqueous Saturation,0.181,,,,,,,,21,70,33,40,7,9,
Aqueous Saturation,0.00001,,,,,,,,1,81,1,40,4,6,
Aqueous Saturation,0.00001,,,,,,,,1,81,1,40,1,3,
Gas Pressure,101325,Pa,,,,,,1,81,1,40,1,9,
Temperature,22.0,C,,,,,,1,81,1,40,1,9,
#--
~Boundary Conditions Card

A.3

```
#----------------------------------------------------
29,
West,Dirichlet Energy,Zero Flux Aqueous,Neumann Gas,
1,1,36,40,3,5,1,
0,day,22,C,,,1.0,63.7695,cm/min,0.0,
East,Outflow,Zero Flux Aqueous,Dirichlet Gas,
81,81,1,40,3,5,1,
0,day,,,,,1.0,101325,Pa,1.0,
Bottom,Dirichlet,Zero Flux Aqueous,Zero Flux Gas,
1,3,36,40,1,1,1,
0,day,22,C,,,,,,
Bottom,Dirichlet,Zero Flux Aqueous,Zero Flux Gas,
4,6,35,40,1,1,1,
0,day,22,C,,,,,,
Bottom,Dirichlet,Zero Flux Aqueous,Zero Flux Gas,
7,9,34,40,1,1,1,
0,day,22,C,,,,,,
Bottom,Dirichlet,Zero Flux Aqueous,Zero Flux Gas,
10,12,33,40,1,1,1,
0,day,22,C,,,,,,
Bottom,Dirichlet,Zero Flux Aqueous,Zero Flux Gas,
13,15,32,40,1,1,1,
0,day,22,C,,,,,,
Bottom,Dirichlet,Zero Flux Aqueous,Zero Flux Gas,
16,18,31,40,1,1,1,
0,day,22,C,,,,,,
Bottom,Dirichlet,Zero Flux Aqueous,Zero Flux Gas,
19,21,30,40,1,1,1,
0,day,22,C,,,,,,
Bottom,Dirichlet,Zero Flux Aqueous,Zero Flux Gas,
22,24,29,40,1,1,1,
0,day,22,C,,,,,,
Bottom,Dirichlet,Zero Flux Aqueous,Zero Flux Gas,
25,27,28,40,1,1,1,
0,day,22,C,,,,,,
Bottom,Dirichlet,Zero Flux Aqueous,Zero Flux Gas,
28,30,27,40,1,1,1,
0,day,22,C,,,,,,
Bottom,Dirichlet,Zero Flux Aqueous,Zero Flux Gas,
31,33,26,40,1,1,1,
0,day,22,C,,,,,,
Bottom,Dirichlet,Zero Flux Aqueous,Zero Flux Gas,
34,36,25,40,1,1,1,
0,day,22,C,,,,,,
Bottom,Dirichlet,Zero Flux Aqueous,Zero Flux Gas,
37,39,24,40,1,1,1,
0,day,22,C,,,,,,
Bottom,Dirichlet,Zero Flux Aqueous,Zero Flux Gas,
```

```
40,42,23,40,1,1,1,
0,day,22,C,,,,,,
Bottom,Dirichlet,Zero Flux Aqueous,Zero Flux Gas,
43,45,22,40,1,1,1,
0,day,22,C,,,,,,
Bottom,Dirichlet,Zero Flux Aqueous,Zero Flux Gas,
46,48,21,40,1,1,1,
0,day,22,C,,,,,,
Bottom,Dirichlet,Zero Flux Aqueous,Zero Flux Gas,
49,51,20,40,1,1,1,
0,day,22,C,,,,,,
Bottom,Dirichlet,Zero Flux Aqueous,Zero Flux Gas,
52,54,19,40,1,1,1,
0,day,22,C,,,,,,
Bottom,Dirichlet,Zero Flux Aqueous,Zero Flux Gas,
55,57,18,40,1,1,1,
0,day,22,C,,,,,,
Bottom,Dirichlet,Zero Flux Aqueous,Zero Flux Gas,
58,60,17,40,1,1,1,
0,day,22,C,,,,,,
Bottom,Dirichlet,Zero Flux Aqueous,Zero Flux Gas,
61,63,16,40,1,1,1,
0,day,22,C,,,,,,
Bottom,Dirichlet,Zero Flux Aqueous,Zero Flux Gas,
64,66,15,40,1,1,1,
0,day,22,C,,,,,,
Bottom,Dirichlet,Zero Flux Aqueous,Zero Flux Gas,
67,69,14,40,1,1,1,
0,day,22,C,,,,,,
Bottom,Dirichlet,Zero Flux Aqueous,Zero Flux Gas,
70,72,13,40,1,1,1,
0,day,22,C,,,,,,
Bottom,Dirichlet,Zero Flux Aqueous,Zero Flux Gas,
73,75,12,40,1,1,1,
0,day,22,C,,,,,,
Bottom,Dirichlet,Zero Flux Aqueous,Zero Flux Gas,
76,78,11,40,1,1,1,
0,day,22,C,,,,,,
Bottom,Dirichlet,Zero Flux Aqueous,Zero Flux Gas,
79,81,10,40,1,1,1,
0,day,22,C,,,,,,
#-----------------------------------------------------
~Output Options Card
#-----------------------------------------------------
13,
6,40,5,  # 5 cm
16,40,5, # 15 cm
26,40,5, # 25 cm
```

26,30,5, # 25 cm
36,40,5, # 35 cm
36,29,5, # 35 cm
46,40,5, # 45 cm
46,27,5, # 45 cm
56,40,5, # 55 cm
56,25,5, # 55 cm
66,40,5, # 65 cm
66,24,5, # 65 cm
76,40,5, # 75 cm
1,1,hr,m,6,6,6,
6,
Temperature,,
Aqueous saturation,,
humidity,,
Water gas concentration,g/m^3,
Water vapor partial pressure,Pa,
xnc gas volumetric flux,cm/min,
1,
5,d,
9,
no restart,,
Temperature,,
Aqueous saturation,,
humidity,,
Water gas concentration,g/L,
Water gas mass frac.,,
xnc gas volumetric flux,cm/min,
Aqueous pressure,,
Gas pressure,,
#--
~Surface Card
#--
9,
Gas advective water mass,kg/min,kg,east,81,81,1,40,3,5,
Gas diffusive water mass,kg/min,kg,east,81,81,1,40,3,5,
Gas Volumetric Flux,L/min,L,West,1,1,36,40,3,5,
Gas Volumetric Flux,L/min,L,East,81,81,1,40,3,5,
Gas Mass Flux,kg/min,kg,West,1,1,36,40,3,5,
Gas Mass Flux,kg/min,kg,East,81,81,1,40,3,5,
Heat,W,J,West,1,1,36,40,3,5,
Heat,W,J,East,81,81,1,40,3,5,
Heat,W,J,Bottom,1,81,1,40,3,5,

Appendix B

Example Input file for Controlling Factors

Appendix B: Example Input File for Controlling Factors

```
#----------------------------------------------------
~Simulation Title Card
#----------------------------------------------------
1,
Z-direction Horizontal Withdrawal Well,
Andy Ward,
PNNL,
Mar 9 2007,
17:23,
3,
Z-direction vertical injection and extraction wells.
Injection at 10 degrees C,
Sand Homogeneous,
#----------------------------------------------------
~Solution Control Card
#----------------------------------------------------
Normal,
Water-Air-Energy,
1,
0,day,365,day,1,s,100,day,1.25,16,1.e-06,
1000,
Variable Aqueous Diffusion,
Variable Gas Diffusion,
0,
#----------------------------------------------------
~Grid Card
#----------------------------------------------------
Cartesian,
27,1,25,
0,m,12@1.0,m,3@0.33333,m,12@1.0,m,
0,m,1@1.0,m,
0,m,1@0.50,m,23@1.0,m,1@0.50,m,
#----------------------------------------------------
~Rock/Soil Zonation Card
#----------------------------------------------------
2,
Sand,1,27,1,1,1,25,
Clay,1,27,1,1,24,25,
#----------------------------------------------------
~Mechanical Properties Card
#----------------------------------------------------
Sand,2650,kg/m^3,0.437,0.430,0,,Millington and Quirk,
```

Clay,2650,kg/m^3,0.475,0.475,0,,Millington and Quirk,

#---
~Hydraulic Properties Card
#---
Sand,21.0,hc:cm/hr,,,21.0,hc:cm/hr,
Clay,0.06,hc:cm/hr,,,0.06,hc:cm/hr,

#---
~Thermal Properties Card
#---
Sand,Cass,0.60,W/m K,0.70,W/m K,8.0,0.26,W/m K,3.0,750.0,J/kg K,
Clay,Cass,0.60,W/m K,0.70,W/m K,8.0,0.26,W/m K,3.0,750.0,J/kg K,

#---
~Saturation Function Card
#---
Sand,Extended Brooks and Corey,15.98,cm,0.69,0.046,,,
Clay,Extended Brooks and Corey,85.6,cm,0.17,0.189,,,

#---
~Aqueous Relative Permeability Card
#---
Sand, Mualem,,,
Clay, Mualem,,,

#---
~Gas Relative Permeability Card
#---
Sand, Mualem,,
Clay, Mualem,,

#---
~Initial Conditions Card
#---
Aqueous Saturation, Gas Pressure,
3,
Aqueous Saturation,0.20,,,,,,,1,27,1,1,1,25,
Gas Pressure,101325,Pa,,,,,,1,27,1,1,1,25,
Temperature,25.0,C,,,,,,1,27,1,1,1,25,

#---
~Boundary Conditions Card
#---
2,
Top,Dirichlet Energy,Zero Flux Aqueous,Zero Flux Gas,
1,27,1,1,25,25,1,
0,day,25,C,,,1.0,,,1.0,
Bottom,Dirichlet Energy,Zero Flux,Zero Flux,
1,27,1,1,1,1,1,
0,day,25,C,,,1.0,,,1.0,

#---
~Source Card
#---
2,

Z-Direction Injection Well
Z-Direction Injection Well,Water Relative Humidity,1,1,1,1,11,16,1,
0,s,141325,Pa,15.24,cm,0.5,0.5,1e-17,m^2,30,C,
#
Z-Direction Injection Well,Water Relative Humidity,27,27,1,1,11,16,1,
0,s,61325,Pa,15.24,cm,0.5,0.5,1e-17,m^2,30,C,
#--
~Output Options Card
#--
27,
1,1,12,
2,1,12,
3,1,12,
4,1,12,
5,1,12,
6,1,12,
7,1,12,
8,1,12,
9,1,12,
10,1,12,
11,1,10,
12,1,12,
13,1,12,
14,1,12,
15,1,12,
16,1,12,
17,1,12,
18,1,12,
19,1,12,
20,1,12,
21,1,12,
22,1,12,
23,1,12,
24,1,12,
25,1,12,
26,1,12,
27,1,12,
1,1,day,m,5,5,5,
8,
Temperature,c,
Aqueous moisture content,,
Aqueous saturation,,
Gas Saturation,,
Aqueous matric potential,cm,
Gas pressure,Pa,
Water Gas Conc.,g/m^3,
Water Gas Mass Frac.,,
366,

B.3

0,day,
1,day,
2,day,
3,day,
4,day,
5,day,
6,day,
7,day,
8,day,
9,day,
10,day,
11,day,
12,day,
13,day,
14,day,
15,day,
16,day,
17,day,
18,day,
19,day,
20,day,
21,day,
22,day,
23,day,
24,day,
25,day,
26,day,
27,day,
28,day,
29,day,
30,day,
31,day,
32,day,
33,day,
34,day,
35,day,
36,day,
37,day,
38,day,
39,day,
40,day,
41,day,
42,day,
43,day,
44,day,
45,day,
46,day,
47,day,

48,day,
49,day,
50,day,
51,day,
52,day,
53,day,
54,day,
55,day,
56,day,
57,day,
58,day,
59,day,
60,day,
61,day,
62,day,
63,day,
64,day,
65,day,
66,day,
67,day,
68,day,
69,day,
70,day,
71,day,
72,day,
73,day,
74,day,
75,day,
76,day,
77,day,
78,day,
79,day,
80,day,
81,day,
82,day,
83,day,
84,day,
85,day,
86,day,
87,day,
88,day,
89,day,
90,day,
91,day,
92,day,
93,day,
94,day,
95,day,

96,day,
97,day,
98,day,
99,day,
100,day,
101,day,
102,day,
103,day,
104,day,
105,day,
106,day,
107,day,
108,day,
109,day,
110,day,
111,day,
112,day,
113,day,
114,day,
115,day,
116,day,
117,day,
118,day,
119,day,
120,day,
121,day,
122,day,
123,day,
124,day,
125,day,
126,day,
127,day,
128,day,
129,day,
130,day,
131,day,
132,day,
133,day,
134,day,
135,day,
136,day,
137,day,
138,day,
139,day,
140,day,
141,day,
142,day,
143,day,

B.6

144,day,
145,day,
146,day,
147,day,
148,day,
149,day,
150,day,
151,day,
152,day,
153,day,
154,day,
155,day,
156,day,
157,day,
158,day,
159,day,
160,day,
161,day,
162,day,
163,day,
164,day,
165,day,
166,day,
167,day,
168,day,
169,day,
170,day,
171,day,
172,day,
173,day,
174,day,
175,day,
176,day,
177,day,
178,day,
179,day,
180,day,
181,day,
182,day,
183,day,
184,day,
185,day,
186,day,
187,day,
188,day,
189,day,
190,day,
191,day,

192,day,
193,day,
194,day,
195,day,
196,day,
197,day,
198,day,
199,day,
200,day,
201,day,
202,day,
203,day,
204,day,
205,day,
206,day,
207,day,
208,day,
209,day,
210,day,
211,day,
212,day,
213,day,
214,day,
215,day,
216,day,
217,day,
218,day,
219,day,
220,day,
221,day,
222,day,
223,day,
224,day,
225,day,
226,day,
227,day,
228,day,
229,day,
230,day,
231,day,
232,day,
233,day,
234,day,
235,day,
236,day,
237,day,
238,day,
239,day,

240,day,
241,day,
242,day,
243,day,
244,day,
245,day,
246,day,
247,day,
248,day,
249,day,
250,day,
251,day,
252,day,
253,day,
254,day,
255,day,
256,day,
257,day,
258,day,
259,day,
260,day,
261,day,
262,day,
263,day,
264,day,
265,day,
266,day,
267,day,
268,day,
269,day,
270,day,
271,day,
272,day,
273,day,
274,day,
275,day,
276,day,
277,day,
278,day,
279,day,
280,day,
281,day,
282,day,
283,day,
284,day,
285,day,
286,day,
287,day,

288,day,
289,day,
290,day,
291,day,
292,day,
293,day,
294,day,
295,day,
296,day,
297,day,
298,day,
299,day,
300,day,
301,day,
302,day,
303,day,
304,day,
305,day,
306,day,
307,day,
308,day,
309,day,
310,day,
311,day,
312,day,
313,day,
314,day,
315,day,
316,day,
317,day,
318,day,
319,day,
320,day,
321,day,
322,day,
323,day,
324,day,
325,day,
326,day,
327,day,
328,day,
329,day,
330,day,
331,day,
332,day,
333,day,
334,day,
335,day,

336,day,
337,day,
338,day,
339,day,
340,day,
341,day,
342,day,
343,day,
344,day,
345,day,
346,day,
347,day,
348,day,
349,day,
350,day,
351,day,
352,day,
353,day,
354,day,
355,day,
356,day,
357,day,
358,day,
359,day,
360,day,
361,day,
362,day,
363,day,
364,day,
365,day,
16,
Rock/Soil Type,,
Temperature,C,
Aqueous moisture content,,
Aqueous saturation,,
Gas Saturation,,
Aqueous matric potential,cm,
Gas pressure,Pa,
Aqueous relative permeability,,
Gas relative permeability,,
Water Gas Conc.,g/m^3,
Water gas mass frac.,,
xnc aqueous vol,cm/hr,
znc aqueous vol,cm/hr,
xnc gas vol,cm/hr,
znc gas vol,cm/hr,
no restart,,
#--

B.11

~Surface Flux Card
#---
12,
Aqueous Volumetric,cm^3/day,cm^3,West,2,2,1,1,2,24, # Injection Well
Aqueous Volumetric,cm^3/day,cm^3,East,26,26,1,1,2,24,# Withdrawal Well
Gas Volumetric,cm^3/day,cm^3,West,2,2,1,1,2,24, # Injection Well
Gas Volumetric,cm^3/day,cm^3,East,26,26,1,1,2,24,# Withdrawal Well
Condensate Water Mass,kg/day,kg,West,2,2,1,1,2,24, # Injection Well
Condensate Water Mass,kg/day,kg,East,26,26,1,1,2,24, # Withdrawal Well
Gas Advective Water Mass,kg/day,kg,West,2,2,1,1,2,24, # Injection Well
Gas Advective Water Mass,kg/day,kg,East,26,26,1,1,2,24, # Withdrawal Well
Gas Diffusive Water Mass,kg/day,kg,West,2,2,1,1,2,24, # Injection Well
Gas Diffusive Water Mass,kg/day,kg,East,26,26,1,1,2,24, # Withdrawal Well
Gas Advective Heat Flux,W,J,West,2,2,1,1,2,24, # Injection Well
Gas Diffusive Heat Flux,W,J,East,26,26,1,1,2,24, # Withdrawal Well

Distribution

No. of Copies				No. of Copies		

ONSITE

3 U.S. Department of Energy-Richland Operations
    Bryan Foley   A6-38
    Kevin Leary   A6-38
    DOE Public Reading Room   H2-53

2 Lockheed Martin Information Technology
    Central Files   B1-07
    Document Processing Center   A3-94

2 CH2M Hill Hanford, Inc.
    William McMahon   E6-35
    Curtis Wittreich   H6-62

ONSITE

6 Fluor Hanford, Inc.
    Chris Sutton   E6-35
    Larry Fitch   E6-35
    Scott Petersen   E6-35
    Bruce Ford   E6-35
    Dave Fort   E6-35
    Mark Benecke   E6-35

12 Pacific Northwest National Laboratory
    Diana Bacon   K9-33
    Mart Oostrom   K9-33
    Mark Freshley   K9-33
    Charlie Kincaid   K9-33
    Andy Ward (5)   K9-33
    Mike Truex   K6-96
    Hanford Technical Library (2)   P8-55